

©2018

Nathan D. Rudd

ALL RIGHTS RESERVED

DUAL-LIGAND LUMINESCENT METAL-ORGANIC FRAMEWORKS TOWARDS
ENVIRONMENTAL REMEDIATION EFFORTS

By

Nathan D. Rudd

A dissertation submitted to the

School of Graduate Studies

Rutgers, The State University of New Jersey

In partial fulfillment of the requirements

For the degree of

Doctor of Philosophy

Graduate Program in Chemistry and Chemical Biology

Written under the direction of

Jing Li

And approved by

New Brunswick, New Jersey

October 2018

ABSTRACT OF THE DISSERTATION

Dual-Ligand Metal-Organic Frameworks towards Environmental Remediation Efforts

By Nathan D. Rudd

Dissertation Director:
Dr. Jing Li

Rapid industrialization during the 20th century has left an indelible mark on the global landscape. Often, industrial processes cannot be regulated to match the pace at which nations are developing—infrastructures become more complex without proper management. Contamination of local environments from these operations has plagued ecosystems and can lead to detrimental effects on a larger scale. In recent decades, the development of “green” industrial agendas has diminished pollution and enriched efforts for environmentally sustainable technologies, however this progression does not remediate the contamination that already exists. Functional materials that can detect ultralow concentrations of pollutants are essential before they accumulate and cause extensive damage. Furthermore, dual-performance compounds that sense and extract contaminants would streamline environmental purification efforts and simplify remediation procedures.

Luminescent metal-organic frameworks (LMOFs) are a rapidly growing category of functional, crystalline materials useful for a broad range of applications. LMOFs are comprised of single metal ions or clusters linked together through organic ligands. Extended, multidimensional frameworks are formed that boast tunable surfaces and optical properties. The ability to alter porosity and chemical functionalities within the material enhance the effectiveness to interact with specifically targeted analytes.

Organic ligands within LMOFs, through the scope of this work, contain aromatic groups that undergo optical emission under specific irradiation. Linker molecules with varying functional

moieties are also incorporated into LMOFs. When assembled together, the materials that are produced exhibit altered optical emission profiles through strong guest-host interactions as well as the interplay between the optically-active and functionalized organic ligands. Additionally, enhanced uptake of guest molecules into the LMOF channels highlight the dual-performance of these materials.

Overall, this dissertation focuses on the design, synthesis, characterization and application of LMOFs for the luminescence-based sensing and extraction of various inorganic/organic species, important for both contamination remediation and energy-related applications.

ACKNOWLEDGEMENTS

To begin, I would like to thank my research advisor, Dr. Jing Li, for her continued support and encouragement during my tenure as a graduate student at Rutgers University. She has exhibited a perseverance towards scientific advancement that has been a constant inspiration. Her advice has not only enriched my knowledge in our field, but also taught me how to harness the power of the scientific community to expand my projects. Her work ethic is something I will strive to mimic throughout the rest of my career. Additionally, I am very grateful to have worked alongside members of my dissertation committee—Dr. Eric Garfunkel, Dr. KiBum Lee, and Dr. Long Pan—who have provided advice and insight that helped to push me through my research.

I would also like to thank past and present members of the Li research group. Any progress in my dissertation can also be attributed to their contributions, both as friends and fellow scientists, with special gratitude towards Dr. Ben Deibert and William Lustig. Also, I am very appreciative for the efforts from scientists across the country who have directly contributed to my dissertation research, including Dr. Gene Hall, Dr. Feng Chen, Dr. Simon Teat, Dr. Yves Chabal, Dr. Erika Fuentes-Fernandez, and Dr. Kui Tan.

Lastly, I would like to thank members of my family. It is their efforts throughout my life that have brought me to where I am today. Thank you to my fiancée, Kristen DeGraff, who has listened to every presentation, read every manuscript, and was always there for me throughout this process. I will always appreciate, and reciprocate, her love and support. My sister, Merrill, represents what it means to be a dedicated scientist and has always set goals for me, whether she knew it or not. We are each other's biggest fan, and I wouldn't have it any other way. Last, but not least, I would like to recognize my parents. They have always let me follow my passion and their

unconditional love and support has helped me through every decision. My parents have enabled me to not only be where I am today, but also who I am—for this, I will be forever grateful.

TABLE OF CONTENTS

Abstract of the Dissertation	ii
Acknowledgement	iv
Table of Contents	vi
List of Tables	ix
List of Figures	xi
Chapter 1: Introduction	1
1.1 LMOF Background	1
1.2 LMOFs as Sensors	2
1.3 Advantages of Dual-Ligand LMOFs	3
Chapter 2: Simultaneous Detection and Extraction of Heavy Metals from Water	5
2.1 Introduction	5
2.2 Experimental Details	7
2.2.1 Ligand Syntheses	7
2.2.2 Isorecticular MOF Synthesis	9
2.2.3 Structural Analysis of LMOF-261	9
2.2.4 Additional Instrumental Details	12
2.2.5 Fluorescence Titrations	16
2.3 Results and Discussion	16
2.3.1 Crystal Structure Analysis	16
2.3.2 Pore Characterization	18
2.3.3 Optical Properties of LMOF-261, -262, and -263	20

2.3.4 Heavy Metal Detection	22
2.3.5 Heavy Metal Removal	28
2.3.6 Hg ²⁺ Interaction Mechanism	34
2.4 Conclusions.....	42
Chapter 3: Ligand-based Emission towards the Detection of Carbon Tetrachloride	43
3.1 Introduction.....	43
3.2 Experimental Details.....	45
3.2.1 Synthesis of LMOF-271	45
3.2.2 Structural Characterization	46
3.2.3 Porosity Investigation	48
3.2.4 Thermogravimetric Analysis	49
3.2.5 Optical Characterization	49
3.2.6 Fluorescence Titrations	51
3.3 Results and Discussion	51
3.3.1 Crystal Structure Analysis	51
3.3.2 Optical Detection	53
3.4 Conclusions.....	59
Chapter 4: LMOFs for Lithium Harvesting Applications.....	59
4.1 Introduction.....	59
4.2 Experimental Details.....	62
4.2.1 Ligand Synthesis	62
4.2.2 Synthesis of Zr ₆ O ₄ (OH) ₄ (btb) ₂ (dsab) ₃ (LMOF-321)	63
4.2.3 Structural Analysis of LMOF-321	64

4.2.4 Pore Characterization.....	65
4.2.5 Additional Instrumental Details.....	66
4.2.6 Fluorescence Titrations.....	69
4.3 Results and Discussion	69
4.3.1 Synthesis of an Isorecticular Zr-MOF	69
4.3.2 Lithium-Ligand Interaction.....	70
4.3.3 Optical Properties.....	71
4.3.4 Lithium Detection	71
4.3.5 Lithium Extraction.....	76
4.3.6 Interaction Mechanism.....	80
4.4 Conclusions.....	82
Chapter 5: Conclusions and Outlook	83
List of Abbreviations	85
References.....	86

LIST OF TABLES

Table 2.1. Single crystal data of LMOF-261	10
Table 2.2. IQY data for as-made and outgassed samples of LMOF-261, -262 and -263 under 360 nm excitation.....	14
Table 2.3. XRF data from a 50:50 (w/w) mixture of $\text{HgCl}_2\text{:ZnO}$ and as-made LMOF-263	15
Table 2.4. Relative molar ratios of $\text{Hg}^{2+}\text{:Zn}^{2+}$ in LMOF-263 after exposure to various Hg^{2+} concentrations. Values represent averages over three trials	33
Table 2.5. Summary of XPS data for LMOF-263 exposed to various Hg^{2+} and Mg^{2+} concentrations	40
Table 2.6. The percent atomic concentration at each oxygen core level over multiple Hg^{2+} and Mg^{2+} exposure conditions	41
Table 3.1. Single crystal data of LMOF-271	47
Table 4.1. IQY data for as-made and outgassed samples of LMOF-321, H_3btb , and PCN-133 ..	68

LIST OF SCHEMES

Scheme 2.1. tppe synthesis	7
Scheme 2.2. H ₂ hfdc synthesis	8
Scheme 2.3. H ₂ dbtdcO ₂ synthesis	8

LIST OF FIGURES

Figure 2.1. PXRD patterns of the LMOF isorecticular series (LMOF-261, -262, and -263).....	11
Figure 2.2. Crystal images of (a) LMOF-261 and (b) LMOF-262	11
Figure 2.3. LMOF-263 is stable under a variety of conditions, including a) in water for 24 h and b) 2 weeks. Also, LMOF-263 stayed relatively stable exposed to pH c) 4, d) 6, e) 8 and f) 10 for 15 h, with the low angle peaks showing increased crystallinity under basic conditions	12
Figure 2.4. Thermogravimetric (TG) analysis of as-made LMOF-261 (green), -262 (purple) and -263 (red).....	13
Figure 2.5. (a) The PBU of LMOF-261, depicting a pseudo-tetrahedrally coordinated Zn center bound to two fluorophoric tppe ligands and two ofdc linkers. (b) An individual net of the LMOF-261 framework viewed along the b-axis, containing 1D, edge sharing pentagonal and rhombohedral channels. (c) The same net depicted down the c-axis, showcasing edge sharing octahedral and cylindrical channels. The ofdc linkers point directly into the cylindrical channels extending down the c-axis. (d) Simplified LMOF-261 depicting four-fold interpenetration. Each of the three other nets occupies one octahedral pore of the fourth net to create narrow pentagonal channels, sharing edges from multiple nets	18
Figure 2.6. N ₂ adsorption and desorption isotherms for a) LMOF-261 and b) LMOF-263. c) The H-K micropore size distribution analysis of LMOF-261, indicating micropores in the range of 5-10 Å.....	19
Figure 2.7. CO ₂ adsorption and desorption isotherms for LMOF-261 and -263. Uptake maxima increased from LMOF-261 to -263, with 1.60 and 2.22 mmol/g, respectively	20

Figure 2.8. Optical absorption spectra (converted to KM Function) of as-made LMOF-261 (green), -262 (purple), -263 (red) and 4-ttpe (blue)	21
Figure 2.9. Optical emission (solid) and excitation (dotted) spectra of as-made LMOF-261, -262 and -263	21
Figure 2.10. Optical emission and excitation spectra for outgassed LMOF-261 (green), -262 (purple) and -263 (red). Values in parentheses provide the emission or excitation wavelength at which the displayed excitation or emission spectra, respectively, were monitored. The emission maxima of outgassed samples of LMOF-261, -262 and -263 are at 538, 528 and 516 nm, respectively	22
Figure 2.11. (a) LMOF-263 optical emission in the solid-state and as a suspension in water (0.25 g/L). (b) Emission spectra of LMOF-263 after incremental additions of an aqueous Hg^{2+} solution and (c) Pb^{2+} solution. (d) Stern-Volmer curves ($\lambda_{\text{ex}} = 365 \text{ nm}$) for heavy and light metal ions, monitoring LMOF-263 selectivity (inset— Hg^{2+} detection at low concentrations)	24
Figure 2.12. (a) PL intensity ratios of LMOF-263 at each Hg^{2+} adsorption and desorption stage of the recycling cycle, and (b) the PXRD patterns after each full cycle to show LMOF-263 stability after the recycling process. The average standard deviations in intensity for the Hg^{2+} and Pb^{2+} exposures were 1.811 a.u. and 1.799 a.u., respectively	25
Figure 2.13. Emission spectra from the low concentration fluorescence titration of LMOF-263 with aliquots of Hg^{2+} solution, with enhanced detail provided in the inset	26
Figure 2.14. Stern-Volmer curves for LMOF-261, -262 and -263 after exposure to Hg^{2+} through fluorescence titrations	27

Figure 2.15. (a) PL intensity ratios of LMOF-263 at each Hg^{2+} adsorption and desorption stage of the recycling cycle, and (b) the PXRD patterns after each full cycle to show LMOF-263 stability after the recycling process	28
Figure 2.16. Metal ion concentrations after exposure to 5, 10 or 15 mg of LMOF-263 in 35 mL solutions	29
Figure 2.17. The remaining Hg^{2+} concentrations after exposure to various amounts of LMOF-263 in mixed metal solutions (initial concentrations: 10 ppm M^{2+} , as specified in the legend).....	30
Figure 2.18. (a) Hg^{2+} concentrations after exposure to LMOF-263 for various time intervals. (b) The amount of adsorbed Hg^{2+} as a function of exposure time. The inset shows the pseudo-second-order kinetic plot for Hg^{2+} adsorption (initial Hg^{2+} concentration: 10 ppm)	31
Figure 2.19. PXRD overlay of LMOF-263 samples, demonstrating structural effects with increased exposure to Hg^{2+}	33
Figure 2.20. Molar ratio of Hg/Zn (blue dots) in LMOF-263 samples after exposure to 10, 100, 1,000, 10,000, 20,000 and 30,000 ppm Hg^{2+} solutions. These values represent averages over three trials. The error bars represent the average standard deviation of the molar ratio ($\pm 0.152 \text{ Hg}/\text{Zn}$) over all concentrations	33
Figure 2.21. FTIR spectra for LMOF-261 and LMOF-263. Black labels are used to identify peaks related to the sulfone and other sulfur related moieties (LMOF-263), while blue labels show peaks concerning the carbonyl group (LMOF-261)	35
Figure 2.22. XPS spectra for as-made LMOF-263	36

Figure 2.23. XPS spectra of LMOF-263 exposed to water (no Hg) as reference. No trace Hg^{2+} is detected after the water treatment throughout the analysis.....	36
Figure 2.24. XPS spectra of LMOF-263 exposed to 100 ppm Hg^{2+}	37
Figure 2.25. XPS spectra of LMOF-263 exposed to 1,000 ppm Hg^{2+}	37
Figure 2.26. XPS spectra of LMOF-263 exposed to 10,000 ppm Hg^{2+}	38
Figure 2.27. XPS spectra of LMOF-263 exposed to 30,000 ppm Hg^{2+}	38
Figure 2.28. XPS spectra of LMOF-263 exposed to 20,000 ppm Mg^{2+}	39
Figure 2.29. Overlaid XPS spectra of LMOF-263 exposed to incremental Hg^{2+} concentrations. The sulfur binding energy increases (curves shift to the right) when exposed to higher Hg^{2+} concentrations	40
Figure 2.30. Interaction mechanism of Hg^{2+} with the sulfone functional group	42
Figure 3.1. (a) Pristine LMOF-271 crystals in the mother liquor, (b) filtered and washed with DMF and (c) under 365 nm excitation.....	46
Figure 3.2. (a) N_2 adsorption (solid) and desorption (void) isotherms for LMOF-271. (c) The H-K micropore size distribution analysis. The nonuniform pore size indicates various pore dimensions along LMOF-271	48
Figure 3.3. Thermogravimetric analysis (TGA) of pristine LMOF-271	49
Figure 3.4. Optical absorption spectra (converted to KM function) of LMOF-271 (blue) and tpe (orange)	50

Figure 3.5. Optical emission and excitation spectra for pristine (blue) and activated (red) LMOF-271. The displayed emission spectra were monitored under $\lambda_{\text{ex}} = 365$ nm, while the excitation spectrum was monitored at 475 nm. The LMOF-271 excitation spectrum does not change after activation.....50

Figure 3.6. (a) Each Zn^{2+} is five-coordinate, having a Zn-N bond with one chromophoric tppe and four Zn-O bonds with four adc linkers. (b) The Zn-based SBU is a paddle-wheel-type structure with adc linkers extending into the *ab*-plane, and tppe ligands expanding the framework along the *c*-axis. (c) LMOF-271 viewed along the *b*-axis, showing edge-sharing hexagonal and triangular 1D channels. This further depicts the 2D sheets of Zn SBUs and adc linkers that are connected through tppe ligands. (d) The same net portrayed down the *c*-axis, showing tetragonal 1D channels that are heavily occupied with anthracene groups from the adc linkers. Anthracene groups have different orientations throughout the 1D channel52

Figure 3.7. PXRD pattern of simulated LMOF-271 overlaid with those of LMOF-271 exposed to various experimental conditions. The small peak at $\sim 4^\circ$ 2θ that was determined through the simulated pattern only arises after LMOF-271 activation (green pattern)53

Figure 3.8. (a) The optical emission spectra of pristine (black) and THF-suspended LMOF-271 (orange—0 h, blue—15 h, $\lambda_{\text{ex}} = 365$ nm). (b) The emission enhancement of LMOF-271 as the sensor is exposed to incremental amounts of CTC ($\lambda_{\text{ex}} = 365$ nm). Emission spectra were recorded 8 min after the increase in CTC concentration. (c) Stern-Volmer curves for various chloromethane solvents. LMOF-271 displays a highly selective signal response to CTC (blue) over CLF (orange) and DCM (green)55

Figure 3.9. Stern-Volmer curve for LMOF-271 when exposed to CTC. Error bars indicate the average standard deviation of I/I_0 values between multiple trials of PL titrations. The inset equation describes the linear relationship between I/I_0 and CTC concentration at low values. The slope represents the fluorescence enhancement efficiency, K_{SV}	56
Figure 3.10. The overlay of emission spectra from the low concentration fluorescence titration of LMOF-271 with aliquots of CTC. Detection of 25 ppb (blue) is clearly detected	57
Figure 3.11. PL intensity ratios of LMOF-271 at each stage of the CTC exposure and washing portions of the recycling analysis. The red dot indicates that the fluorescence signal was not enhanced to the same level as the previous two cycles. At this stage there was drastic color change in the solid LMOF-271, indicating degradation of the structure	58
Figure 4.1. ^1H -NMR of H_2dsab with integrations and functional group assignments (inset). The shifts at 3.3, 2.5, and 2.09 ppm correspond to water and residual solvents (DMSO, acetone)	63
Figure 4.2. PXRD pattern comparison between PCN-133 and LMOF-321 exposed to various conditions	64
Figure 4.3. (left) N_2 adsorption and desorption isotherms for LMOF-321. (right) The H-K micropore size distribution analysis of LMOF-321, indicating nanopores in the range of 5.8-6.1 Å	65
Figure 4.4. Thermogravimetric (TG) analysis of as-made (solid) and activated (dotted) LMOF-321	66
Figure 4.5. Optical absorption spectra (converted to KM Function) of as-made LMOF-321 (orange) and H_3btb (blue)	67

Figure 4.6. Optical emission and excitation spectra for LMOF-321 (as-made and activated) and H₃btb. Values in parentheses provide the emission or excitation wavelength at which the displayed excitation or emission spectra, respectively, were monitored67

Figure 4.7. (a) LMOF-321 optical emission when immersed in water (0.25 g/L) initially and after 15 h. The inset depicts LMOF-321 emission stability during seawater exposure. (b) Emission spectra of LMOF-321 after incremental additions of an aqueous Li⁺ solution under pH 7, (c) pH 8, and (d) pH 10. (e) PL titrations of LMOF-321 with Li⁺ in seawater (pH 7.6). All emission spectra had $\lambda_{\text{ex}} = 365$ nm72

Figure 4.8. (a) Stern-Volmer (S-V) curves ($\lambda_{\text{ex}} = 365$ nm) of LMOF-321 for alkali and alkaline earth metals. High selectivity for Li⁺ is clearly visible. (b) S-V curves comparing the PL signal change from LMOF-321 and PCN-133 during Li⁺ exposure. (c) Low-concentration Li⁺ titrations immersed in pH 7 (green), seawater (pH 7.6, blue), pH 8 (orange) and pH 10 (purple). Equations represent the S-V relationship, with K_{SV} values provided under each condition. Average standard deviation values for pH = 7, 7.6, 8, and 10 titrations were 0.897, 0.849, 0.775, and 0.665 a.u., respectively74

Figure 4.9. (a) Optical emission spectra of LMOF-321 as-made (black) and after successive Li⁺- (blue) and HCl-exposures (red). A maximum emission within $\pm 6\%$ of the as-made and initially Li⁺-quenched spectra were considered recycled. Pink and purple spectra correspond to PL emissions from degraded products. (b) PXRD overlay of LMOF-321 samples after each successive regeneration cycle. The red diffraction pattern represents a breakdown of the framework after five full cycles. (c) PL intensity ratios of LMOF-321 at each Li⁺-adsorption and -desorption stage of the regeneration cycle76

Figure 4.10. (a) The remaining metal concentrations after exposure to various amounts of LMOF-321. (b) Residual Li^+ concentrations from mixed-metal solution exposures.....77

Figure 4.11. (a) Li^+ concentrations after exposure to LMOF-321 for various time intervals. (b) The amount of adsorbed Li^+ as a function of exposure time. The inset shows the pseudo-second-order kinetic plot for Li^+ adsorption (initial Li^+ concentration: 10 ppm), which was used to determine the kinetic rate constant ($0.0056 \text{ g mg}^{-1} \text{ min}^{-1}$).....79

Figure 4.12. Adsorption isotherm of Li^+ on LMOF-321. The inset shows experimental values fit with the Langmuir model.....80

Figure 4.13. FTIR spectra for pristine H_2dsab and LMOF-321 samples [reference to KBr pellet in vacuum ($<20 \text{ mTorr}$)]. Black labels are used to identify peaks related to the sulfone and imide moieties. (a) The spectrum for the pristine H_2dsab ligand, highlighting peaks representing the imide and sulfone groups. (b) The spectrum of LMOF-321 exposed to water is compared with (c) LMOF-321 after exposure to $\text{Li}^+_{(\text{aq})}$ solution. The top difference spectrum, obtained by subtracting spectrum b from c, shows the perturbations of the asymmetric and symmetric sulfone vibrational modes after Li^+ -exposure81

Figure 4.14. XPS spectra of LMOF-321 exposed to water (no $\text{M}^{+/2+}$) as reference, and 1,000 ppm solutions of Ca^{2+} and Li^+ . The shift in N 1s binding energy observed in both exposures indicates direct interaction with the imide in the bis(sulfonyl)imide functional group82

CHAPTER 1: Introduction

1.1 LMOF Background

Metal-organic frameworks (MOFs) are a type of material classified as coordination polymers with open frameworks that contain potential voids.¹ MOFs are constructed via self-assembly of metal cations, or clusters, and polydentate organic ligands, producing one, two, or three-dimensional coordination networks.² The crystallinity of these systems enables X-ray diffraction techniques to provide precise structural information. These materials can be chemically modified to insert functionalities at definite locations—coupled with adjustable porosity, these desirable characteristics have prompted the use of MOFs towards several applications, including gas storage and separation,³⁻⁴ catalysis,⁵⁻⁶ sensing,⁷ drug delivery,⁸⁻⁹ proton conduction,¹⁰ optoelectronics,¹¹ and imaging.¹² The organic ligands used in MOFs often incorporate aromatic or conjugated π groups that not only provide a rigid backbone towards a stable structure, but can also be photo-excitable and discharge optical emission.

Luminescent MOFs (LMOFs) represent a growing subcategory of MOFs, which emit light upon excitation. Photoluminescence (PL) results when photon energy is used to excite the material. Due to the variation in LMOF structures, which often include many types of inorganic nodes, organic ligands, and guest molecules, the photoluminescence mechanism can be vastly different between materials. The focus of this work lies on LMOFs that display ligand-based emission—in such cases, the inorganic components or guest molecules within the framework make negligible contributions to the emission. However, the interplay between multiple-linker systems facilitates electron-transfer mechanisms that alter the optical properties of the system compared to the molecular chromophores, or the individual luminescent organic ligands.¹³ Permanent porosity, a characteristic of select LMOFs, enables the material to constrain target analytes, or specific

chemical species under direct observation, within the channels and promote effective interactions with specific functionalities. The locations of these moieties are explicitly known from X-ray diffraction studies. These traits are not common among other potential sensor materials and represent an interesting path for detection and preconcentration methods.

1.2 LMOFs as Sensors

Within a certain type of medium, a specific analyte may enter the pores of an LMOF and interact with organic ligands within the confined cavities. Whether the interaction site exists on a chromophore or a functionalized co-linker, the electronic properties of the LMOF change and a detection signal is generated—this response is similar to observations in small molecule and conjugated polymer systems.¹⁴⁻¹⁵ Immobilization of optically-active ligands into the LMOF promotes higher internal quantum yield (IQY) values compared to the molecular chromophore¹⁶⁻¹⁷ and limits self-quenching from aggregation after exposure to analytes. IQY represents the ratio between emitted and absorbed photons from an optically active material.

A change in the photoluminescence intensity or wavelength can be used as a detection signal to identify the presence of analyte within a LMOF. Emission intensity variation is the most common mode of detection, with enhancement or quenching of the PL dependent on the electronic properties of the organic ligands and/or target analytes under investigation. Several characteristics of LMOFs need to be considered before application towards specific analytes. Pore apertures can be adjusted depending on the size and morphology of incorporated organic ligands, which usually include π -conjugated components. However, additional functionalities on the optically-active linkers or structural co-linkers could diminish the pore window. These functionalities also have a drastic effect on the chemical environment within the LMOF channels, including acidity/basicity,

polarizability, hydrophobicity, etc. These factors need to be individually managed to formulate ideal LMOFs to interact with specific guest species.

When selecting metal ions for assembly into the LMOF, it is important to consider how these inorganic components will participate in the luminescence mechanism. Paramagnetic ions (Mn^{2+} , Co^{2+} , Ni^{2+} , Cu^{2+}) are known to quench luminescence through the activation of energy or electron transfer processes from the photo-excitabile organic ligand.¹⁸ Commonly used metal ions for LMOF assembly include d^{10} metal ions, such as Zn^{2+} or Cd^{2+} , due to the low-energy, fully filled core-orbitals that do not participate in luminescence mechanisms, promoting ligand-based emission from the system.¹⁹ However, in order to solve issues with LMOF stability in certain environments, highly valent metal ions have been used to increase the bond strength with carboxylate-based ligands, resulting in rigid secondary building units (SBUs).²⁰⁻²² The LMOF bandgaps may be altered from similar systems using d^{10} metal ions,²³ however these robust SBUs with a larger coordination sphere could lead to further interaction pathways through open-metal sites in addition to stability enhancements.

Aside from stability, LMOFs must exhibit sensitivity and selectivity to be effective sensor materials. A focus of the research presented in this dissertation focuses on the synthesis and incorporation of functionalized co-linkers that were designed to interact with target analytes over similarly structured guests.

1.3 Advantages of Dual-Ligand LMOFs

It is difficult to maintain effective and selective interactions with analytes using a single ligand; it would have to be photoluminescent under specific irradiation and chemical conditions (pre- and post-exposure to target species) while promoting guest-host interactions to occur through functionalization and/or physical confinement. Chemical modification on a chromophore may

interrupt its electronic properties and quench luminescence. The presence of an interaction site on the optically-active ligand in a LMOF could lead to enhanced detection sensitivity, but there are many variables to regulate (pore window constraints, framework stability, excitation wavelength, etc.) when using a single-ligand system.

Dual-ligand LMOFs consolidate organic groups with a variety of properties and often lead to materials with interesting and useful structures that would not result from single-ligand systems. These dual-ligand materials have been difficult to synthesize due to the competitive formation of thermodynamically- and kinetically-favored products. The metal-ligand bonds are often exothermic, and certain linkers may coordinate more slowly due to steric or electronic effects from chemical functionalities.²⁴⁻²⁶ Reaction pathways have been optimized in the presented work, and mechanisms for multivariate LMOF preparation vary dependent on the metal source, organic ligands, solvent conditions, etc.

The level of variation achieved with dual-ligand LMOFs cannot be matched by single-ligand systems. Porosity and surface chemistry can be easily adjusted through small alterations in the co-linker.²⁷ Switching the organic component in a single-ligand LMOF may result in drastic optical or structural mutations from the original material. Due to the separation between functionalized co-linkers (guest-host interaction sites) and chromophores, the emission profile from an LMOF can be easily predicted. Additionally, along with the knowledge of precise interaction site locations from X-ray diffraction analyses, the functionalities on co-linkers can be modified between similarly-structured materials without detrimental quenching effects. A systematic study can be implemented to determine ideal LMOF sensors towards specific analytes. The tailorable pores and surfaces within dual-ligand LMOFs also provide opportunities for adsorption, extending the application of this class of materials. Dual-performances in detection

and adsorption of target analytes are outlined in this work, establishing methods to simplify remediation efforts and industrial procedures.

CHAPTER 2: Simultaneous Detection and Extraction of Heavy Metals from Water

2.1 Introduction

Effective detection and removal of toxic heavy metals (Hg^{2+} , Pb^{2+} , Cd^{2+} , etc.) from water sources are paramount to regions spanning the globe. Pollution from mines, factories or even poorly constructed water supply pipes lead to devastating effects on the environment and vital biological processes, including human health. Recent crises involving drinking water contamination in Flint, Michigan and Newark, New Jersey have proved that these issues don't just exist within developing nations—heavily industrialized areas and cities with antiquated water regulations have a direct and detrimental effect on our drinking water supplies.²⁸ Alternatively, agricultural communities in under-industrialized areas have high concentrations of heavy metals in groundwater (from assorted agrochemicals, textiles, metallurgy, etc.).²⁹ Not only does contaminated groundwater affect drinking supplies, but these metals also leach into the soil and accumulate in plants and animals. This expands the number of exposed people and ecosystems beyond the agricultural communities.

The ability to detect ultra-low levels of toxic metals is of emerging importance. To remediate water supplies, it is best to detect toxic metals as early as possible, before the concentrations increase, accumulate in the local environment and cause considerable damage. Previous studies have used a variety of materials that have lowered the threshold for detection. Electrochemical methods³⁰⁻³³ for the detection of mercury have vastly lowered sensing limits, however these methods are expensive, cumbersome and require higher technical prowess.

Techniques that measure sample absorbance to detect trace mercury levels³⁴⁻³⁶ have allowed for more portable instrumentation, but it has been shown that fluorescence based sensors have lower detection limits.³⁷

The possibility of synthesizing new fluorescent materials that selectively bind heavy metals has drawn further attention.³⁸⁻⁴⁰ Luminescent metal-organic frameworks (LMOFs) have recently been developed as chemical sensors due to their high porosity, tunability and mild synthetic conditions.^{18, 41-47} Most of the previous studies making use of LMOFs for heavy metal detection have focused on functionalized prototype materials to increase selectivity for toxic metal ions or to enhance luminescence, without addressing their capture/removal potential from aqueous solution.⁴⁸⁻⁵⁴ Other studies have centered on tailoring MOFs to boost their uptake capacity for heavy metal ions, without providing fluorescence-based quantitative detection ability for these contaminants.⁵⁵⁻⁵⁷ Obtaining a material that can simultaneously detect and remove heavy metals from water would greatly enhance the water remediation process, although research that places a spotlight on both functionalities is sparse.⁵⁷⁻⁵⁸

Effective fluorescence detection and adsorption of heavy metals relies on both selectivity and sensitivity — namely the signal responses must be sensitive to the change in concentration and interactions should be analyte specific.^{57, 59-60} Dual-ligand MOFs that offer both luminescence and targeted functionality provide a unique scaffold that can echo these important properties.⁶¹⁻⁶²

Following these guidelines, we have recently developed a new strategy to design highly porous and strongly luminescent MOFs (LMOFs) for possible use as dual-functional fluorescence sensors and adsorbents.^{17, 63-64} By incorporation of a chromophore-based ligand along with a structure-modulating co-ligand,⁶⁵ we have succeeded in synthesizing a number of LMOFs with high stability, specified porosity, surface functionality, targeted emission energy and strong

luminescence. For example, the combination of a green-emitting chromophore and a tricarboxylate co-ligand leads to LMOF-251 with desired yellow emission and significantly enhanced fluorescence IQY.¹⁷

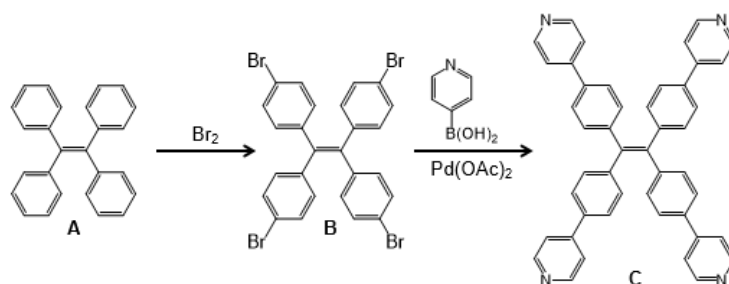
The aforementioned characteristics make these LMOFs promising candidates for selective detection and effective capture of heavy metals. In this study, we report the design and synthesis of a series of isorecticular LMOFs⁶⁶ built on tpe chromophore and a dicarboxylate-based co-ligand with varying functional moieties and a detailed study of their heavy metal detection and uptake potential. We show that the LMOF with thio-functionalization exhibits extremely sensitive and selective optical detection of heavy metals over nonhazardous lighter metals, as well as high performance in the removal of heavy metals from aqueous solution.

2.2 Experimental Details

2.2.1 Ligand Syntheses

Synthesis of 4-tpe

1,1,2,2-tetraphenylethene (tpe, **A**) powder was reacted with liquid bromine to produce 1,1,2,2-tetrakis(4-bromophenyl)ethene (Br₄-tpe, **B**) and further purified via recrystallization in methylene chloride/methanol. To attach the pyridine moiety to the tetradentate segment, a Suzuki coupling was carried out (Scheme 2.1) between Br₄-tpe and pyridine-4-boronic acid, catalyzed by

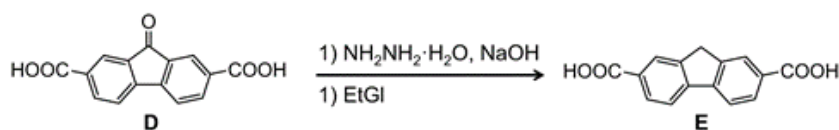


Scheme 2.1. tpe synthesis.

palladium(II) acetate. The fluorophore 4-ttpe [1,1,2,2-tetrakis(4-(pyridine-4-yl)phenyl)ethane, **C**] product was synthesized according to literature procedures.¹⁷ Product yield was 75%.

Synthesis of *H*₂hfdc

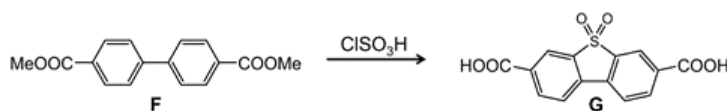
The linker *H*₂hfdc (**E**) was synthesized through use of the Huang Modification.⁶¹ *H*₂ofdc [9-oxo-9*H*-fluorene-2,7-dicarboxylic acid] (**D**) (3 g, 11.2 mmol) and NaOH (2.64 g, 6 equiv.) were mixed with hydrazine monohydrate (2.25 mL, 16 equiv.) and ethylene glycol (100 mL) for 12 h at reflux, outlined in Scheme 2.2 below. Hydrazine monohydrate was evaporated from the mixture and the temperature raised to keep the ethylene glycol at reflux. After the reaction ceased, the solution was neutralized using excess water, and the pH was slowly decreased to ~1 using aliquots of concentrated HCl. The orange solid (2.5 g, 86% yield) was filtered and washed with excess water.



Scheme 2.2. *H*₂hfdc synthesis.

Synthesis of *H*₂dbtdcO₂

The sulfone-functionalized ligand *H*₂dbtdcO₂ [**G**, dibenzo[*b,d*]thiophene-3,7-dicarboxylic acid-5,5-dioxide} was synthesized according to the work of Olkhovik et al.⁶⁷ Dimethyl biphenyl-4,4'-dicarboxylate (**F**, 5 g, 18.5 mmol) was dissolved in chlorosulfonic acid (21.57 g, 10 equiv.), depicted in Scheme 2.3. The mixture was heated at reflux for 3 h, or until no more HCl was produced as a by-product. At this time, the mixture was poured onto crushed ice to quench the



Scheme 2.3. *H*₂dbtdcO₂ synthesis.

reaction. White solid was separated via vacuum filtration, washed with water and dried to produce $\text{H}_2\text{dbtdcO}_2$ (4.5 g, 80% yield).

2.2.2 Isorecticular MOF Syntheses

Synthesis of $\text{Zn}_2(\text{ofdc})_2(\text{tppe})$ (LMOF-261)

Solvothermal reactions of $\text{Zn}(\text{NO}_2)_2 \cdot 6\text{H}_2\text{O}$ (0.030 g, 0.1 mmol), tppe (0.024 g, 0.4 mmol) and ofdc (0.0134g, 0.05 mmol) in a mixed solvent system (DMA:iPrOH:DMSO, 4:1:1) were prepared in 20 mL glass vials. The reaction mixture initially was kept under sonication until all solids were dissolved, then the vials were kept at 150 °C for 24 h. After the reaction mixture was cooled to room temperature, the yellow needle-shaped crystals were collected via vacuum filtration and washed with DMA.

Synthesis of $\text{Zn}_2(\text{hfdc})_2(\text{tppe})$ (LMOF-262)

Solvothermal reactions of $\text{Zn}(\text{NO}_2)_2 \cdot 6\text{H}_2\text{O}$ (0.015 g, 0.05 mmol), tppe (0.019 g, 0.3 mmol) and hfdc [9H-fluorene-2,7-dicarboxylic acid] (0.025 g, 0.1 mmol) were prepared similarly to LMOF-261 reactions, instead reacting at 120 °C for 3 d. Orange rod crystals were filtered after the reaction was brought to room temperature and washed with DMA.

Synthesis of $\text{Zn}_2(\text{dbtdcO}_2)_2(\text{tppe})$ (LMOF-263)

Solvothermal reactions of $\text{Zn}(\text{NO}_2)_2 \cdot 6\text{H}_2\text{O}$ (0.030 g, 0.1 mmol), tppe (0.024 g, 0.4 mmol) and $\text{H}_2\text{dbtdcO}_2$ [dibenzo[*b,d*]thiophene-3,7-dicarboxylic acid 5,5-dioxide] (0.030 g, 0.1 mmol) were prepared similarly to LMOF-261 reactions. After the reaction mixture was cooled to room temperature, pale yellow needle-shaped crystals were collected via vacuum filtration and washed with DMA.

2.2.3 Structural Analysis of LMOF-261

Single crystal X-ray diffraction data for LMOF-261 were collected on a Bruker D8 diffractometer with PHOTON 100 detector using the synchrotron source ($\lambda = 0.7749 \text{ \AA}$) at the Advanced Light Source 11.3.1 Chemical Crystallography beamline (Table 2.1). All non-hydrogen atoms were refined anisotropically; hydrogen atoms were placed geometrically, constrained and refined with a riding model. The unresolvable electron density from the void space in the structure was removed by SQUEEZE.

Table 2.1. Single crystal data of LMOF-261.

Compound	LMOF-261
Formula	$\text{C}_{38}\text{H}_{22}\text{N}_2\text{O}_5\text{Zn}$
M	651.94
Crystal system	Tetragonal
Space group	$I4_1/a$
a/ \AA	33.9529(14)
b/ \AA	33.9529(14)
c/ \AA	17.1833(8)
$\alpha/^\circ$	90
$\beta/^\circ$	90
$\gamma/^\circ$	90
V/ \AA^3	19808.9(19)
Z	16
Temperature/K	100(2)
l (radiation wavelength)/ \AA	0.7749
D (g/cm^3)	0.874
Reflections collected	126056
R1 ^a [$I > 2\sigma(I)$]	0.0585
wR2 ^b [$I > 2\sigma(I)$]	0.1516
Goodness-of-fit	1.066
CCDC No.	1478942

$$^a \text{R1} = \sum |F_o - F_c| / \sum |F_o|$$

$$^b \text{wR2} = \sum [w(F_o^2 - F_c^2)^2] / \sum w(F_o^2)^{1/2}$$

The powder X-ray diffraction (PXRD) patterns were collected on a Rigaku Ultima-IV diffractometer using monochromatic Cu K_α radiation ($\lambda = 1.5406 \text{ \AA}$). Data were collected between $3\text{--}45^\circ 2\theta$ with step size 0.02° and scanning rate $2.0^\circ/\text{min}$. PXRD patterns were obtained for the as-

made crystal samples, shown in Figure 2.1. The crystal morphologies change slightly within the isorecticular series, yet the PXRD patterns contained identical peaks (Figure 2.1, 2.2). Crystal colors were consistent with the color of the dicarboxylate linker used in the solvothermal reaction. Only powder samples of LMOF-263 could be synthesized for this analysis.

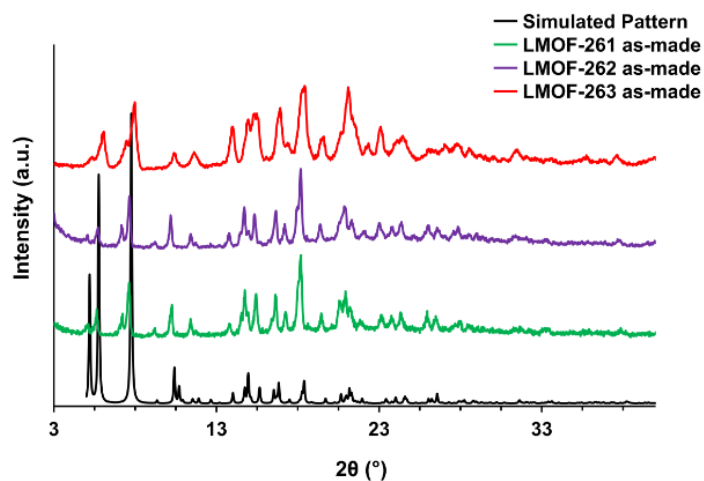


Figure 2.1. PXRD patterns of the LMOF isorecticular series (LMOF-261, -262 and -263).

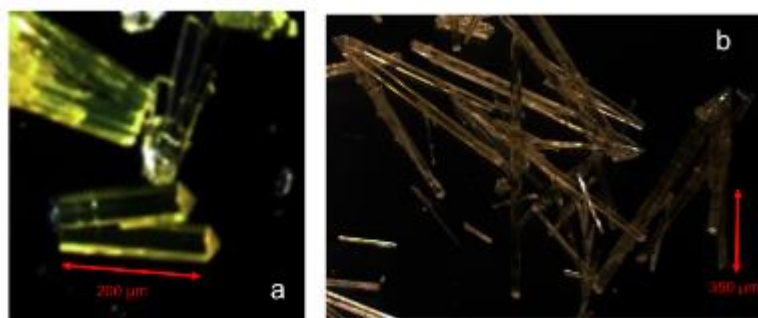


Figure 2.2. Crystal images of (a) LMOF-261 and (b) LMOF-262.

Figure 2.3 portrays the remarkable stability of LMOF-263 at various pH values and water exposure times. The material was stable in water for 2 weeks, and relatively stable in pH 4-10 for 15 h.

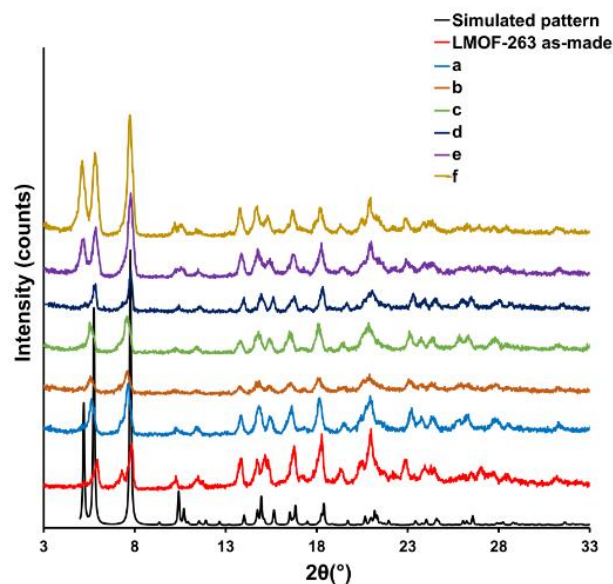


Figure 2.3. LMOF-263 is stable under a variety of conditions, including a) in water for 24 h and b) 2 weeks. Also, LMOF-263 stayed relatively stable exposed to pH c) 4, d) 6, e) 8 and f) 10 for 15 h, with the low angle peaks showing increased crystallinity under basic conditions.

2.2.4 Additional Instrumental Details

Thermogravimetric Analysis of LMOF-261, -262, and -263

Thermogravimetric analysis (TGA) was performed using a TA Instruments Q5000 under constant N₂ flow (20 mL/min). Approximately 4 mg of sample was placed into a platinum pan, which was then heated from 30-600 °C at a rate of 10 °C/min. Figure 2.4 displays the three TGA curves for each member of the isorecticular series.

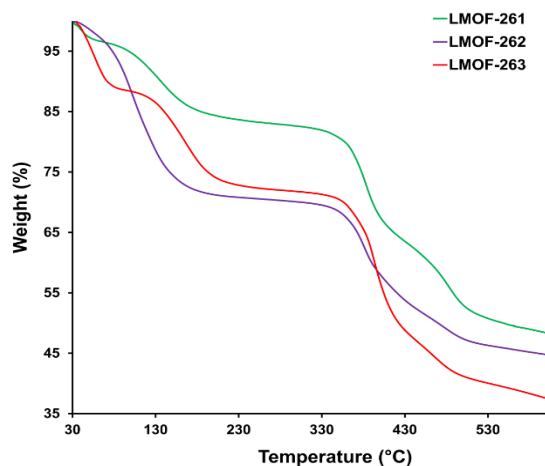


Figure 2.4. Thermogravimetric (TG) analysis of as-made LMOF-261 (green), -262 (purple) and -263 (red).

Optical Characterization Techniques

UV-visible diffuse reflectance spectra were obtained for LMOF-261, -262, -263 and the fluorescent ligand 4-ttpe at room temperature using a Shimadzu UV-3600 spectrophotometer. The diffuse reflectance data was converted to the Kubelka-Munk Function as follows:

$$F(R) = \frac{(1 - R)^2}{2R}$$

Equation 2.1. Kubelka-Munk function $F(R)$, where R is the diffuse reflectance.

Using a Varian Cary Eclipse spectrophotometer, optical excitation and emission spectra were collected for as-made and outgassed solid samples of LMOF-261, -262 and -263. Additionally, internal quantum yield (IQY) was measured using a Hamamatsu C9220-03 spectrophotometer with integrating sphere. Table 2.2 displays IQY data upon 360 nm excitation.

Table 2.2. IQY data for as-made and outgassed samples of LMOF-261, -262 and -263 under 360 nm excitation.

	IQY (%)	
	As-made	Outgassed
LMOF-261	18.2	9.5
LMOF-262	10.7	10.2
LMOF-263	89.2	76.6

Gas Sorption

Gas sorption isotherms of outgassed LMOF-261 and -263 were collected on a Quantachrome Instruments Autosorb-1 MP volumetric gas sorption analyzer using ultra high purity N₂ (99.999%). Liquid nitrogen was used as coolant to achieve cryogenic temperature (77 K). The N₂ isotherm was collected in a pressure range from 10⁻⁷ to 1 atm. The BET surface area was obtained using Autosorb v1.50 software.

Inductively Coupled Plasma Optical Emission Spectroscopy

Inductively coupled plasma optical emission spectroscopy (ICP-OES) analyses were performed using a Spectro Arcos Analyzer with standards from VHG Labs (#SM45-500 and SM70B-500). ICP-OES was used to determine the concentrations of various metal ions (Hg²⁺, Pb²⁺, Ca²⁺ and Mg²⁺) in aqueous solutions after various LMOF-263 exposure conditions.

X-ray Fluorescence Spectroscopy

X-ray fluorescence spectroscopy (XRF) measurements were performed on a Horiba X-ray Analytical Microscope XGT-1000WR, with X-ray tube voltage and current at 50 kV and 60 μ A, respectively. XRF was utilized to determine the relative amounts of Zn²⁺ and Hg²⁺ in LMOF-263 after various Hg²⁺ exposure conditions. As a control, a mixture of ZnO and HgCl₂ (50:50 weight ratio of Zn:Hg) was prepared to make sure the instrument was calibrated properly. The molar ratio

between Zn and Hg in the mixture was 1:0.280, which corresponds to a relative mass of 53.83 and 46.17%, respectively (Table 2.3). The difference between an exact 50:50 ratio can be attributed to error when weighing out the powders.

For further control, relative masses of zinc and sulfur in as-made LMOF-263 were determined (Table 2.3). The LMOF-263 formula $[\text{Zn}_2(\text{dbtdcO}_2)_2\text{tppe}]$, derived from SCXRD analysis on the isorecticular LMOF-261, reveals an equimolar amount of zinc and sulfur. The relative weight percentages of zinc and sulfur in the as-made samples averaged to 67.22 and 32.78%, respectively, or a molar ratio of 1:0.995, consistent with the structural analysis.

Table 2.3. XRF data from a 50:50 (w/w) mixture of $\text{HgCl}_2\text{:ZnO}$ and as-made LMOF-263.

50:50 Mixture of $\text{HgCl}_2\text{:ZnO}$			As-made LMOF-263		
Element	Molar Ratio	Weight Percentage (%)	Element	Molar Ratio	Weight Percentage (%)
Zn	1	53.83	Zn	1	67.22
Hg	0.280	46.17	S	0.995	32.78

Fourier Transform Infrared Spectroscopy

Fourier transform infrared (FTIR) spectroscopy was used to identify the different functional groups in LMOF-261 and LMOF-263. For these measurements, the LMOF-263 powder was gently pressed onto a KBr pellet (~1 cm diameter, 1-2 mm thick). The pellet was placed into a high-pressure, high-temperature cell (product number P/N 5850c, Specac Ltd., UK) at the focal point of an IR spectrometer (Nicolet 6700, Thermo Scientific, US). The samples were activated by annealing under vacuum (<50 mTorr) at 100 °C for at least 1 h, then cooled down to room temperature for FTIR analysis.

X-ray Photoelectron Spectroscopy

X-ray photoelectron spectroscopy (XPS) was employed to further investigate the interaction of Hg^{2+} or Mg^{2+} with LMOF-263. Information regarding changes in local electronic structure of S, C and O as a function of Hg^{2+} or Mg^{2+} can be inferred by monitoring the sulfur binding energy in LMOF-263. The samples were loaded on a KBr pellet (same procedure as in FTIR), using a Perkin Elmer PHI system equipped with a concentric hemispherical analyzer. An Al K α (1486.6 eV) monochromatic X-ray source at a chamber base pressure of <1.0 nTorr was used to excite photoelectrons. Since LMOF-263 is insulating, potential charging was corrected by using a neutralizing flood gun and insuring that the C 1s core level is at 285.4 eV and correcting the other core levels accordingly.

2.2.5 Fluorescence Titrations

An as-made sample of LMOF-263 was placed into water (0.25 g/L) and gently sonicated. LMOF-263 was easily suspended in water. Photoluminescence (PL) titrations were carried out by incrementally adding aliquots of M^{2+} stock solutions to the LMOF-263 suspension and kept under continuous stirring. The fluorescence spectra were recorded 5 min after adding the appropriate amount of M^{2+} stock solution. This exposure time ensured that analyte entered the LMOF pores. Each measurement was repeated three times and the average value was used.

2.3 Results and Discussion

2.3.1 Crystal Structure Analysis

An isorecticular LMOF series has been synthesized by using the tetradentate tpe ligand and several functionalized dicarboxylate linkers as co-ligands. The formation of a group of LMOFs with the same structure and topology using such co-ligands would allow us to study, compare, and understand the difference in their sensing behavior in a direct and systematic manner. Crystals of LMOF-261 were obtained through procedures reported above.

LMOF-261 or $[\text{Zn}_2(\text{ofdc})_2(\text{tppe})]\cdot\text{S}$ (S = solvent guest molecules) crystallizes in the tetragonal crystal system with space group $I4_1/a$. Each Zn^{2+} has distorted tetrahedral coordination to two carboxylate groups from ofdc linkers and two pyridine groups from tppe ligands, forming the PBU (Figure 2.5a). Each PBU is connected to three other PBUs through ofdc linkers to create a distorted square, with four Zn^{2+} in the same plane (Figure 2.5b). This distorted square is further connected by tppe ligands to expand the framework in three dimensions. Viewed down the b-axis, an individual net of LMOF-261 exhibits 1D, edge sharing pentagonal and rhombohedral channels (Figure 2.5b). Along the c-axis, there are two types of 1D channels having square and octagon shaped cross sections, respectively. (Figure 2.5c). The tetrahedral channels have an aperture of ~ 1.7 nm, while the octahedral channels have an aperture of ~ 3.7 nm. These channels proliferate down the c-axis, with carbonyl groups pointed directly into the LMOF channels.

The overall structure of LMOF-261 involves a four-fold interpenetrated framework containing four of these identical nets (Figure 2.5d). When tppe and ofdc are simplified as 4-c nodes, the structure would be a 2-nodal, (4,4)-c net (mot-e type) with four-fold, class IIIa interpenetration. This is a unique net type, according to the ToposPro Database. The interpenetrated structure encloses two types of 1D channels down the c-axis: one having a pentagon-shaped cross section (8.1 Å aperture) and the other, with a narrower tetragon-shaped aperture 7.2 Å in diameter.

The simulated pattern from single crystal X-ray diffraction (SCXRD) on LMOF-261 matched the PXRD patterns of LMOF-262 and -263 samples (Figure 2.1), confirming their structures are isorecticular with respect to the parent LMOF-261.

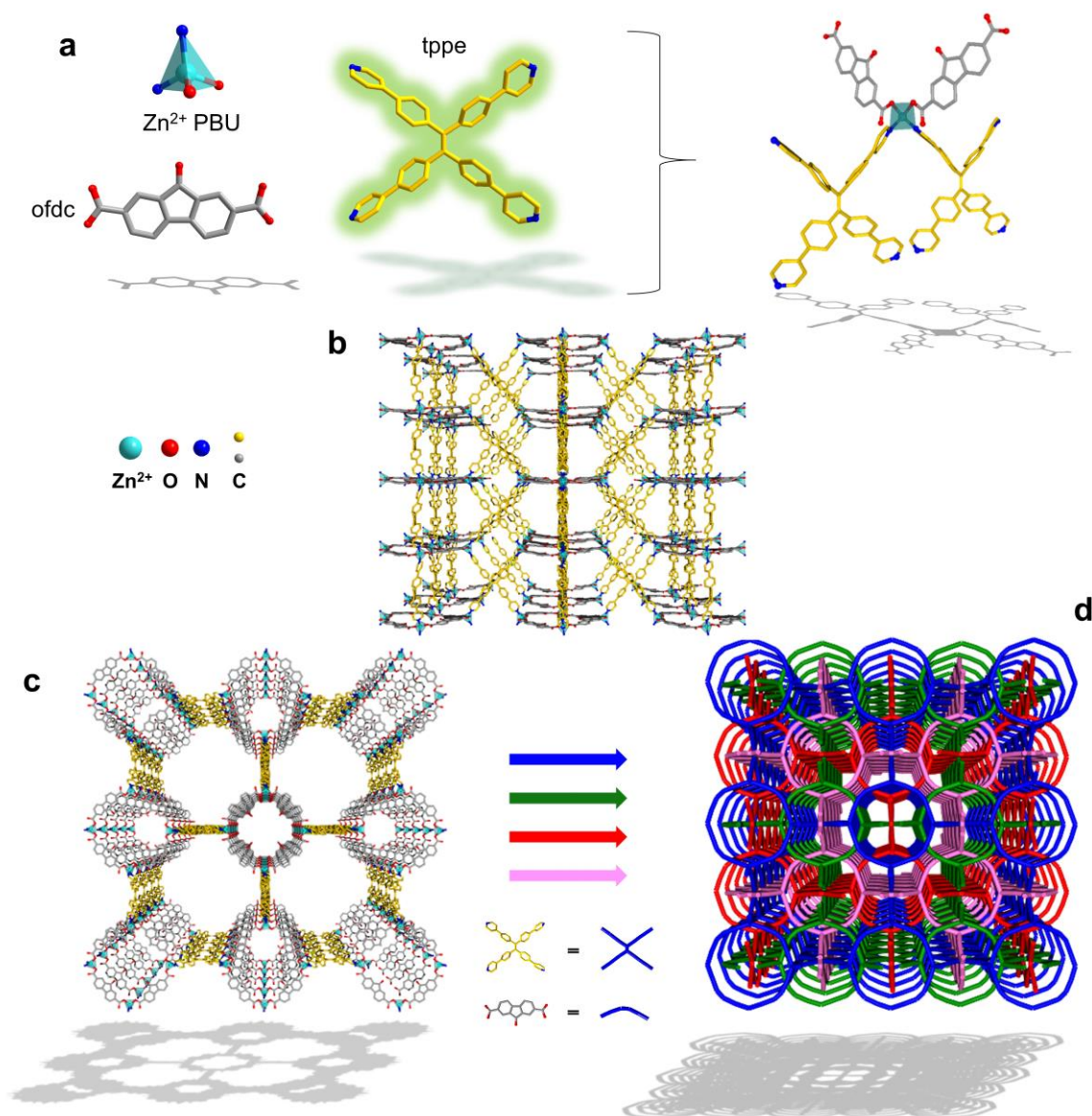


Figure 2.5. (a) The PBU of LMOF-261, depicting a pseudo-tetrahedrally coordinated Zn center bound to two fluorophoric tppe ligands and two ofdc linkers. (b) An individual net of the LMOF-261 framework viewed along the b-axis, containing 1D, edge sharing pentagonal and rhombohedral channels. (c) The same net depicted down the c-axis, showcasing edge sharing octahedral and cylindrical channels. The ofdc linkers point directly into the cylindrical channels extending down the c-axis. (d) Simplified LMOF-261 depicting four-fold interpenetration. Each of the three other nets occupies one octahedral pore of the fourth net to create narrow pentagonal channels, sharing edges from multiple nets.

2.3.2 Pore Characterization

Gas sorption isotherms of LMOF-261 and -263 were collected on a Quantachrome Instruments Autosorb-1 MP volumetric gas sorption analyzer using ultra high purity N₂ (99.999%). Liquid nitrogen was the coolant used to reach cryogenic temperature (77 K). As-made samples of LMOF-261 and -263 were outgassed at 120 °C for 8 h and the subsequent degassed samples were used. LMOF-262 was not stable upon outgassing, so the material was excluded from gas adsorption analyses. N₂ adsorption isotherms for LMOF-261 and -263 are depicted in Figure 2.6. BET surface areas were determined to be 977 and 1004 m²/g for LMOF-261 and -263, respectively.

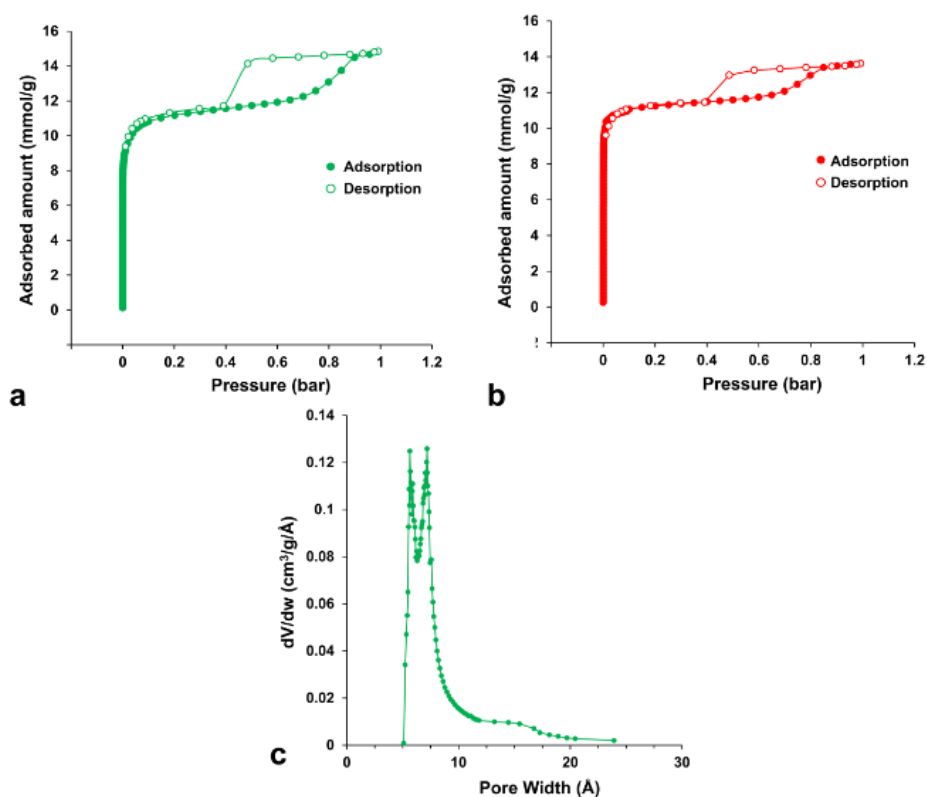


Figure 2.6. N₂ adsorption and desorption isotherms for a) LMOF-261 and b) LMOF-263. c) The H-K micropore size distribution analysis of LMOF-261, indicating micropores in the range of 5-10 Å.

CO₂ adsorption and desorption isotherms (room temperature) were obtained for LMOF-261 and -263. Figure 2.7 shows the CO₂ adsorption isotherm overlay. Uptake maxima were recorded at 1.60 and 2.22 mmol/g for LMOF-261 and -263, respectively. The higher CO₂ uptake for LMOF-263 is consistent with its larger BET surface area. The micropore volumes for LMOF-

261 and -263 were 0.27 and 0.32 cm³/g, respectively—also consistent with the BET surface area values. The micropores would be wide enough to incorporate partially or fully solvated Hg²⁺ ions, respectively.⁶⁸⁻⁶⁹

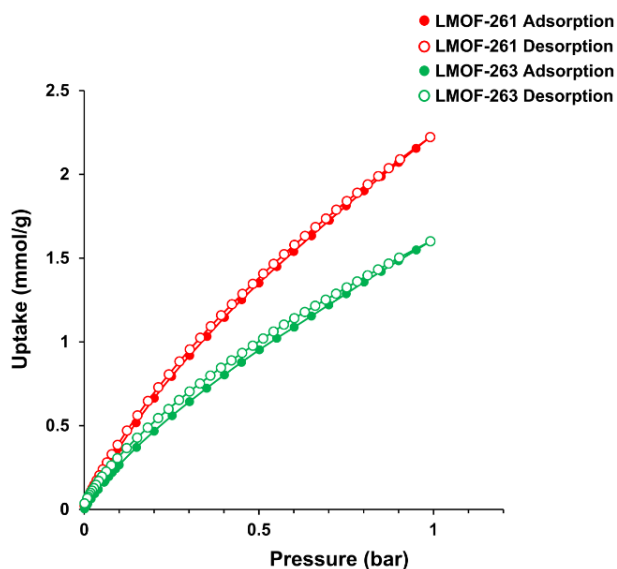


Figure 2.7. CO₂ adsorption and desorption isotherms for LMOF-261 and -263. Uptake maxima increased from LMOF-261 to -263, with 1.60 and 2.22 mmol/g, respectively.

2.3.3 Optical Properties of LMOF-261, -262, and -263

The optical diffuse reflectance spectra of the type ligand and the isoreticular series of LMOFs were collected using a Shimadzu UV-3600 spectrophotometer, after which transformation to the Kubelka-Munk function allowed their optical band gaps to be estimated. The HOMO-LUMO energy gaps of type, LMOF-261, -262 and -263 are estimated to be 2.3, 2.55, 2.65 and 2.7 eV, respectively (Figure 2.8).

Photoluminescence (PL) excitation and emission spectra were collected for samples of the LMOF series at room temperature. The ligand type showed strong green emission when excited by UV light ($\lambda_{\text{ex}} = 365$ nm) with an emission maximum at 500 nm. The emissions of all three

LMOFs are ligand based, with a maximum of intensity at 514, 516 and 464 nm, for LMOF-261, -262 and -263, respectively (Figure 2.9).

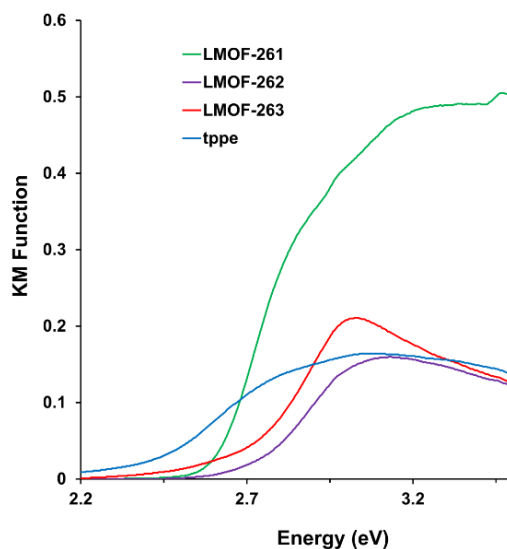


Figure 2.8. Optical absorption spectra (converted to KM Function) of as-made LMOF-261 (green), -262 (purple), -263 (red) and 4-tppe (blue).

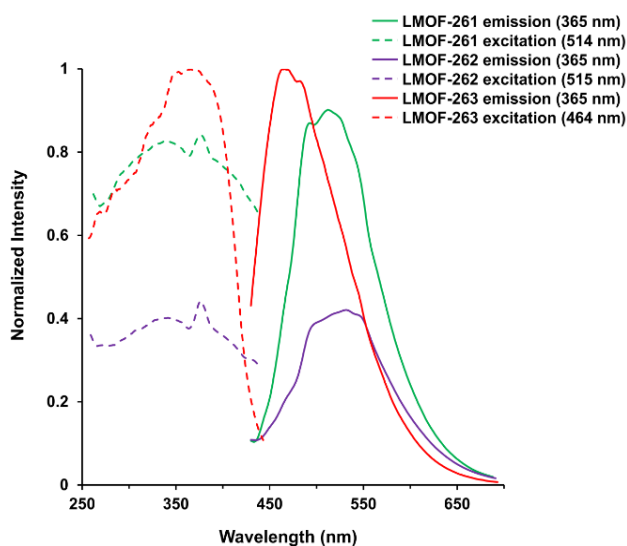


Figure 2.9. Optical emission (solid) and excitation (dotted) spectra of LMOF-261, -262 and -263.

Similar spectra were also collected for outgassed solid samples of LMOF-261, -262 and -263, depicted in Figure 2.10. The emission for each LMOF was red-shifted upon outgassing. Outgassed LMOF-263 demonstrates the most drastic red-shift from the as-made sample, changing

from blue to green emission ($\lambda_{\text{em, as-made}} = 464 \text{ nm}$, $\lambda_{\text{em, outgassed}} = 516 \text{ nm}$) with 365 nm excitation.

LMOF-261 red-shifted from green to yellow emission ($\lambda_{\text{em, as-made}} = 514 \text{ nm}$, $\lambda_{\text{em, outgassed}} = 538 \text{ nm}$)

while the emission from LMOF-262 red-shifted from 515 nm to 528 nm upon outgassing.

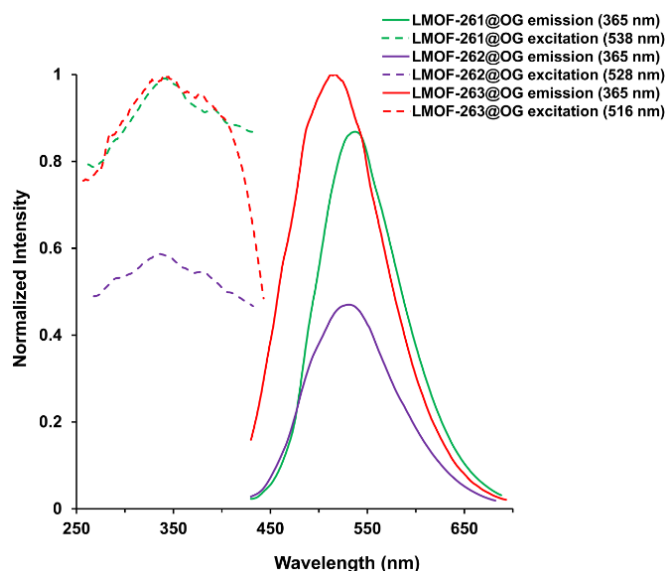


Figure 2.10. Optical emission and excitation spectra for outgassed LMOF-261 (green), -262 (purple) and -263 (red). Values in parentheses provide the emission or excitation wavelength at which the displayed excitation or emission spectra, respectively, were monitored. The emission maxima of outgassed samples of LMOF-261, -262 and -263 are at 538, 528 and 516 nm, respectively.

A comparison among three isorecticular counterparts indicated that LMOF-263 has the highest chemical stability (Figure 2.3) as well as fluorescence IQY (Table 2.2). In addition, the sulfone functional group on the co-ligand, clearly detected by FTIR (Figure 2.21), is likely to enhance the interactions between heavy metal ions and LMOF sensor, and therefore, was chosen as the target system for the subsequent sensing experiments.

2.3.4 Heavy Metal Detection

Heavy metals have been identified as serious water contaminants that lead to the dysfunction of vital biological processes. Simple and highly efficient probes that can be used for on-site measurements are vital to monitor low concentrations of heavy metals in water. On the

other hand, light metals, such as Ca^{2+} or Mg^{2+} , are commonly found in drinking water supplies and provide essential functions in biological processes. Therefore, selectivity for toxic metals over these harmless elements would be an important criterion for fluorescent detectors.

Detection of various metal ions (Hg^{2+} , Pb^{2+} , Ca^{2+} , Mg^{2+}) was accomplished by observing the change in PL signal of an aqueous LMOF-263 suspension before and after addition of the analyte. Figure 2.11a shows the LMOF-263 emission wavelength ($\lambda_{\text{em}} = 464 \text{ nm}$, $\lambda_{\text{ex}} = 365 \text{ nm}$) stays the same in the solid-state or as a suspension in water, yet the intensity is decreased when suspended in water. LMOF-263 was stable in water for 14 days and stable in pH 4-10 for up to 15 hours (Figure 2.3). The emission intensity at 464 nm ($\lambda_{\text{ex}} = 365 \text{ nm}$) decreased when immersed in water, however that intensity was maintained 15 h after the initial immersion (Figure 2.11a). While Hg^{2+} detection could be plagued by formation of nonuniform suspensions,⁷⁰ LMOF-263 forms a uniform suspension in water, promoting its ease as an on-site detection material.

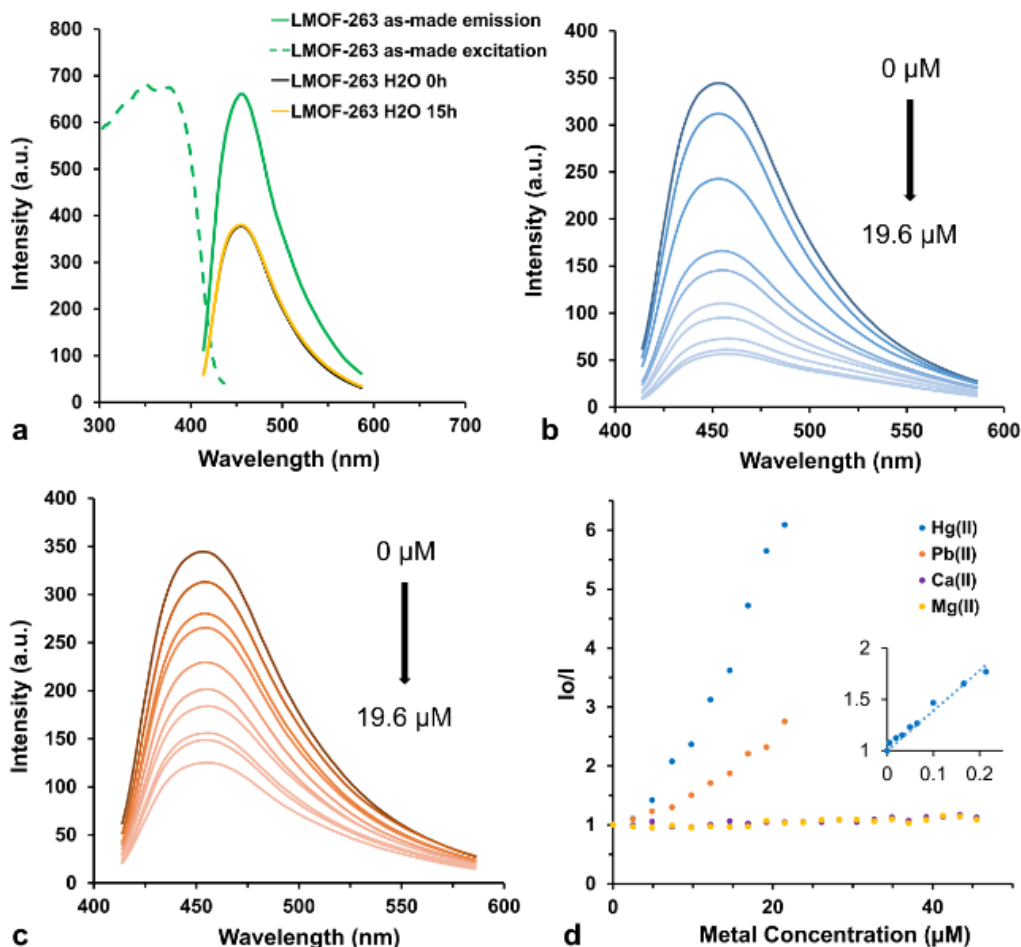


Figure 2.11. (a) LMOF-263 optical emission in the solid-state and as a suspension in water (0.25 g/L). (b) Emission spectra of LMOF-263 after incremental additions of an aqueous Hg^{2+} solution and (c) Pb^{2+} solution. (d) Stern-Volmer curves ($\lambda_{\text{ex}} = 365 \text{ nm}$) for heavy and light metal ions, monitoring LMOF-263 selectivity (inset— Hg^{2+} detection at low concentrations).

Upon addition of M^{2+} solution aliquots, the emission intensity of LMOF-263 was quenched to varying degrees, depending on the M^{2+} analyte and concentration. Approximately 84% of the total intensity of LMOF-263 was quenched upon addition of only $19.6 \mu\text{M}$ of Hg^{2+} (Figure 2.11b), while 64% of the total intensity was quenched when exposed to $19.6 \mu\text{M}$ of Pb^{2+} (Figure 2.11c). The quenching efficiency was quantified using the Stern-Volmer (SV) equation, highlighted in Equation 2.2.

$$\frac{I_0}{I} = K_{SV}[Q] + 1$$

Equation 2.2. Stern-Volmer relationship.

where I_0 is the initial emission peak intensity (pre-exposure to analyte), I is the emission peak intensity after addition of analyte, $[Q]$ is the molar concentration of the analyte (or quencher) and K_{SV} is the Stern-Volmer constant, which can be used to quantitatively measure the performance of LMOF-263 as a sensor for heavy metals (Hg^{2+} and Pb^{2+}). As shown in the inset of Figure 2.11d, at low concentrations, the value I_0/I is directly proportional to metal ion concentration. The K_{SV} was determined to be 459,446 and 55,017 M^{-1} for Hg^{2+} and Pb^{2+} , respectively (Figure 2.12).

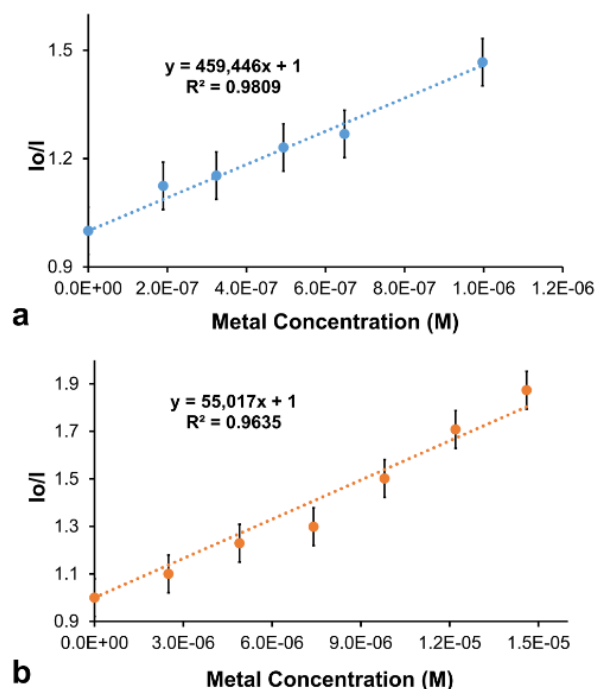


Figure 2.12. (a) PL intensity ratios of LMOF-263 at each Hg^{2+} adsorption and desorption stage of the recycling cycle, and (b) the PXRD patterns after each full cycle to show LMOF-263 stability after the recycling process. The average standard deviations in intensity for the Hg^{2+} and Pb^{2+} exposures were 1.811 a.u. and 1.799 a.u., respectively.

The limit of detection (LOD), defined as the concentration of metal ion at which the decrease in intensity was greater than the average standard deviation in repeated measurements of the same sample, was determined to be 3.3 ppb for Hg^{2+} and 19.7 ppb for Pb^{2+} . These results were confirmed through low-concentration titration of LMOF-263 with aqueous solutions of Hg^{2+} , shown in Figure 2.13 below. The addition of 5 ppb was clearly detected. The Hg^{2+} detection limit of LMOF-263 was on par with all photoluminescent MOFs that have been investigated for heavy metal fluorescence detection and exhibits the second highest MOF K_{SV} value reported to date.⁴⁸⁻

49, 52, 54, 71-74

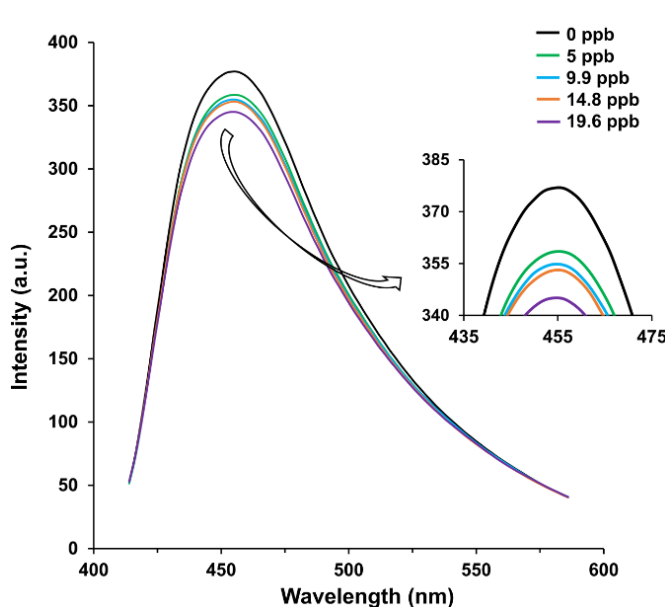


Figure 2.13. Emission spectra from the low concentration fluorescence titration of LMOF-263 with aliquots of Hg^{2+} solution, with enhanced detail provided in the inset.

The only MOF to exhibit a higher quenching efficiency for Hg^{2+} was the heavily studied PCN-224, for which uptake capacity was not reported.⁷⁵ Certain nanomaterials have also demonstrated higher Hg^{2+} K_{SV} values than LMOF-263, however they have no reported adsorption capacity for heavy metals, limiting their use for water remediation efforts.^{52, 76-77} The Pb^{2+} fluorescence detection limit and K_{SV} value exceed the performance of any other luminescent

MOF.^{51, 78-79} In addition to its high sensitivity toward heavy metals, LMOF-263 also exhibits excellent selectivity. Based on the Stern-Volmer plots shown in Figure 2.11d, the K_{SV} values for Ca^{2+} and Mg^{2+} were calculated to be 2,745 and 2,193 M^{-1} , respectively, which correspond to a detection ratio of 167.4 and 209.5 for Hg^{2+}/Ca^{2+} and Hg^{2+}/Mg^{2+} , respectively. These values clearly indicate that LMOF-263 acts as a highly selective detector for heavy metals only.

To compare the effects of different functional groups on the dicarboxylate linkers, LMOF-261, -262 and -263 were exposed to various Hg^{2+} concentrations (following fluorescence titration procedures). Figure 2.14 shows the Stern-Volmer curves for each member of the isorecticular series. LMOF-263, which contains the sulfone functional group, was quenched more efficiently compared to its counterparts. LMOF-261 and -262 contain carbonyl and methylene groups, respectively, on the central position of the dicarboxylate linker. These moieties don't interact as effectively with Hg^{2+} compared to the sulfone group.

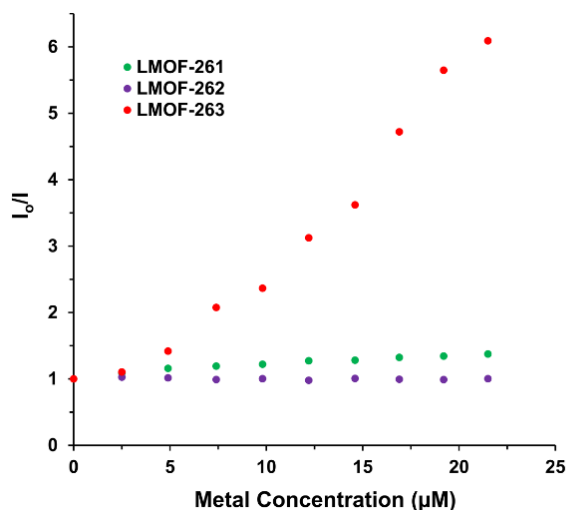


Figure 2.14. Stern-Volmer curves for LMOF-261, -262 and -263 after exposure to Hg^{2+} through fluorescence titrations.

Recyclability of an adsorbent is a highly desirable feature for environmental remediation. After the initial exposure to 10 ppm Hg^{2+} solutions, two additional cycles were carried out on the same MOF sample. The luminescence was fully recovered after each desorption, as determined through PL quenching/enhancement (Figure 2.15a). The structure of LMOF-263 was well maintained during these cycles (Figure 2.15b).

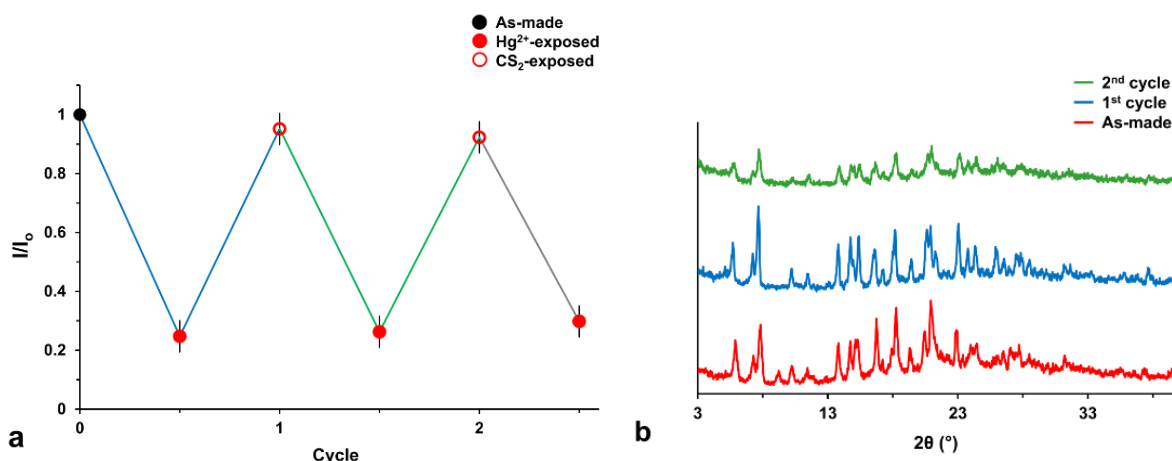


Figure 2.15. (a) PL intensity ratios of LMOF-263 at each Hg^{2+} adsorption and desorption stage of the recycling cycle, and (b) the PXRD patterns after each full cycle to show LMOF-263 stability after the recycling process.

2.3.5 Heavy Metal Removal

Materials with high performances for both detection and capture of toxic/hazardous species are rare. Like detection requirements, selectivity for heavy metals over light metals is important when removing these contaminants from water. To assess the heavy metal removal performance of LMOF-263, as-made samples (5, 10 and 15 mg; 0.20 mM, 0.41 mM and 0.62 mM, respectively) were placed in dilute aqueous solutions (35 mL) of HgCl_2 , PbCl_2 , CdCl_2 , CaCl_2 , and MgCl_2 (concentration of M^{2+} , 10 ppm; ~ 0.350 mg of M^{2+}). After these mixtures were stirred at room temperature for 12 h, the solutions were filtered from the adsorbent and the residual M^{2+} concentrations were determined via ICP-OES. Displayed in Figure 2.16, LMOF-263 lowers the

concentration of Hg^{2+} from 10 ppm to 36 ppb — the adsorbent effectively removes $\sim 99.6\%$ of Hg^{2+} from solution), which is among the highest performances for MOFs.⁵⁷

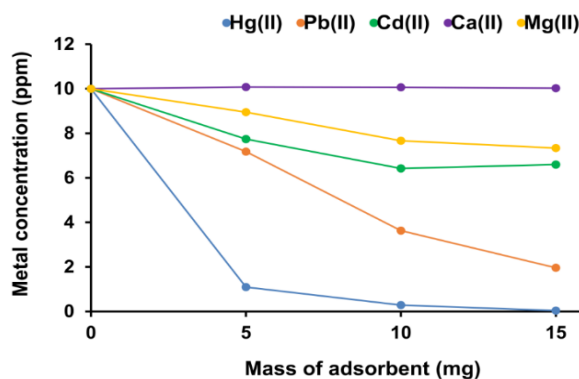


Figure 2.16. Metal ion concentrations after exposure to 5, 10 or 15 mg of LMOF-263 in 35 mL solutions.

LMOF-263 (15 mg, 0.62 mM), when exposed to 35 mL solutions of 10 ppm M^{2+} (~ 0.350 mg M^{2+}), lowers the concentration of Pb^{2+} , Cd^{2+} , Ca^{2+} , and Mg^{2+} to 1.96, 6.60, 10.03 and 7.34 ppm, respectively. LMOF-263 exhibits distinct selectivity towards heavier metals (Hg^{2+} , Pb^{2+}) over lighter metals (Ca^{2+} , Mg^{2+}), as highlighted in Figure 2.16. Even with an increased amount of adsorbent, the concentrations of Ca^{2+} and Mg^{2+} in the post-exposure solutions did not significantly decrease. This is consistent with the detection results shown above.

To further evaluate the selectivity of LMOF-263 for heavy metals over light metals, we carried out adsorption experiments on mixed-metal solutions. Solutions of 10 ppm of Hg^{2+} , Pb^{2+} , Ca^{2+} and Mg^{2+} (35 mL, ~ 0.350 mg of each M^{2+}) were prepared and exposed to 10 and 15 mg amounts of LMOF-263 for 15 h (0.41 and 0.62 mM LMOF-263, respectively). Similar amounts of LMOF-263 were also exposed to solutions of 10 ppm Hg^{2+} as a control and solutions of 10 ppm Hg^{2+} , Ca^{2+} and Mg^{2+} to investigate the interference of Pb^{2+} ions. Figure 2.17 displays the LMOF-263 adsorption performance under these competitive conditions. When all four heavy and light metals are mixed, LMOF-263 clearly shows preference towards Hg^{2+} adsorption—approximately

99.2% of the initial amount of Hg^{2+} was removed, lowering the concentration of Hg^{2+} from 10 ppm to 78 ppb (Figure 2.17, 15 mg LMOF-263). When the same amount of adsorbent was exposed to 10 ppm Hg^{2+} (single-metal solution), 99.6% of the initial Hg^{2+} amount was extracted, lowering the solution Hg^{2+} concentration to 41 ppb. These results provide convincing evidence that LMOF-263 selectively interacts with and captures Hg^{2+} over light metals.

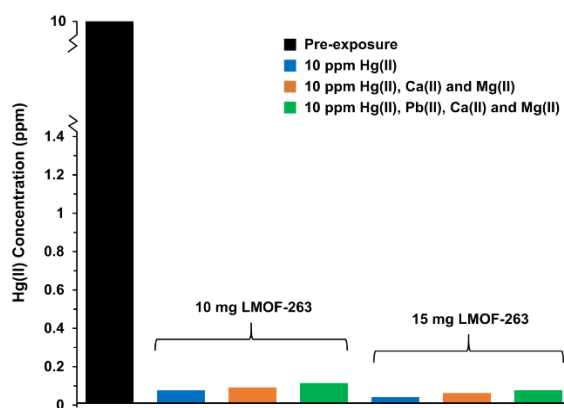


Figure 2.17. The remaining Hg^{2+} concentrations after exposure to various amounts of LMOF-263 in mixed metal solutions (initial concentrations: 10 ppm M^{2+} , as specified in the legend).

To emphasize its practical use as an on-site remediation material, LMOF-263 adsorption kinetics were analyzed. LMOF-263 (15 mg, 0.62 mM) was exposed to solutions of 10 ppm Hg^{2+} (35 mL) for specific time intervals. As shown in Figure 2.18, LMOF-263 displays fast second-order adsorption kinetics^{55, 59} with 99.1% of Hg^{2+} removed from solution within 30 min and 99.4% removed after 15 h. The minimal improvement after 30 min indicates the efficiency of Hg^{2+} adsorption. The experimental data were fitted with the pseudo-second-order kinetic model, shown in Equation 2.3:⁸⁰

$$\frac{t}{q_t} = \frac{1}{k_2 q_e^2} + \frac{t}{q_t}$$

Equation 2.3. Pseudo-second-order kinetic model, where k_2 ($\text{g mg}^{-1} \text{min}^{-1}$) is the adsorption rate constant, q_t (mg g^{-1}) is the amount of Hg^{2+} adsorbed at time t (min), and q_e (mg g^{-1}) is the amount of Hg^{2+} adsorbed at equilibrium.

The value of the adsorption rate constant k_2 was determined to be $0.295 \text{ g mg}^{-1} \text{min}^{-1}$, and a high correlation coefficient (>0.999) was obtained when the data was fit with the kinetic model (Figure 2.18b).

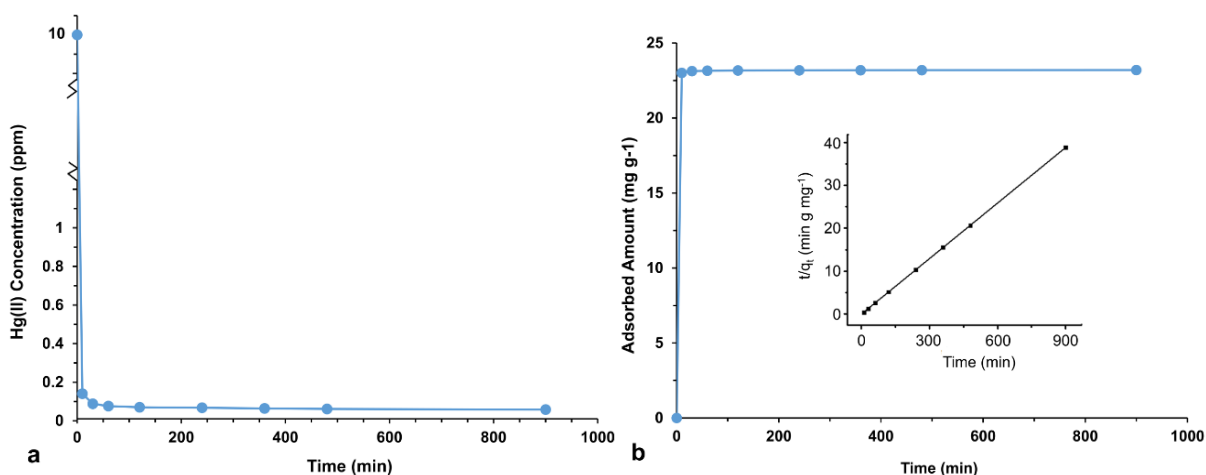


Figure 2.18. (a) Hg^{2+} concentrations after exposure to LMOF-263 for various time intervals. (b) The amount of adsorbed Hg^{2+} as a function of exposure time. The inset shows the pseudo-second-order kinetic plot for Hg^{2+} adsorption (initial Hg^{2+} concentration: 10 ppm).

One measure of a sorbent's affinity for some target metal ion is the distribution coefficient (K_d), defined in Equation 2.4:⁸¹

$$K_d = \left[\frac{C_i - C_f}{C_f} \right] \times \frac{V}{m}$$

Equation 2.4. Distribution coefficient relationship.

where C_i is the initial metal concentration, C_f is the final equilibrium metal ion concentration, V is the volume of treated solution (mL) and m is the mass of sorbent used (g). K_d values of 1.0×10^5

mL g⁻¹ are usually considered to have excellent performance.⁸² The K_d value for LMOF-263 on Hg²⁺ in this analysis was determined to be 6.45×10^5 mL g⁻¹. This is on the same order of magnitude as other high performance materials, including Zr-DMBD (9.99×10^5 mL g⁻¹),⁵⁷ sulfur-functionalized mesoporous carbon ($6.34\text{--}6.82 \times 10^5$ mL g⁻¹)⁸² and commercial resins ($10^4 \sim 5.10 \times 10^5$ mL g⁻¹).⁸³

As further confirmation of mercury uptake into LMOF-263, X-ray fluorescence spectroscopy (XRF) was employed to determine the amount of Hg²⁺ left in filtered LMOF samples after Hg²⁺ exposure. Approximately 15 mg of LMOF-263 was immersed in 35 mL water solutions of various concentrations of Hg²⁺ (10 through 30,000 ppm) for 36 h. After filtration and washing with copious amounts of water, XRF analysis was used to determine the relative weight ratios of Zn²⁺ and Hg²⁺ in the samples (Table 2.4). The structure of LMOF-263 was stable after exposure to Hg²⁺ for 36 h—Figure 2.19 exhibits the PXRD overlay of the filtered adsorbents after exposure to each Hg²⁺ concentration. The sharp peak observed around 4.5° 2θ in the simulated pattern is enhanced after Hg²⁺ exposure. This same phenomenon was seen after exposure to basic conditions (Figure 2.3). The presence of adsorbed species in MOF channels has been shown to increase low-angle diffraction peaks,⁸⁴ whether it be Hg²⁺ ions (from adsorption experiments) or by-products from the base-catalyzed hydrolysis of solvent guest molecules (base-exposure experiments). Figure 2.20 displays the molar ratios of Hg²⁺ to Zn²⁺ for samples treated at varied concentrations. After exposure to higher concentrations of Hg²⁺, the relative weight ratio of Hg²⁺ to Zn²⁺ approaches ~80% and ~20%, respectively, corresponding to approximately 1.3 Hg²⁺ ions per Zn²⁺ ion.

Table 2.4. Relative molar ratios of $\text{Hg}^{2+}:\text{Zn}^{2+}$ in LMOF-263 after exposure to various Hg^{2+} concentrations. Values represent averages over three trials.

Element	Hg^{2+} Concentration (ppm)					
	10	100	1000	10,000	20,000	30,000
Zn	1	1	1	1	1	1
Hg	0.25	0.47	0.76	0.88	1.19	1.30

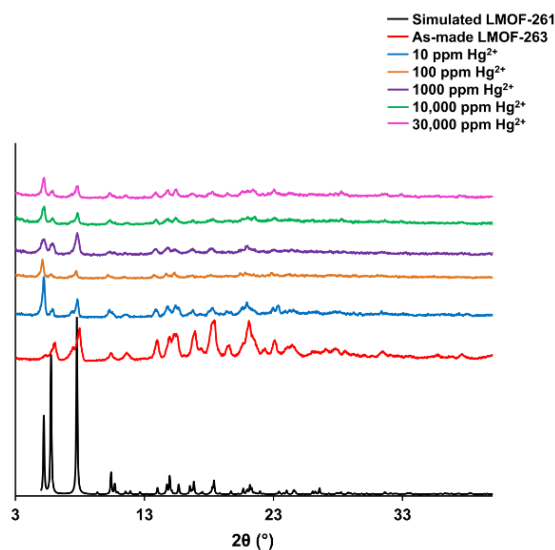


Figure 2.19. PXRD overlay of LMOF-263 samples, demonstrating structural effects with increased exposure to Hg^{2+} .

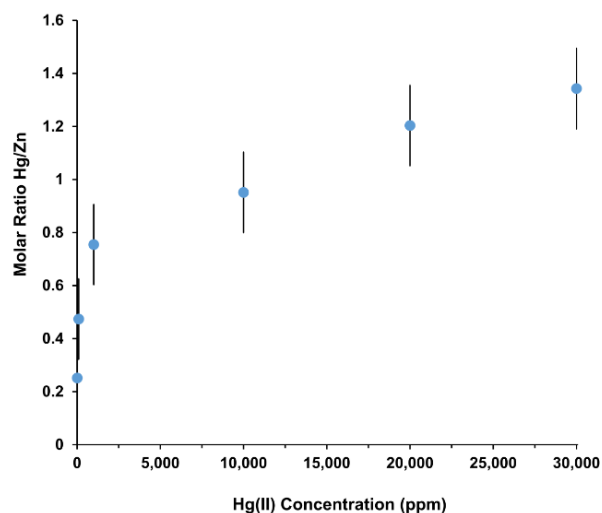


Figure 2.20. Molar ratio of Hg/Zn (blue dots) in LMOF-263 samples after exposure to 10, 100, 1,000, 10,000, 20,000 and 30,000 ppm Hg^{2+} solutions. These values represent averages over three trials. The error bars represent the average standard deviation of the molar ratio (± 0.152 Hg/Zn) over all concentrations.

For each unit cell of LMOF-263 there are equimolar amounts of Zn^{2+} and sulfone groups ($[\text{Zn}_2(\text{dbtdcO}_2)_2\text{tppe}]$, from SCXRD analysis on LMOF-261 described above), so there are also 1.3 Hg^{2+} per sulfone moiety. Previous work has demonstrated similar metal analyte interactions with sulfur (>1 metal ion per sulfur atom).⁸⁵ From the XRF data, LMOF-263 exhibits an estimated maximum uptake capacity of ~ 380 mg Hg^{2+}/g , which is at the similar scale compared with the best-performing MOFs for Hg^{2+} adsorption, although in all other cases no quantitative data were provided on their selectivity or sensitivity of fluorescent detection.^{57, 86,87-94} While unsaturated metal nodes in HKUST-1 or ligands within UiO-66 have been functionalized with thiol groups to enhance Hg^{2+} uptake (714 and 769 mg Hg^{2+}/g , respectively), these MOFs were reported to have no fluorescence, thus negligible detection potential.⁵⁵⁻⁵⁶ LMOF-263 displays both a low detection limit and a high uptake performance, establishing itself as an ideal, dual-functional material for water purification applications.

2.3.6 Hg^{2+} Interaction Mechanism

Fourier transform infrared (FTIR) spectroscopy was used to identify the different functional groups in LMOF-261 and LMOF-263. Data were collected on pristine samples of LMOF-263 and LMOF-261 (the parent structure). Sulfur-related vibrational modes were clearly identified for the LMOF-263 sample, and carbonyl modes observed for LMOF-261. In Figure 2.21, all the vibrational modes in the two pristine samples are shown in the $600\text{--}1800\text{ cm}^{-1}$ spectral range with the most important modes assigned and labeled as described below. The vibrational modes at 1311 (S=O str), 1170 (S=O str), 1133 ($-\text{SO}_2$ sym), 877 and 854 (C-S str) and 735 cm^{-1} (C-S-C) are associated with the presence of the sulfone moiety in LMOF-263 (Figure 2.21, red). LMOF-261 contains the carbonyl group in place of the sulfone moiety, characterized by vibrational

modes at 1720 (C=O str), 1090 (C-O str), 980 (C-O str) and 940 cm^{-1} (C-O str) (Figure 2.21, green).⁹⁵⁻⁹⁶

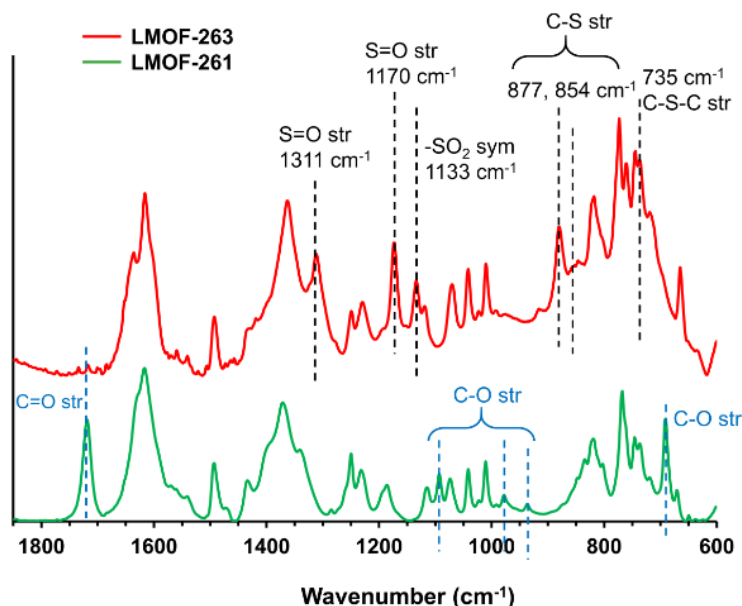


Figure 2.21. FTIR spectra for LMOF-261 and LMOF-263. Black labels are used to identify peaks related to the sulfone and other sulfur related moieties (LMOF-263), while blue labels show peaks concerning the carbonyl group (LMOF-261).

Details about the microscopic interaction of Hg^{2+} within LMOF-263 can be derived from X-ray photoelectron spectroscopy (XPS) measurements through analyses of the core level shifts. XPS was employed to further investigate the interaction of Hg^{2+} or Mg^{2+} with LMOF-263. Information regarding changes in local electronic structure of S, C and O as a function of Hg^{2+} or Mg^{2+} concentration can be inferred by monitoring the sulfur binding energy in LMOF-263. Figures 2.22-2.27 display the XPS spectra for pristine and Hg^{2+} -loaded LMOF-263 samples for various Hg^{2+} concentrations. The binding energies of carbon (1s), oxygen (1s), sulfur ($2p^{3/2}$, $2p^{1/2}$) and mercury ($4f^{7/2}$, $4f^{5/2}$) are noted in the spectra. Figure 2.28 exhibits the XPS spectra of LMOF-263 exposed to 20,000 ppm Mg^{2+} .

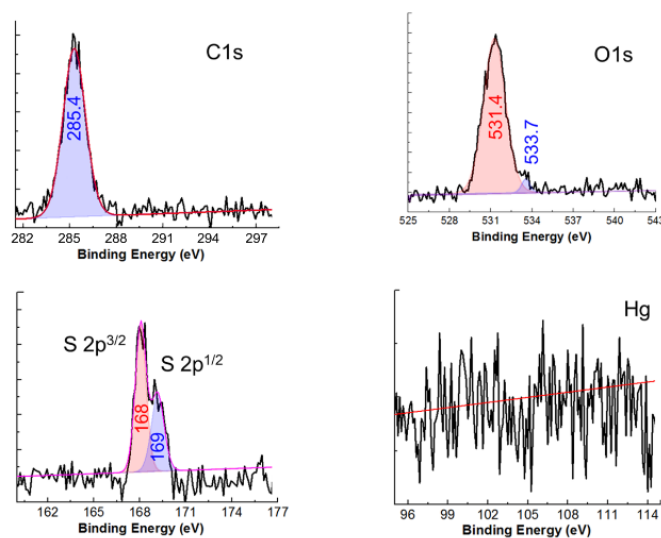


Figure 2.22. XPS spectra for as-made LMOF-263.

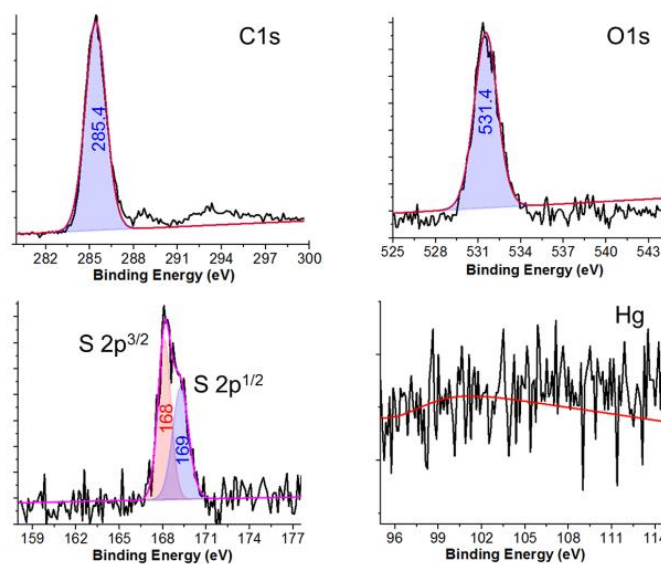


Figure 2.23. XPS spectra of LMOF-263 exposed to water (no Hg) as reference. No trace Hg^{2+} is detected after the water treatment throughout the analysis.

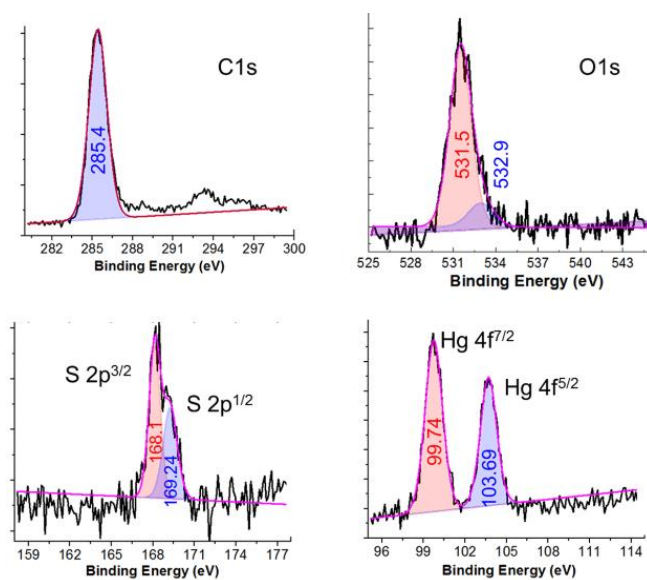


Figure 2.24. XPS spectra of LMOF-263 exposed to 100 ppm Hg^{2+} .

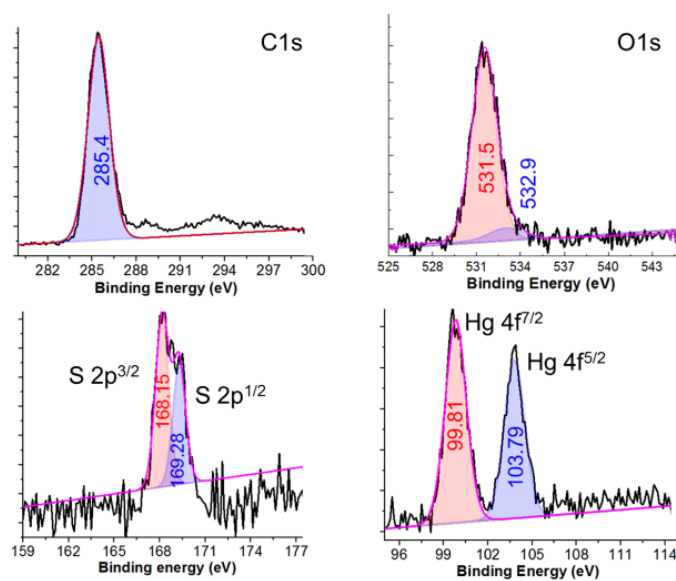


Figure 2.25. XPS spectra of LMOF-263 exposed to 1,000 ppm Hg^{2+} .

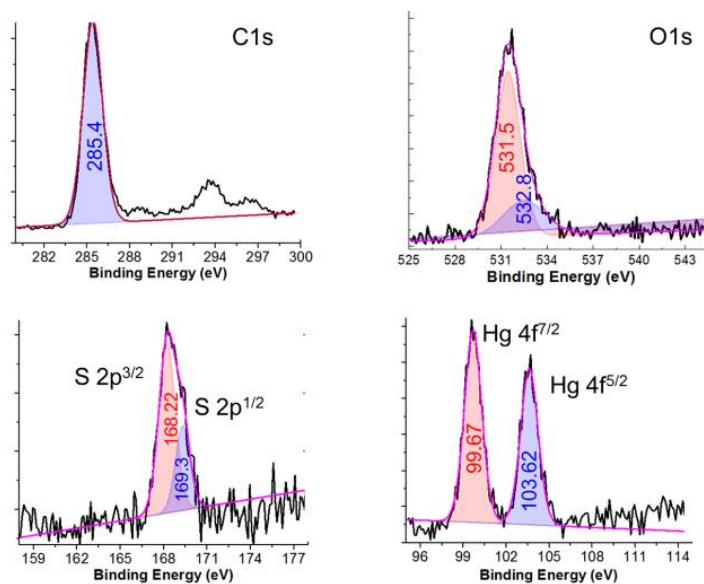


Figure 2.26. XPS spectra of LMOF-263 exposed to 10,000 ppm Hg^{2+} .

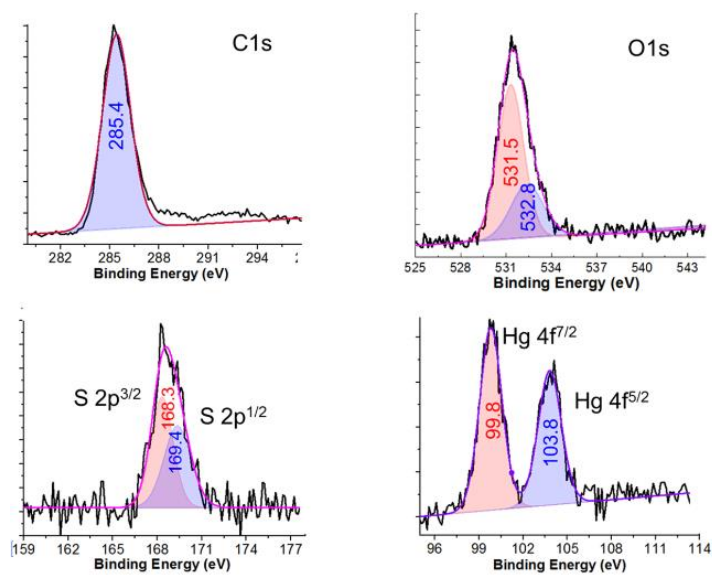


Figure 2.27. XPS spectra of LMOF-263 exposed to 30,000 ppm Hg^{2+} .

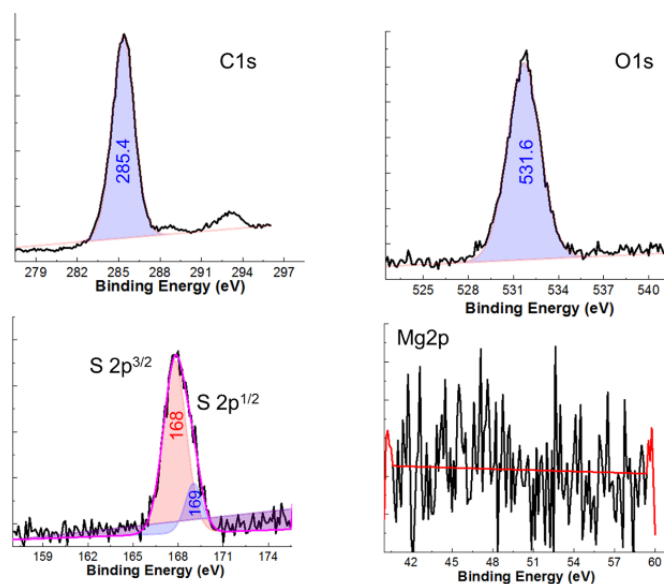


Figure 2.28. XPS spectra of LMOF-263 exposed to 20,000 ppm Mg^{2+} .

The sulfur (S orbitals $2p^{3/2}$, $2p^{1/2}$) binding energies increase with increased exposure to Hg^{2+} . In Figures 2.22 and 2.23, the carbon, oxygen and sulfur binding energies are the same in both the as-made LMOF-263 and the water-exposed LMOF-263. This confirms that any perturbation in the observed binding energies must be from interactions with Hg^{2+} , as shown in Figures 2.24-2.27. A secondary oxygen binding energy (532.9/532.8 eV) is measured in the Hg^{2+} -exposed samples that was not observed in the as-made, water-exposed or Mg^{2+} -exposed samples. This lends evidence that the oxygen atom within the sulfone group is also affected by the presence of Hg^{2+} . Additionally, since there is no observed shift of the C core level, the interaction is assumed to remain on the sulfone functionality. In contrast, upon LMOF-263 exposure to 20,000 ppm of Mg^{2+} (Figure 2.28), there are no changes in the sulfur binding energy, supporting the observation that LMOF-263 selectively interacts with heavy metals. Table 2.5 summarizes the data from Figures 2.22-2.28. The increase in sulfur binding energy as Hg^{2+} concentration increases is most clearly seen and monitored by overlaying the S core levels in Figure 2.29.

Table 2.5. Summary of XPS data for LMOF-263 exposed to various Hg^{2+} and Mg^{2+} concentrations.

	Binding Energy (eV)			Hg/Mg
	C	O	S	
As-made	285.4	531.4	168/169	0
H ₂ O exposed	285.4	531.4	168/169	0
100 ppm Hg^{2+}	285.4	531.5/532.9	168.1/169.24	99.74/103.69
1,000 ppm Hg^{2+}	285.4	531.5/532.9	168.15/169.28	99.7/103.75
10,000 ppm Hg^{2+}	285.4	531.5/532.8	168.22/169.3	99.7/103.62
30,000 ppm Hg^{2+}	285.4	531.5/532.8	168.3/169.4	99.8/103.8
20,000 ppm Mg^{2+}	285.4	531.5	168/169	0

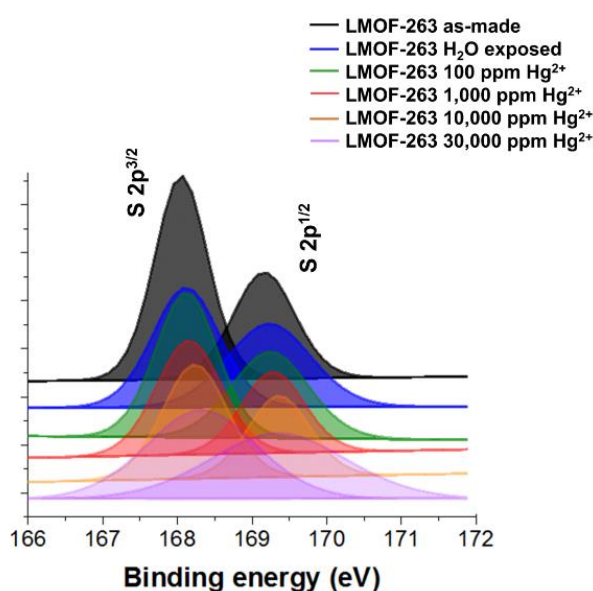
**Figure 2.29.** Overlaid XPS spectra of LMOF-263 exposed to incremental Hg^{2+} concentrations. The sulfur binding energy increases (curves shift to the right) when exposed to higher Hg^{2+} concentrations.

Table 2.6 exhibits the change in the oxygen binding energies as Hg^{2+} concentration increases. The gradual change indicates that Hg^{2+} interacts with both sulfur and oxygen atoms in the sulfone moiety. Upon Mg^{2+} exposure, the secondary oxygen binding energy peak is nonexistent, emphasizing minimal interactions between the sulfone group and the light metal. These findings are similar to previous studies of Hg^{2+} incorporation in materials (i.e. typical Hg^{2+} interactions with S),^{70-71, 97-98} The Hg^{2+} ions have a stronger affinity to sulfur than to O_2 , increasing

the sulfur binding energy in the mercury-exposed samples relative to the as-made LMOF-263. Similar binding energies for Hg-S interactions have been reported in the literature.⁹⁹ In conclusion, XPS confirms the selective interaction of Hg^{2+} with sulfone groups within LMOF-263, supporting conclusions from fluorescence titrations and ICP-OES measurements.

Table 2.6. The percent atomic concentration at each oxygen core level over multiple Hg^{2+} and Mg^{2+} exposure conditions.

	O ₂ Binding Energy (eV)	
	~531.5	~534
	Percent Atomic Concentration (%)	
0 ppm Hg^{2+}	97	3
100 ppm Hg^{2+}	87	13
1,000 ppm Hg^{2+}	91	9
10,000 ppm Hg^{2+}	72.2	27.7
30,000 ppm Hg^{2+}	68.3	31.7
20,000 ppm Mg^{2+}	100	0

Although oxygen and sulfur have similar binding energies with mercury (100.7 and 101 eV, respectively), sulfur exhibits other bonding properties that give it a higher affinity for heavy metals, such as the availability of vacant *d-orbitals* as opposed to oxygen, lower ionization potential and electronegativity, and greater polarizability compared to oxygen, which has led to the classification of sulfur as a *soft* base and oxygen as a *hard* base. *Soft* bases have a higher affinity to *soft* acids like mercury and silver, and less affinity to *hard* acids like calcium and magnesium, based on the HSAB Pearson acid-base concept.¹⁰⁰ Figure 2.30 illustrates the potential configuration and interaction of Hg^{2+} with the sulfone group linkers based on earlier work.¹⁰¹

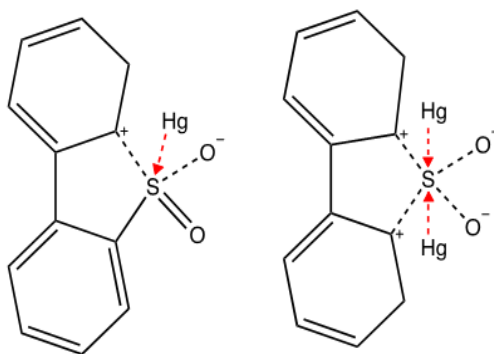


Figure 2.30. Interaction mechanism of Hg^{2+} with the sulfone functional group.

2.4 Conclusions

We have designed, synthesized and structurally characterized a new series of isorecticular LMOFs containing tpe chromophore ligand and a functionalized co-ligand. In addition, we have performed a systematic study to investigate, compare and understand their photoluminescent properties and to assess their potential as chemical sensors and adsorbents for heavy metals. LMOF-263, specifically, is a porous, water-stable, blue-emitting MOF with a high IQY (89.2%) and a BET surface area of $1004 \text{ m}^2/\text{g}$. LMOF-263 acts as a highly sensitive and selective sensor, capable of detecting heavy metal ions in water at very low concentrations (e.g. 3.3 ppb for Hg^{2+} and 19.7 ppb for Pb^{2+}) and has a high Hg^{2+} uptake capacity of $\sim 380 \text{ mg/g}$. The detection ratio for Hg^{2+} compared to light metals Mg^{2+} and Ca^{2+} are 209.5 and 167.4, respectively, illustrating the excellent selectivity of LMOF-263 for heavy metal ions. The achieved K_{SV} values are among the highest in their class for Hg^{2+} ($459,446 \text{ M}^{-1}$) and Pb^{2+} ($55,017 \text{ M}^{-1}$). No other MOFs reported to date have had such high performances in both the detection and adsorption of toxic heavy metals. The Hg^{2+} adsorption process follows a fast, second-order kinetics model (rate constant: $0.295 \text{ g mg}^{-1} \text{ min}^{-1}$), removing 99.1% of the total contaminant amount within 30 min. LMOF-263 selectively adsorbed Hg^{2+} when exposed to a mixture of heavy and light metals.

These results suggest that LMOF-263 is well suitable for the simultaneous optical detection (through luminescence quenching) and selective removal of heavy metals (e.g. Hg^{2+} , Pb^{2+}) from aqueous solution. XPS data provide direct evidence for the interaction of Hg^{2+} with the sulfone moiety, underscoring the role of sulfur in these LMOF materials. Materials that can detect low concentrations and selectively adsorb heavy metals can greatly benefit environmental remediation efforts. Simple and cost-effective optical detection methods using these materials would prove to be valuable for populations across the globe.

CHAPTER 3: Ligand-based Emission towards the Detection of Carbon Tetrachloride

3.1 Introduction

Extensive research has been dedicated to the design and synthesis of luminescent metal-organic frameworks (LMOFs) throughout the last decade. LMOFs have received this attention due to their endless potential in a variety of optical applications.^{18, 44, 102-104} Recently, LMOFs as chemical sensors have been a vital focus due to their porosity, surface tunability and moderate synthetic conditions.^{41-43, 45-47} Multi-linker MOFs allow for fine-tuning of the pore environment,¹⁰⁵ which enables specific analytes to enter the MOF pores and interact with the framework, aiding in effective detection. It has been shown that the combination of Zn(II) ions, a tricarboxylate co-ligand, and a chromophoric ligand generates an LMOF with targeted emission energy and enhanced fluorescence IQY compared to the molecular chromophore.¹⁷ Based on our previous work, MOFs built from Group 12 metals generally give rise to ligand-based or ligand-to-ligand charge transfer processes.^{49, 64, 106-111} Similarly, a Zn-based material was synthesized with a functionalized co-linker and a chromophoric ligand that was used for the simultaneous sensing and removal of toxic heavy metals from water,²⁷ yet the same chromophoric linker was paired with a

comparably sized co-linker with different functionalization to detect agricultural toxins.⁶³ Slight differences in linker shape and varied functional moieties, coupled with a chromophoric species, can result in a vast library of potential sensor materials with distinctive applications. The presence of both functionalized and fluorescent organic linkers helps to promote a specific emission response from the LMOF-analyte interaction.

The LMOF-analyte interaction prompts a luminescence quenching or enhancement response, depending on the electronic properties of the target analyte and the primary interaction site on the LMOF. Luminescence quenching (“turn-off”) detection has been more common for LMOF sensors, however, the presence of electron-rich aromatic species in the host framework has been shown to promote luminescence enhancement (“turn-on”) detection.^{18, 110, 112} Luminescence enhancement sensing simplifies optical detection methods by making the system easier to observe against a dark background, with the naked eye.

The industrial age has evoked innumerable organic contaminants that plague our environment. Carbon tetrachloride (CTC) is a relatively stable chemical and persistent under normal environmental conditions. Thus, there has been a gradual accumulation of CTC in the environment as a repercussion to industrial activities.¹¹³ The use of CTC as a fumigant pesticide was banned in 1986, however the haloalkane has been used in the production of chlorofluorocarbons and cleaning fluids more recently. Although these substances are getting phased out of production as well, the stability of CTC allows it to enter the ecosystem if these products aren’t handled appropriately. A large amount of the CTC released into the environment enters the atmosphere due to its high vapor pressure, and a fair portion interacts with soil, either adsorbing to organic matter or leaching into groundwater.¹¹⁴ In the atmosphere, CTC reacts with ozone or oxygen to form chlorine monoxide radicals that vastly degrade the ozone layer, while

human exposure from groundwater results in liver or kidney malfunction.^{113, 115} Similar volatile organic solvents, namely chloroform (CLF) and dichloromethane (DCM), also pose some danger to the environment and human health. However, these solvents are more commonly used in industry due to their lower toxicity levels compared to CTC.¹¹⁶

Previously, CTC has been selectively detected using “cataluminescent” probes, however this strategy relies on temperature-sensitive catalytic oxidation and reduction reactions, limiting its simplicity.¹¹⁷⁻¹¹⁸ Additionally, nanocomposite thin films have been utilized to selectively detect carbon tetrachloride from other VOCs,¹¹⁹ but this fabrication method is expensive and utilizes advanced equipment that would not be ideal for practical settings. Dual-ligand LMOFs provide a unique surface where analytes can interact with target functional moieties and luminescent species in extreme proximity to achieve required sensitivity and selectivity. The strong tunability of LMOFs insures the inclusion of these vital properties.^{18, 62} We have recently designed and synthesized a LMOF with an immobilized chromophore and an anthracene-based co-linker that promotes effective van der Waals and electronic interactions to selectively detect CTC over similarly structured CLF and DCM.

3.2 Experimental Details

3.2.1 Synthesis of LMOF-271

The tetradentate linker 1,1,2,2-tetrakis(4-(pyridine-4-yl)phenyl)ethane (tppe) was synthesized following previous procedures, outlined in Section 2.2.1. In 20 mL glass vials, mixtures of $\text{Zn}(\text{NO}_3)_2 \cdot 6\text{H}_2\text{O}$ (0.015 g, 0.05 mmol), 9,10-anthracenedicarboxylic acid (H_2adc ; 0.013 g, 0.05 mmol) and tppe (0.007 g, 0.01 mmol) dissolved in DMF:iPrOH:DMSO (4:1:1) were prepared and heated to 150 °C for 15 h. The reactions were cooled slowly to room temperature, at which point yellow block crystals (Figure 3.1) were collected via vacuum filtration and washed thoroughly with DMF.

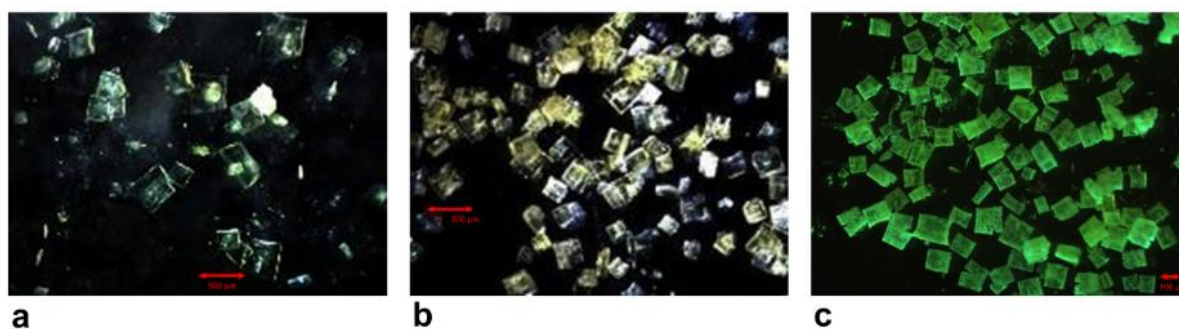


Figure 3.1. (a) Pristine LMOF-271 crystals in the mother liquor, (b) filtered and washed with DMF and (c) under 365 nm excitation.

Crystals of LMOF-271 [$\text{Zn}_4(\text{adc})_4(\text{tppe})$] maintain high quality while still immersed in the mother liquor (Figure 3.1a). After filtration and washing with DMF, the block crystals lower in quality, as seen in Figure 3.1b. For SCXRD, samples of LMOF-271 were kept in the mother liquor to ensure the crystal quality was maintained. Figure 3.1c portrays crystals of LMOF-271 under 365 nm excitation, emphasizing uniform luminescence in the solid state.

3.2.2 Structural Analysis of LMOF-271

Single-crystal X-ray diffraction (SCXRD) data for LMOF-271 were collected on a Bruker PHOTON100 CMOS diffractometer using the synchrotron source ($\lambda = 0.7749 \text{ \AA}$) at the Advanced Light Source 11.3.1 Chemical Crystallography beamline (Table 3.1).

Table 3.1. Single crystal data of LMOF-271

Compound	LMOF-271
Formula	$\text{C}_{55}\text{H}_{32}\text{N}_2\text{O}_8\text{Zn}_2$
M	979.56
Crystal system	Orthorhombic
Space group	Imma
$a/\text{\AA}$	21.6011(15)
$b/\text{\AA}$	21.8271(15)
$c/\text{\AA}$	43.822(3)
$\alpha/^\circ$	90
$\beta/^\circ$	90
$\gamma/^\circ$	90
$V/\text{\AA}^3$	20662(2)
Z	8
Temperature/K	270(2)
λ (radiation wavelength)/ \AA	0.7749
D (g/cm^3)	0.630
Reflections collected	61380
$R1^a$ [$I > 2\sigma(I)$]	0.0730
$wR2^b$ [$I > 2\sigma(I)$]	0.1419
Goodness-of-fit	1.028
CCDC No.	1526908

$$^a R1 = \sum |F_o - F_c| / \sum |F_o|$$

$$^b wR2 = \sum [w(F_o^2 - F_c^2)^2] / \sum w(F_o^2)^2]^{1/2}$$

All non-hydrogen atoms were refined anisotropically; hydrogen atoms were placed geometrically, constrained and refined with a riding model. The unresolvable electron density from the void space in the structure was removed by SQUEEZE. The powder X-ray diffraction (PXRD) patterns were collected using a Rigaku Ultima-IV diffractometer using monochromatic Cu K_α

radiation ($\lambda = 1.5406 \text{ \AA}$). Data were collected between 3 and $45^\circ 2\theta$ with step size 0.02° and scanning rate $2.0^\circ/\text{min}$.

3.2.3 Porosity Investigation

Gas sorption isotherms of LMOF-271 were collected on an Autosorb-1 MP volumetric gas sorption analyzer (Quantachrome Instruments) utilizing ultra-high-purity N_2 (99.999%). Liquid nitrogen was used as the coolant to reach cryogenic temperatures (77 K). As-made LMOF-271 (75 mg) was immersed in 15 mL of tetrahydrofuran (THF) in a glass vial for 5 h. At this point, the supernatant was decanted from LMOF-271, and fresh THF was added. This process was repeated five times. This amount of THF-exchanged sample was activated at 343 K for 8 h under vacuum. The N_2 isotherm was measured in a pressure range between 10^{-7} and 1 atm at 77 K (Figure 3.2). The Brunauer-Emmett-Teller (BET) surface area of LMOF-271 was estimated to be $660 \text{ m}^2/\text{g}$ with a pore volume of $0.271 \text{ cm}^3/\text{g}$ using Autosorb V1.50 software. The nonuniform pore size distribution indicates that LMOF-271 exhibits multiple types of pores, with different dimensions, depending on the orientation of the crystal. This is supported by the structure plots in Figure 3.6.

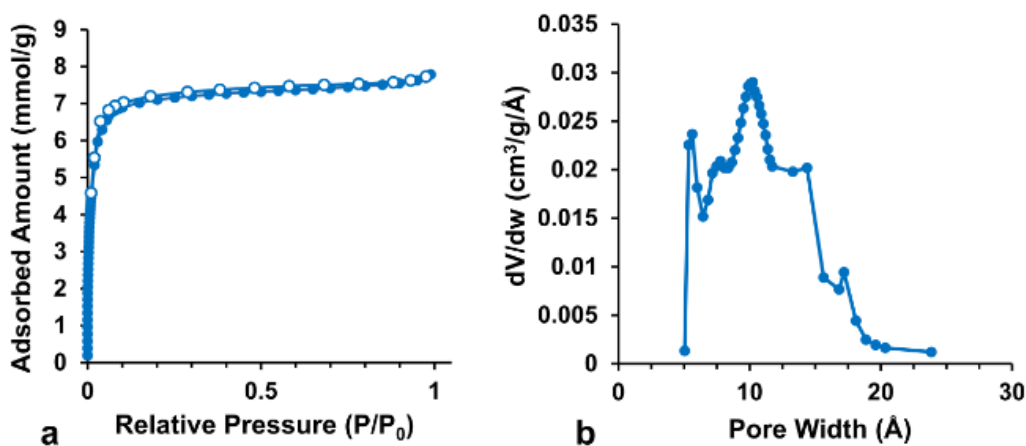


Figure 3.2. (a) N_2 adsorption (solid) and desorption (void) isotherms for LMOF-271. (c) The H-K micropore size distribution analysis. The nonuniform pore size indicates various pore dimensions along LMOF-271.

3.2.4 Thermogravimetric Analysis

Thermogravimetric analysis (TGA) was completed via a TA Instruments Q5000 under constant N₂ flow (20 mL/min). Approximately 5 mg of pristine LMOF-271 was placed into a platinum pan, which was then heated from 30-600 °C at a rate of 10 °C/min. The weight loss from LMOF-271 was monitored over the temperature increase (Figure 3.3).

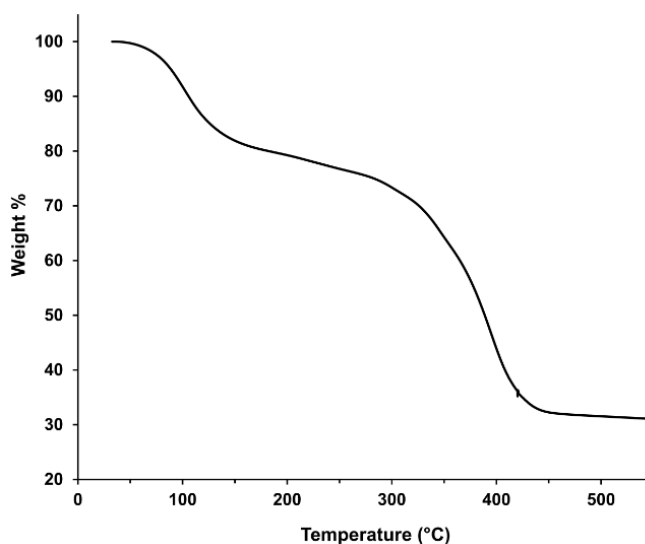


Figure 3.3. Thermogravimetric analysis (TGA) of pristine LMOF-271.

3.2.5 Optical Characterization of LMOF-271

In the interest of determining absorbance properties of LMOF-271, UV-visible diffuse reflectance spectra were obtained for LMOF-271 and the chromophoric ligand ttppe at room temperature (Figure 3.4). Measurements were made using a Shimadzu UV-3600 spectrophotometer. The diffuse reflectance data was converted to the Kubelka-Munk function, according to Equation 2.1.

As portrayed in Figure 3.4, the estimated bandgap of LMOF-271 (~2.5 eV) is redshifted from that of the ligand ttppe (~2.3 eV). Figure 3.5 depicts the optical excitation and emission spectra for pristine and activated samples of LMOF-271. These spectra were measured using a

Varian Cary Eclipse spectrophotometer under 365 nm excitation. The emission energy was redshifted upon activation, from 475 to 516 nm. There are negligible changes in the optical excitation spectrum between the activated and pristine samples. Internal quantum yield (IQY) values were calculated using a Hamamatsu C9220-03 spectrophotometer with integrating sphere. IQY values for pristine and activated LMOF-271 are 18.6% and 16.2%, respectively.

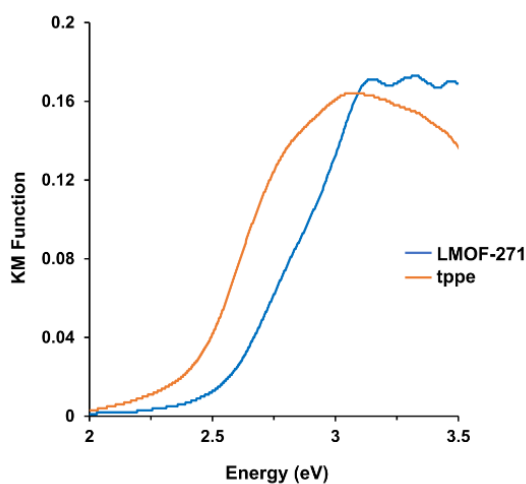


Figure 3.4. Optical absorption spectra (converted to KM function) of LMOF-271 (blue) and tppe (orange).

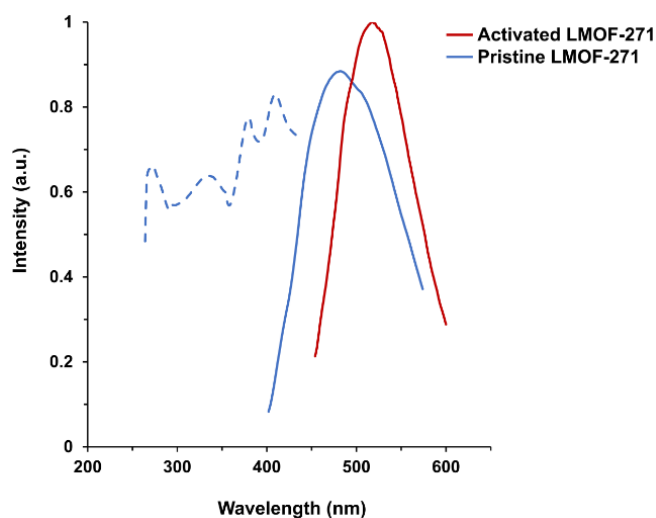


Figure 3.5. Optical emission and excitation spectra for pristine (blue) and activated (red) LMOF-271. The displayed emission spectra were monitored under $\lambda_{\text{ex}} = 365$ nm, while the excitation spectrum was monitored at 475 nm. The LMOF-271 excitation spectrum does not change after activation.

3.2.6 Fluorescence Titrations

Stock solutions (20 ppm) of carbon tetrachloride (CTC), dichloromethane (DCM) and chloroform (CLF) were prepared by adding the appropriate amount of each haloalkane to THF. An outgassed sample of LMOF-271 was placed in THF (0.25 g/L) and gently sonicated, effectively suspending the solid. Photoluminescence (PL) titrations were conducted by adding aliquots of the haloalkane/THF mixtures (CTC, CLF and DCM) to the suspension of LMOF-271. The system was kept under constant stirring to ensure uniform distribution of the analytes. Emission spectra were measured 8 min after adding the most recent aliquot of the stock solution. Each emission measurement was repeated three times and the average value was used.

3.3 Results and Discussion

3.3.1 Crystal Structure Analysis

LMOF-271, with formula $[\text{Zn}_4(\text{adc})_4(\text{tppe})]\cdot\text{S}$ (S = solvent guest molecules), crystallizes in a body-centered orthorhombic system with space group *Imma*. Each Zn^{2+} bonds to four oxygen atoms, each from individual adc linkers, and one nitrogen atom from tppe (Figure 3.6a).

As seen in Figure 3.6b, two adjacent five-coordinate Zn atoms are connected by bridging carboxylate groups from adc linkers to make a paddle-wheel type SBU—these adc linkers extend out into the ab-plane, while tppe affixes the 2D sheets together to expand the framework in three dimensions. The vinylic phenyl group within tppe exhibits 2-fold disorder, which is common among MOF crystal structures.

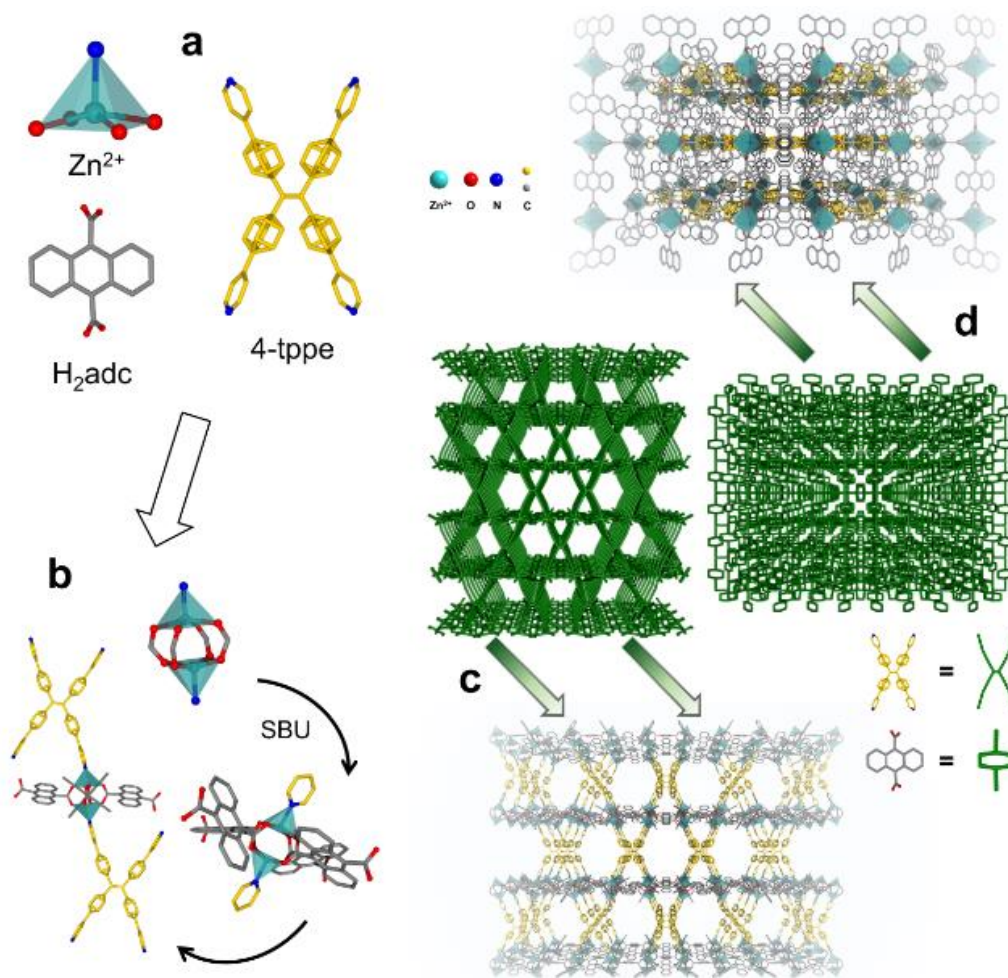


Figure 3.6. (a) Each Zn²⁺ is five-coordinate, having a Zn-N bond with one chromophoric tppe and four Zn-O bonds with four adc linkers. (b) The Zn-based SBU is a paddle-wheel-type structure with adc linkers extending into the *ab*-plane, and tppe ligands expanding the framework along the *c*-axis. (c) LMOF-271 viewed along the *b*-axis, showing edge-sharing hexagonal and triangular 1D channels. This further depicts the 2D sheets of Zn SBUs and adc linkers that are connected through tppe ligands. (d) The same net portrayed down the *c*-axis, showing tetragonal 1D channels that are heavily occupied with anthracene groups from the adc linkers. Anthracene groups have different orientations throughout the 1D channel.

Figure 3.6c displays LMOF-271 viewed along the *b*-axis. The edge-sharing hexagonal 1D channels have an aperture of ~ 10 Å and proliferate down the *b*-axis—both tppe ligands and anthracene groups from the adc linkers line the walls of the channel, showcasing the benefits for a dual-linker system and the versatility of the potential chemistry within the pores of the framework. The simplified network is displayed in green, emphasizing the fact that this system has no

interpenetration, an interesting phenomenon as MOFs with large pores, higher synthetic temperatures and no sterically obstructed ligands are known to form interpenetrated frameworks.¹²⁰ LMOF-271 also exhibits tetragonal 1D channels extending down the c-axis (Figure 3.6d), however the pore window is minimized due to the dense array of anthracene groups lining the channel. Although the aperture is diminished, the anthracene functionalities have random orientations along the c-axis, providing an interesting landscape for analyte interactions within the LMOF channels. The structure is represented by a 2-nodal, (4,6)-c net (sqc124 type) with (4-c)(6-c)2 stoichiometry. The simulated pattern from SCXRD on LMOF-271 matches the corresponding PXRD patterns of pristine LMOF-271 and samples exposed to various experimental conditions (Figure 3.7), indicating LMOF-271 stability throughout the study.

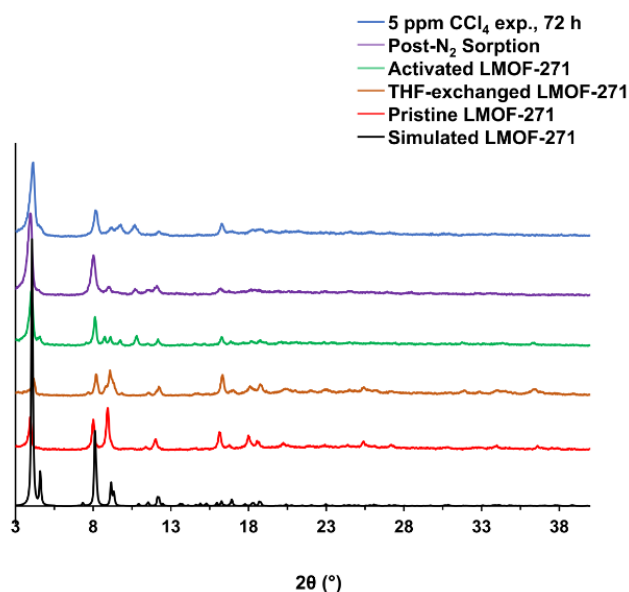


Figure 3.7. PXRD pattern of simulated LMOF-271 overlaid with those of LMOF-271 exposed to various experimental conditions. The small peak at $\sim 4^\circ$ 2θ that was determined through the simulated pattern only arises after LMOF-271 activation (green pattern).

3.3.2 Optical Detection

CTC has been identified as a carcinogenic solvent, often the byproduct of industrial processes and has been recognized as a harmful contaminant in the atmosphere and soil. Although CLF and DCM can be harmful solvents as well, they have lower toxicity compared to CTC.^{116, 121} A sensitive and selective probe for CTC is valuable to ensure that the concentrations do not approach harmful levels (EPA limit in drinking water—5 ppb)¹¹³ and affect ecosystems/human health.

Detection analyses of various solvents (CTC, CLF and DCM) were performed by measuring the change in the emission intensity of an LMOF-271 suspension in THF. Figure 3.8a displays the change in the emission (solid line) intensity as pristine LMOF-271 is immersed in THF (0.25 g/L). Although the emission wavelength is the same when LMOF-271 is suspended, the intensity is increased ($\lambda_{\text{ex}} = 365 \text{ nm}$). This emission wavelength and intensity are maintained in THF after submersion for 72 h, so any subsequent changes in the PL profile are due to analyte influences. The excitation spectrum (dotted line) for LMOF-271 does not change after addition to THF. Additionally, LMOF-271 is stable in THF for at least 72 h, as identified through activation procedures, and forms a uniform suspension—thus, THF provides an appropriate environment for sensing analyses to occur.

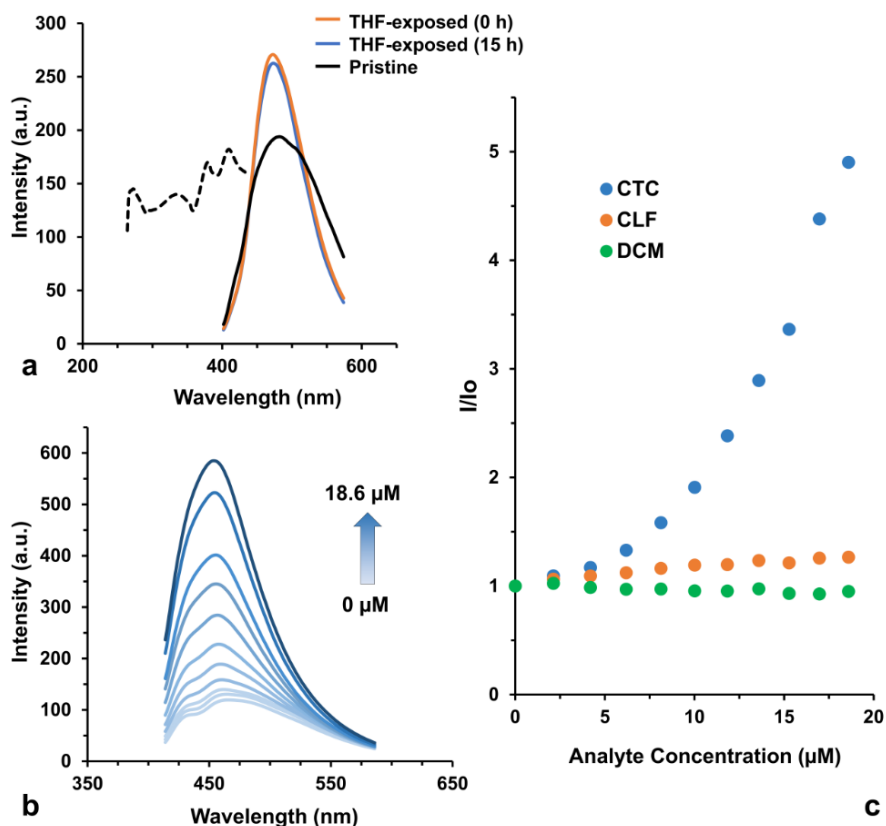


Figure 3.8. (a) The optical emission spectra of pristine (black) and THF-suspended LMOF-271 (orange—0 h, blue—15 h, $\lambda_{\text{ex}} = 365$ nm). (b) The emission enhancement of LMOF-271 as the sensor is exposed to incremental amounts of CTC ($\lambda_{\text{ex}} = 365$ nm). Emission spectra were recorded 8 min after the increase in CTC concentration. (c) Stern-Volmer curves for various chloromethane solvents. LMOF-271 displays a highly selective signal response to CTC (blue) over CLF (orange) and DCM (green).

After the addition of analyte, the LMOF-271 emission intensity increases depending on the type of solvent and its concentration. This emission intensity enhances by a factor of 4.9 when exposed to 18.6 μM (2.86 ppm) of CTC (Figure 3.8b), while the intensity increases by only a factor of 1.27 when exposed to 18.6 μM of CLF. Upon exposure to DCM, the LMOF-271 emission intensity raises negligibly (1.025x). The PL enhancement was quantified using the Stern-Volmer relationship (Equation 2.2).

The Stern-Volmer coefficient (K_{SV}) quantitatively measures the proficiency of LMOF-271 as a sensor for CTC. According to Figure 3.9, at low analyte concentrations there is a direct relationship between I/I_0 and CTC concentration, while the slope of the line is the K_{SV} . The CTC K_{SV} was determined to be $48,903 \text{ M}^{-1}$, which is the highest reported value among known CTC detection materials.¹²²⁻¹²³

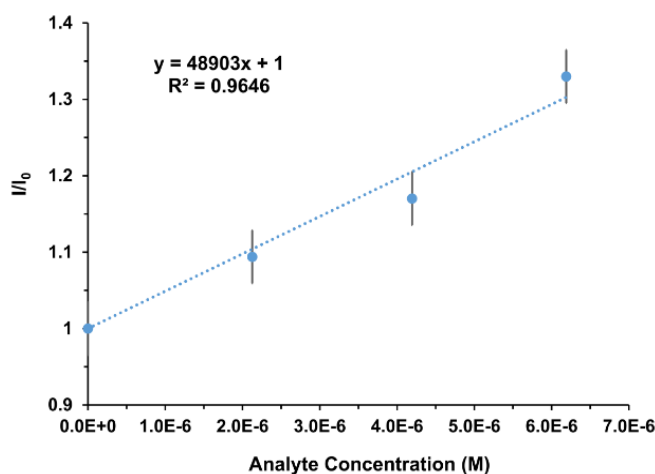


Figure 3.9. Stern-Volmer curve for LMOF-271 when exposed to CTC. Error bars indicate the average standard deviation of I/I_0 values between multiple trials of PL titrations. The inset equation describes the linear relationship between I/I_0 and CTC concentration at low values. The slope represents the fluorescence enhancement efficiency, K_{SV} .

This study represents the first example of using an LMOF for CTC detection. For CLF, the K_{SV} value is less than half of that for CTC ($19,971 \text{ M}^{-1}$), highlighting the selectivity of LMOF-271 for CTC. The limit of detection (LOD) is defined as the concentration of analyte at which the decrease in intensity is greater than the average standard deviation in repeated measurements of the same sample. The average emission intensity standard deviation for CTC exposures was 2.374 a.u. Using the S-V curve in Figure 3.9, the limit of detection for CTC was calculated to be 22 ppb. To confirm this LOD, Figure 3.10 portrays a low-concentration PL titration of LMOF-271 with CTC. The addition of 25 ppb was clearly detected. This LOD is on the same order of magnitude with the maximum contaminant level (MCL) levied by the EPA (5 ppb).¹¹³

Recyclability is vital to the practical application of a detection material, especially for environmental remediation efforts. Once a suspension of LMOF-271 was exposed to 2.86 ppm (18.6 μM) of CTC, the solid was separated from the supernatant through centrifugation, then washed copiously with DMF and THF. The solid was then dried under vacuum at room temperature for 2 h. After submerging in THF again, the fluorescence signal returned to that of the original suspension—this was considered one cycle (Figure 3.11). As CTC is volatile, whatever is not washed after exposure to THF and DMF should evaporate at room temperature under vacuum, leaving LMOF-271 available for further sensing analyses.

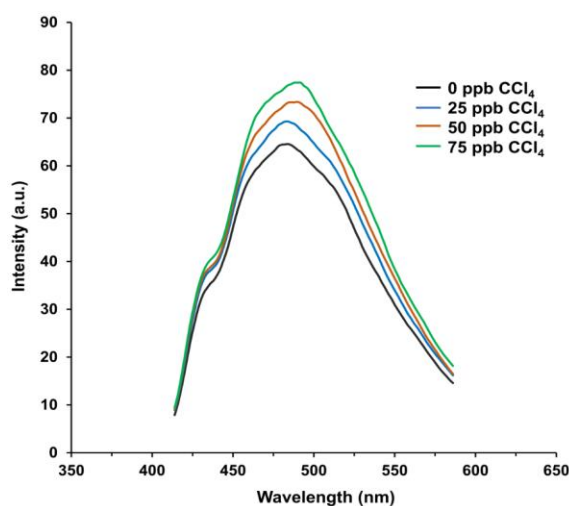


Figure 3.10. The overlay of emission spectra from the low concentration fluorescence titration of LMOF-271 with aliquots of CTC. Detection of 25 ppb (blue) is clearly detected.

Figure 3.11 portrays changes in the fluorescence signal from LMOF-271 as the material is exposed to CTC (solid dot) and after it undergoes the washing/evaporation (void dot) procedures reported above. Recyclability tests were done on LMOF-271 for two full cycles of CTC exposure. During the third cycle, upon CTC exposure, the color of solid LMOF-271 drastically changed

(yellow to dark orange), possibly indicating the onset of structure degradation. Additionally, the PL signal from this sample in the 3rd cycle is also reduced.

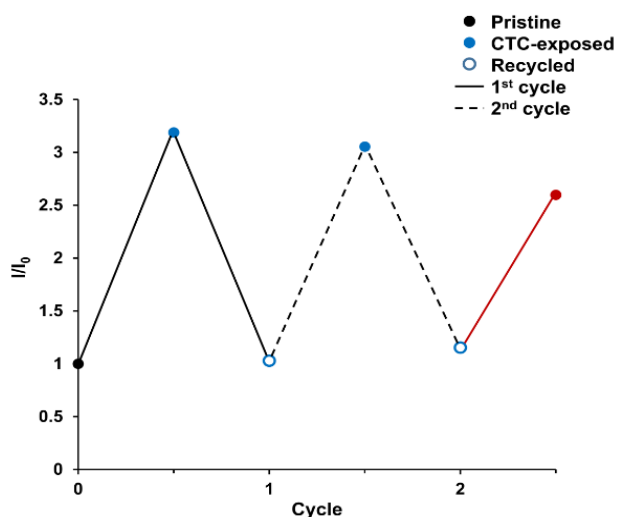


Figure 3.11. PL intensity ratios of LMOF-271 at each stage of the CTC exposure and washing portions of the recycling analysis. The red dot indicates that the fluorescence signal was not enhanced to the same level as the previous two cycles. At this stage there was drastic color change in the solid LMOF-271, indicating degradation of the structure.

The higher selectivity for CTC over CLF and DCM is attributed to the nonpolar environment in the LMOF-271 channels. Previous studies have demonstrated the effectiveness of making use of MOFs with functionalized, nonpolar channels to detect volatile organic compounds (VOCs).¹²⁴⁻¹²⁵ The aromatic anthracene-based colinker and nonpolar CTC can interact through van der Waals forces, while the more polar CLF and DCM do not combine effectively with the framework.¹²⁶ Emission quenching can be a result of electronic influences between immobilized polyaromatic molecules, so the presence of guest species that interfere with π - π interactions could promote an enhanced emission intensity from LMOF-271.¹²⁷⁻¹²⁸ In pristine samples of LMOF-271, anthracene groups may competitively absorb UV irradiation with the chromophore type, acting as built-in quenchers.¹²⁹ Upon exposure to CTC, the analyte enters the LMOF pores and interacts with anthracene moieties through charge-transfer mechanisms that diminish the absorbance of

anthracene.¹³⁰⁻¹³¹ Thus, anthracene groups can no longer inhibit type absorption, resulting in enhanced emission intensity.¹³²⁻¹³³ These results clearly support LMOF-271 as an effective optical detection material for CTC.

3.4 Conclusions

We have designed and synthesized a dual-linker LMOF that is tailored to interact with specific analytes through the functionalized dicarboxylate co-linker and give a specific emission from the chromophoric type. Through several characterization techniques, we have shown the ability for LMOF-271 to selectively interact with CTC over similar chloroalkane solvents (CLF and DCM). LMOF-271 exhibits a K_{SV} of $49,903 \text{ M}^{-1}$, which is the highest reported value to date for CTC detection, and an excellent detection limit of 22 ppb. Cost-effective optical materials that can detect ultra-low concentrations of toxic VOCs can simplify our efforts to protect the environment and human health on a global scale.

CHAPTER 4: LMOFs for Lithium Harvesting Applications

4.1 Introduction

Throughout the last decade, advancements in lithium-ion batteries have been a driving force for technological growth. Lithium extraction from natural resources has drawn increasing interest over that period as the demand for these batteries has escalated to satisfy rapid product development.¹³⁴⁻¹³⁵ Salt-lake brines are the primary source for lithium extraction, accounting for approximately 60% of the global lithium reserves,¹³⁶ and have the potential for larger-scale generation over an extended time compared to pegmatite deposits.¹³⁷ Common interferents within the salt-lake brines (Na^+ , Mg^{2+} , Ca^{2+}) diminish the selectivity of established lithium extraction techniques, including precipitation, ion-exchange, solvent extraction, nanofiltration, and

electrodialysis.¹³⁸⁻¹⁴¹ Separation of lithium from seawater is also affected by the presence of competing cations, and the challenges are intensified due to the lower average lithium concentration (0.17 mg/L, compared to approximately 1,226 mg/L in salt-lake brines).¹⁴²⁻¹⁴³ Despite the low concentration, seawater could provide a compliment to global lithium reserves since the amount of lithium is a few orders of magnitude higher than other critical and precious metals,¹⁴² however, the selectivity demonstrated by separation materials needs to be advanced.

Identifying potential salt-brine lakes for lithium extraction has proven to be arduous since many factors contribute to lithium concentration, including geothermal activity from volcanic systems and anatexis (differential melting of rocks),¹⁴³ among others. Lithium concentration also varies according to depth within a salt-brine lake¹⁴⁴ which complicates the harvesting process. The initial steps of lithium estimation, which must precede any harvesting, has been a very extended process based on innumerable samplings, chemical analyses, precipitation tests and expensive industrial operations.¹³⁴ The ability to quickly and easily detect low concentrations of lithium would lead to drastic cost reductions during the estimation phase. Additionally, using the same material for the sensing and extraction of lithium from water would be a valuable commodity for industrial applications.

Metal-organic frameworks (MOFs) are functional materials produced via the self-assembly of inorganic nodes (metal cations or complexes) with organic ligands. These coordination networks can be permanently porous, depending on their composition and pre-synthetic conditions.¹⁴⁵ Recently, luminescent metal-organic frameworks (LMOFs) have rapidly developed as effective sensors for various analytes.^{7, 18, 27, 41, 44-45, 146} Luminescence-based detection utilizes the change in photoluminescence from LMOFs to sense the presence of a target analyte and is an attractive transduction method due to its simplicity and wide applicability.¹⁴⁷ LMOFs have been previously

used for dual-performance applications in the selective sensing and extraction of metal ions,²⁷ taking advantage of ligand functionalization and permanent porosity. To date, no LMOFs have been used for lithium detection applications.

Fluorescent materials used for low-concentration lithium sensing encountered difficulties in selectivity over competing alkali and alkaline earth metals under aqueous conditions.¹⁴⁸⁻¹⁵⁰ Often, selective fluorescence sensors for lithium have functioned in homogeneous systems where water solubility is a desired technical characteristic.¹⁵¹⁻¹⁵³ Heterogeneous sensors are more advantageous for cost-reducing applications due to their facile recyclability. It is vital to develop sensor materials that address all the issues surrounding lithium sensing and extraction.

Zr-MOFs represent a chemically and thermally robust subcategory group of MOF materials,¹⁵⁴⁻¹⁵⁵ but there have been cases reporting difficulties in maintaining framework stability after increased surface modifications,¹⁵⁶ especially if pore dimensions need to be restricted for specific applications.¹⁵⁷ Dual-ligand Zr-MOFs provide an alternative to congested functionalities in single-linker systems. Active groups are separated onto different components and steric hindrance is minimized. However, dual-ligand MOFs have been arduous to synthesize due to the competition between kinetically- and thermodynamically-favored products. Bond formation between Zr^{4+} and carboxylates is exothermic and MOFs with highly-connected Zr_6 SBUs are preferred, limiting ligands with less desirable coordination characteristics from framework incorporation.²⁴⁻²⁶ Effective multivariate Zr-MOF preparation methods have been recently studied and open paths toward valuable material science solutions.^{25, 158}

The Zr-based LMOF-321 was successfully synthesized and is isorecticular to PCN-133.²⁴ Using size-matching strategies, we developed a functional dicarboxylate co-linker (H_2dsab) with a similar morphology and length to the bridging dicarboxylate ligand in PCN-133. H_2dsab contains

a central bis(sulfonyl)imide moiety that has demonstrated direct interactions with lithium under a variety of aqueous conditions. As a result, perturbations within the LMOF prompted an emission quenching proportional to lithium concentration exposure. Detection and extraction performances were monitored and highlight LMOF-321 as a promising material for lithium harvesting endeavors.

4.2 Experimental Details

4.2.1 Ligand Syntheses

Synthesis of H₂dsab

The synthesis of 4,4'-((hydrosulfonylamino)sulfonyl)dibenzoic acid (H₂dsab) was followed from reported procedures.¹⁵⁹ Toluene-4-sulfonamide (3.5 g, 20.4 mmol) was dissolved in NaOH_(aq) (35 mL H₂O, 863 mg/21.4 mmol NaOH) at 95 °C. Once dissolved, slowly add an equimolar amount of p-toluenesulfonyl chloride (3.9 g, 20.4 mmol). The mixture was stirred at reflux overnight. White precipitate (4,4'-dimethyldiphenylsulfonimide) formed under acidic conditions via the dropwise addition of conc. HCl to the reaction mixture.

Once the intermediate (1.5 g, 4.61 mmol) was filtered, washed extensively with water, and dried, it was subsequently dissolved with equimolar lithium hydroxide monohydrate (0.189 g, 4.61 mmol) in 30 mL water at 95 °C. Potassium permanganate (1.82 g, 11.5 mmol) was slowly added to the solution over 2 h and the system was stirred at reflux overnight. Residual solids (MnO₂, unreacted KMnO₄) were filtered and discarded, while the filtrate was acidified with conc. HCl

added dropwise. The final product (H₂dsab) was filtered, washed with water, and dried at 70 °C overnight. Figure 4.1 displays the ¹H-NMR for H₂dsab.

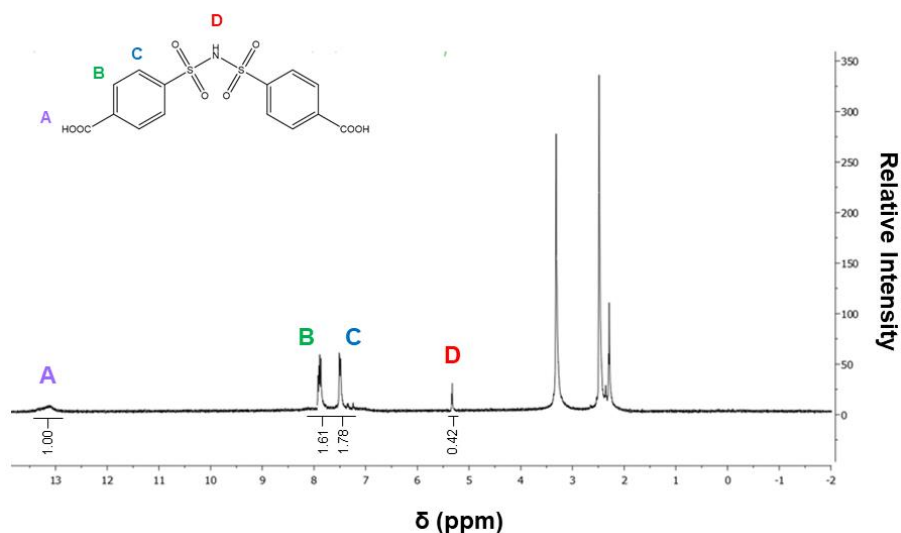


Figure 4.1. ¹H-NMR of H₂dsab with integrations and functional group assignments (inset). The shifts at 3.3, 2.5, and 2.09 ppm correspond to water and residual solvents (DMSO, acetone).

Synthesis of H₃btb

The linker benzene tribenzoic acid (H₃btb) was synthesized according to previous studies.^{24, 160} The intermediate 1,3,5-tris[(4-methoxycarbonyl)phenyl]benzene was formed through a Suzuki coupling from 1,3,5-tribromobenzene, which then underwent a hydrolysis reaction under basic conditions to form H₃btb.

4.2.2 Synthesis of Zr₆O₄(OH)₄(btb)₂(dsab)₃ (LMOF-321)

LMOF-321 was synthesized via a two-step solvothermal reaction. Initially, anhydrous ZrCl₄ (0.030 g, 0.13 mmol) and H₃btb (0.017 g, 0.040 mmol) were dissolved in a mixed-solvent system (DMF:iPrOH:DMSO, 4:1:1) and heated at 100 °C for 1 h. Next, H₂dsab (0.025 g, 0.065 mmol) was added to the mixture with an equal aliquot of the solvent system from the previous step. Formic acid was used at this stage as a modulating agent (3 mL). The mixture was sonicated

to ensure all solids were dissolved, then the vials were maintained at 120 °C for 72 h. After the reaction mixture was cooled to room temperature, pale-yellow needle crystals were collected via vacuum filtration and washed with DMF. This process was adopted from the sequential linker installation from Yuan et al.²⁴

4.2.3 Structural Analysis of LMOF-321

The powder X-ray diffraction (PXRD) patterns were collected on a Rigaku Ultima-IV diffractometer (at room temperature) using monochromatic Cu K α radiation ($\lambda = 1.5406 \text{ \AA}$). Data were collected between 3-40° 2 θ with step size 0.02° and scanning rate 1.5°/min. The diffraction pattern from LMOF-321 matches the diffraction pattern reported from Yuan et al.,²⁴ indicating the formation of a material that is isorecticular to PCN-133. The PXRD pattern overlay is provided in Figure 4.2.

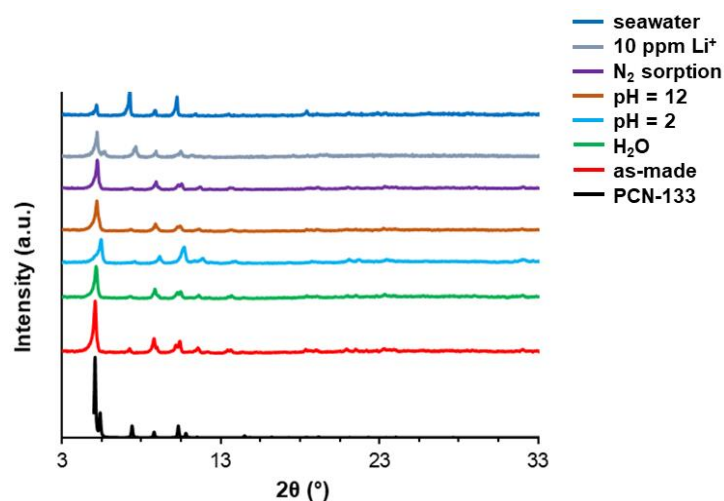


Figure 4.2. PXRD pattern comparison between PCN-133²⁴ and LMOF-321 exposed to various conditions.

The unit cell parameters for LMOF-321 were determined to be 20.062, 20.062, and 17.138 Å, respectively, for the a-, b-, and c-axes. The a- and b-axes shifted negligibly from the parameters in PCN-133,²⁴ however the elongation in the c-axis is consistent with the longer pillar ligand

(H₂dsab) used in place of the shorter dcdps linker in PCN-133 to extend the Zr-btb 2D sheets into three-dimensions.

4.2.4 Pore Characterization

Nitrogen adsorption-desorption isotherms of activated LMOF-321 were collected on a Quantachrome Instruments Autosorb-1 MP volumetric gas sorption analyzer using ultra high purity N₂ (99.999%). Liquid nitrogen was used as coolant to achieve cryogenic temperature (77 K). The N₂ isotherms were collected in a pressure range from 10⁻⁷ to 1 atm. The BET surface area was obtained using Autosorb v1.50 software. LMOF-321 was outgassed by first conducting a solvent-exchange with methylene chloride (3 d). Next, the sample was exposed to 70 °C for 6 h under reduced atmosphere. The N₂ adsorption isotherm for LMOF-321 is depicted in Figure 4.3, along with the H-K pore size distribution analysis. The BET surface area was determined to be 430 m²/g, and the average pore size 5.8-6.1 Å. The pore volume for LMOF-321 was 0.22 cm³/g. The pore diameters are wide enough to incorporate Li⁺ according to average ionic radii but may be size selective towards the larger hydrated alkali and alkaline metal ions.¹⁶¹

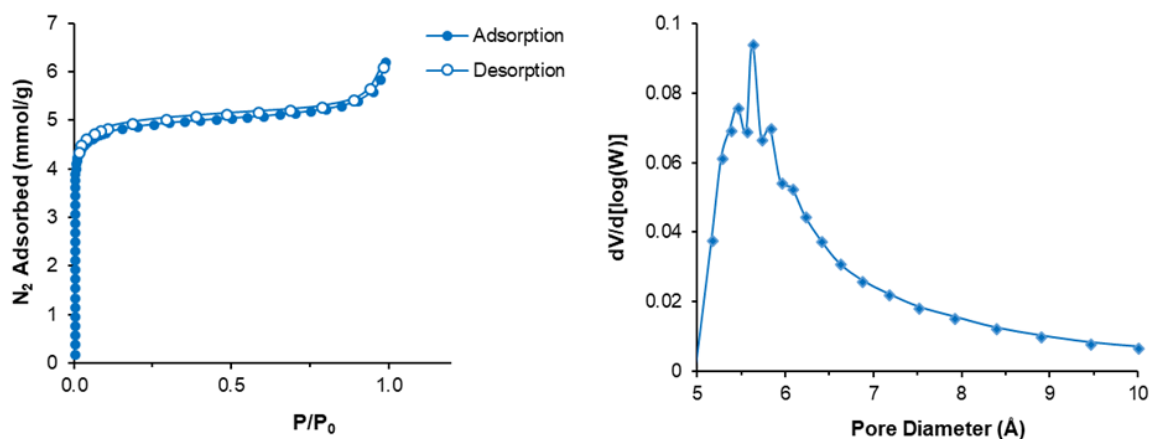


Figure 4.3. (left) N₂ adsorption and desorption isotherms for LMOF-321. (right) The H-K micropore size distribution analysis of LMOF-321, indicating nanopores in the range of 5.8-6.1 Å.

4.2.5 Additional Instrumental Details

Thermogravimetric Analysis

Thermogravimetric analysis (TGA) was performed using a TA Instruments Q5000 under constant N₂ flow (20 mL/min). Approximately 5 mg of sample was placed into a platinum pan, which was then heated from 30-500 °C at a rate of 10 °C/min. Figure 4.4 displays the TGA curve for as-made and activated LMOF-321. The material was activated after a solvent-exchange using DCM over 3 d, then heating at 70 °C under vacuum for 6 h.

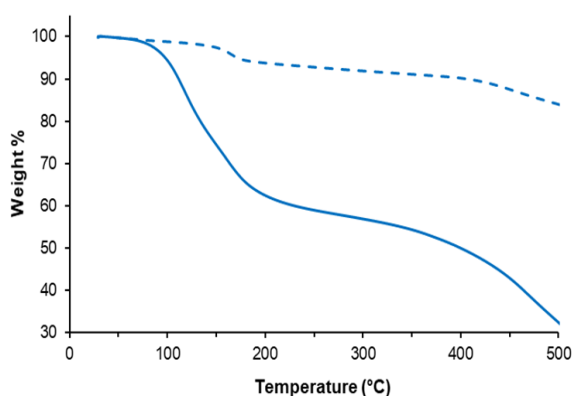


Figure 4.4. Thermogravimetric (TG) analysis of as-made (solid) and activated (dotted) LMOF-321.

Optical Characterization

UV-visible diffuse reflectance spectra were obtained for LMOF-321 and the fluorescent ligand H₃btb at room temperature using a Shimadzu UV-3600 spectrophotometer. The diffuse reflectance data was converted to the Kubelka-Munk Function following Equation 2.1. Plotted in Figure 4.5 are solid-state diffuse reflectance spectra for LMOF-321 and H₃btb. The estimated bandgap is blue-shifted as the fluorophore is incorporated into the framework.

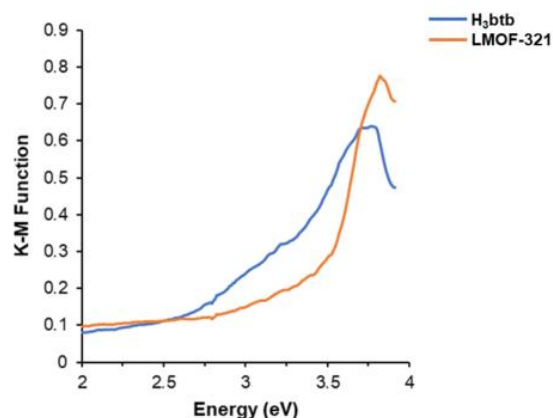


Figure 4.5. Optical absorption spectra (converted to KM Function) of as-made LMOF-321 (orange) and H₃btb (blue).

Using a Varian Cary Eclipse spectrophotometer, optical excitation and emission spectra were collected for as-made and activated LMOF-321, as well as H₃btb, depicted in Figure 4.6. The emission of LMOF-321 was red-shifted upon outgassing ($\lambda_{\text{em, as-made}} = 435 \text{ nm}$, $\lambda_{\text{em, outgassed}} = 455 \text{ nm}$) under UV excitation (365 nm). The fluorophore H₃btb emits at 450 nm under the same excitation.

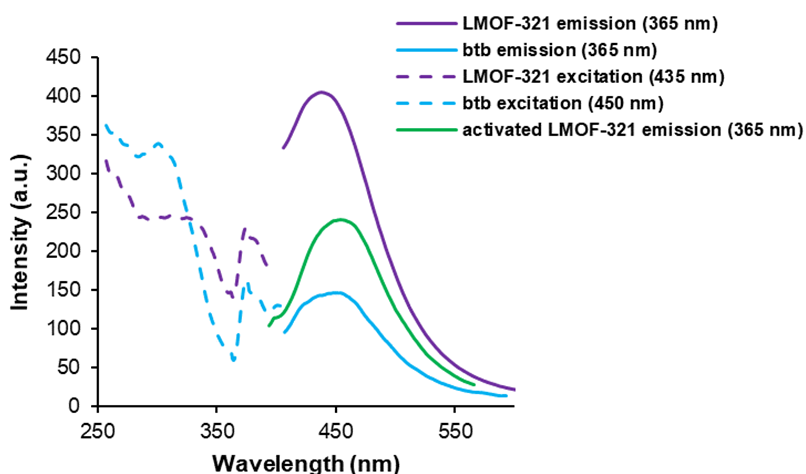


Figure 4.6. Optical emission and excitation spectra for LMOF-321 (as-made and activated) and H₃btb. Values in parentheses provide the emission or excitation wavelength at which the displayed excitation or emission spectra, respectively, were monitored.

Internal quantum yield (IQY) was measured using a Quantaaurus Absolute PL Quantum Yield Spectrophotometer C11347 with integrating sphere. Table 4.1 displays IQY data upon 360 nm excitation. When the fluorophore H₃btb is incorporated into PCN-133, negligible IQY enhancement is observed. However, upon immobilization into LMOF-321, the IQY is doubled from that of the molecular fluorophore.

Table 4.1. IQY data for as-made and outgassed samples of LMOF-321, H₃btb, and PCN-133.

	IQY (%)	
	As-made	Outgassed
LMOF-321	12.4	13.5
H ₃ btb	5.0	-
PCN-133	6.1	-

Inductively Coupled Plasma Optical Emission Spectroscopy

Inductively coupled plasma optical emission spectroscopy (ICP-OES) analyses were performed using a Spectro Arcos Analyzer. ICP-OES was used to determine the concentrations of various metal ions (Li⁺, Na⁺, Ca²⁺ and Mg²⁺) in aqueous solutions after various conditions, including single-metal, mixed-metal, timed-, and equilibrium concentration-exposures in suspensions of LMOF-321.

Fourier Transform Infrared Spectroscopy

Fourier transform infrared (FTIR) spectroscopy was used to identify any perturbations from phonon modes of LMOF-321 before and after Li⁺ exposure. For these measurements, the LMOF-321 samples were gently pressed onto a KBr pellet (~1 cm diameter, 1-2 mm thick). The pellet was placed into a high-pressure, high-temperature cell (product number P/N 5850c, Specac Ltd., UK) at the focal point of an IR spectrometer (Nicolet 6700, Thermo Scientific, US).

X-ray Photoelectron Spectroscopy

X-ray photoelectron spectroscopy (XPS) was employed to further investigate the interaction of Li^+ with LMOF-321. Information regarding changes in the electronic structure of N, the central atom of the bis(sulfonyl)imide functionality that represents the primary interaction site, before and after Li^+ exposure can be inferred by monitoring the nitrogen binding energy in LMOF-321. The samples were loaded on a KBr pellet (same procedure as in FTIR), using a Perkin Elmer PHI system equipped with a concentric hemispherical analyzer. An Al $K\alpha$ (1486.6 eV) monochromatic X-ray source at a chamber base pressure of <1.0 mTorr was used to excite photoelectrons.

4.2.6 Fluorescence Titrations

As-made LMOF-321 was placed into water and sonicated for 1 h. After forming a uniform suspension of LMOF-321 in water, photoluminescence (PL) titrations were carried out by incrementally adding aliquots of metal ion solutions to the sensor suspension under steady stirring. The emission spectra were recorded 5 min after adding the appropriate amount of metal ion solution. This exposure time ensured that metal ions entered the LMOF pores. Each measurement was repeated three-fold and the average value was used. Similar experiments were carried out in seawater (Easthampton, NY).

4.3 Results and Discussion

4.3.1 Synthesis of an Isorecticular Zr-MOF

As previously stated, LMOF-321 was determined to be isorecticular to PCN-133²⁴ from diffraction pattern comparisons (Figure 4.2). Unit cell parameters for LMOF-321 were calculated to be 20.062(7), 20.062, and 17.138(9) Å for the a-, b- and c-axes, respectively. There were negligible differences between the a- and b-axis parameters of LMOF-321 and PCN-133 because

the same tridentate linker (H_3btb) was used to form the 2D sheet. However, incorporation of a larger pillar ligand (H_2dsab) into LMOF-321 generated an elongation of the c-axis relative to PCN-133.²⁴ Through a heterostructural mixed linker approach¹⁶² and appropriate pre-synthetic modifications of the organic building blocks, a robust Zr-based LMOF was synthesized to selectively interact with lithium under aqueous conditions.

4.3.2 Lithium-Ligand Interactions

The optimization of materials for lithium-ion batteries has been a popular research focus for decades, including the search for exemplary electrolytes. Ideal battery electrolytes must be stable under specific conditions, however, most importantly, the electrolytes must reach certain ionic conductivity levels for the system to function. Bis(sulfonyl)imide groups have been identified as ideal components of electrolytic salts, as they interact efficiently with Li^+ ions under standard conditions of battery operation and ionic conductivities are higher compared to sulfonimide or traditional electrolytes (hexafluorophosphate salts, etc).¹⁶³ The high ionic conductivity of these salts was attributed to the outer trifluoromethyl moieties in bis(trifluoromethylsulfonyl)imide, which support electron-withdrawing effects and higher ionization degrees on the lithium-interaction sites.¹⁶³

Replacement of the outer functional group on the compound should promote different lithium conductivity performances. The ligand H_2dsab contains the central bis(sulfonyl)imide group with exterior benzoic groups—this linker structure promoted coordination in the dual-ligand Zr-MOF system and while also promoting interaction with Li^+ through the central moiety. Additionally, the presence of benzoic acid groups (electron-donating) instead of trifluoromethyl moieties (electron-withdrawing) lowered ionic conductivity and the dissociation rate of Li^+ from

the organic ligand. This resulted in stronger interactions with Li^+ , observed from sensing and extraction performances outlined below.

4.3.3 Optical Properties

Photoluminescence (PL) excitation and emission spectra were collected for LMOF-321 and the fluorophoric ligand H_3btb at room temperature (Figure 4.6). The ligand H_3btb showed blue emission when excited by UV light ($\lambda_{\text{ex}} = 365 \text{ nm}$) with an emission maximum at 450 nm, while LMOF-321 exhibits a maximum at 435 nm. After outgassing for 15 h under vacuum at 70 °C, the emission from LMOF-321 red-shifted to 455 nm. A Hamamatsu Quantaaurus Absolute PL Quantum Yield Spectrophotometer C11347 with integrating sphere was used to determine internal quantum yield (IQY) of LMOF-321, PCN-133 and H_3btb under 360 nm excitation (Table 4.1). Immobilization of a molecular chromophore has been shown to decrease nonradiative decay and promote higher quantum efficiencies.¹⁶ PCN-133 has an IQY just above that of H_3btb , however the LMOF-321 IQY increases two-fold from the molecular ligand. Thus, with the bis(sulfonyl)imide functionality and adequate IQY, LMOF-321 should be a suitable candidate for Li^+ sensing applications. The optical diffuse reflectance spectra of H_3btb and LMOF-321 were collected using a Shimadzu UV-3600 spectrophotometer, after which transformation to the Kubelka-Munk function allowed their optical band gaps to be estimated. The HOMO-LUMO energy gaps of H_3btb and LMOF-321 are estimated to be 2.8 and 3.2 eV, respectively (Figure 4.5).

4.3.4 Lithium Detection

Lithium has been projected to be a valuable resource to our global economy for decades to come. To increase the efficiency at which lithium is harvested from natural resources, effective probes need to be implemented to target specific areas/depths of brine lakes or oceans that have adequate lithium concentrations. Other alkali and alkaline earth metals (Na^+ , Ca^{2+} , Mg^{2+}) are

present in high concentrations, so selectivity for lithium is paramount for fluorescent detection materials.

Detection of lithium was performed by observing the changes in PL intensity from an aqueous LMOF-321 suspension, before and after addition of Li^+ solution. As a sensor for aqueous environments, it is important that LMOF-321 emission does not change after immersion in water. Figure 4.7a depicts the stagnant LMOF-321 emission ($\lambda_{\text{em}} = 435 \text{ nm}$, $\lambda_{\text{ex}} = 365 \text{ nm}$) after immersion in water for 15 h. LMOF-321 was stable in neutral, acidic, basic, and seawater samples, highlighting ideal traits for use in practical applications. The PL signal from the uniform LMOF-321 suspension diminished proportionally to the amount of Li^+ added to the system. Influence on the emission intensity varied depending on the metal analyte under observation.

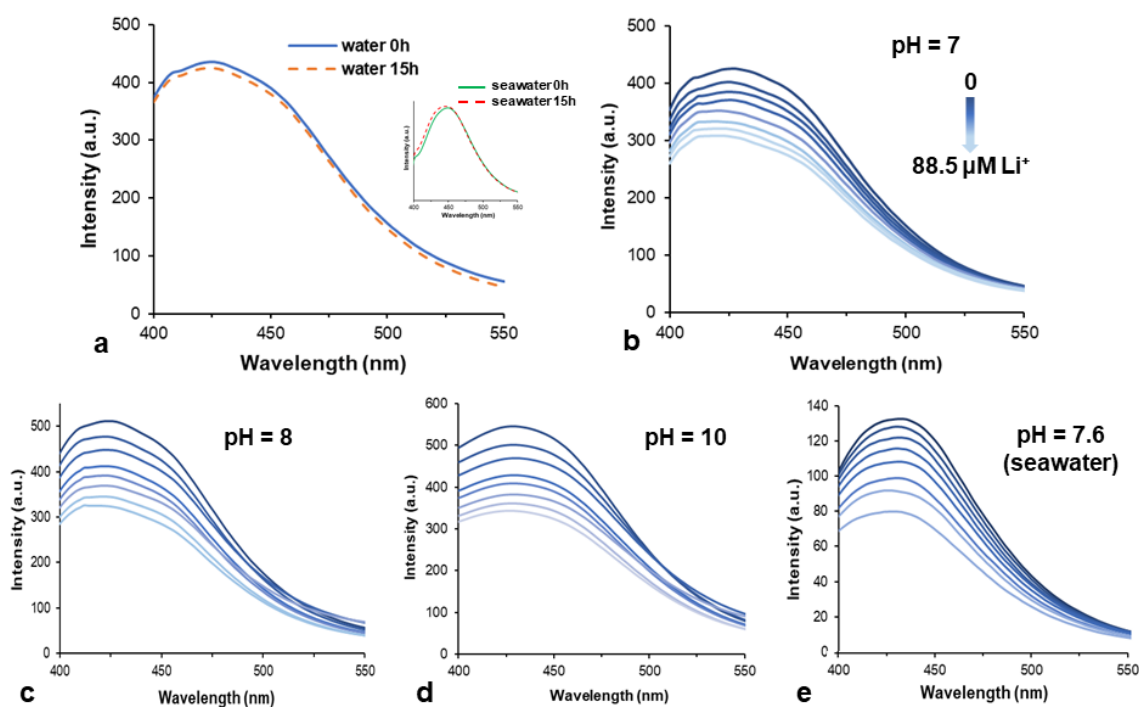


Figure 4.7. (a) LMOF-321 optical emission when immersed in water (0.25 g/L) initially and after 15 h. The inset depicts LMOF-321 emission stability during seawater exposure. (b) Emission spectra of LMOF-321 after incremental additions of an aqueous Li^+ solution under pH 7, (c) pH 8, and (d) pH 10. (e) PL titrations of LMOF-321 with Li^+ in seawater (pH 7.6). All emission spectra had $\lambda_{\text{ex}} = 365 \text{ nm}$.

LMOF-321 interacted with metal ions through the central bis(sulfonyl)imide functional group in the co-linker H₂dsab. It is vital that we examined the properties of the battery electrolyte from which the functionalized ligand is derived to understand the conditions for the best lithium-ligand interactions. The bis(trifluoromethylsulfonyl)imide group in the electrolyte is a strong acid,¹⁶⁴ aided by the charge stabilization from the outer, electron-withdrawing trifluoromethyl groups. The co-linker H₂dsab contains the bis(sulfonyl)imide group accompanied by benzoic acid moieties, so the electron-donating outer groups contribute to a weaker acidity compared to the parent electrolyte. To ensure deprotonation of the imide in H₂dsab, LMOF-321 aqueous suspensions were exposed to a variety of basic conditions and lithium-detection capabilities were compared.

Lithium detection was monitored through PL intensity changes from LMOF-321 under a pH of 7, 8, and 10 (Figure 4.7b-d). Furthermore, as shown in Figure 4.7e, LMOF-321 samples were suspended in seawater and titrated with Li⁺-doped seawater samples to display the practicality of the detection materials. The seawater samples had a pH of 7.6, measured on an American Marine Inc. Pinpoint pH meter. The maximum reduction of PL intensity from LMOF-321 was proportional to pH—the more basic system (pH = 10) prompted the highest quenching efficiency after exposure to lithium. The higher pH prompted increased access to the deprotonated imide within H₂dsab, allowing for more interactions with lithium. Further mechanistic insights are described below.

Upon addition of 614 ppb (88.5 μ M) Li⁺, emission from the LMOF-321 suspension was quenched by a maximum of 40% from the original intensity, achieved through PL titrations under pH 10. Compared to other metal ions (Na⁺, Ca²⁺, Mg²⁺), LMOF-321 was most responsive to Li⁺ under all conditions (Figure 4.8a). As a control, PCN-133 was suspended in water and used in

lithium detection trials (Figure 4.8b). There was no change in the PL signal from PCN-133, due to the absence of the H₂dsab linker and the bis(sulfonyl)imide interaction site. The quenching efficiency of LMOF-321 was calculated via the Stern-Volmer relationship, presented in Equation 2.2. The Stern-Volmer constant (K_{SV}) was used as the quantitative indicator of quenching efficiency and LMOF-321 performance as a sensor for metal ions in aqueous solution.

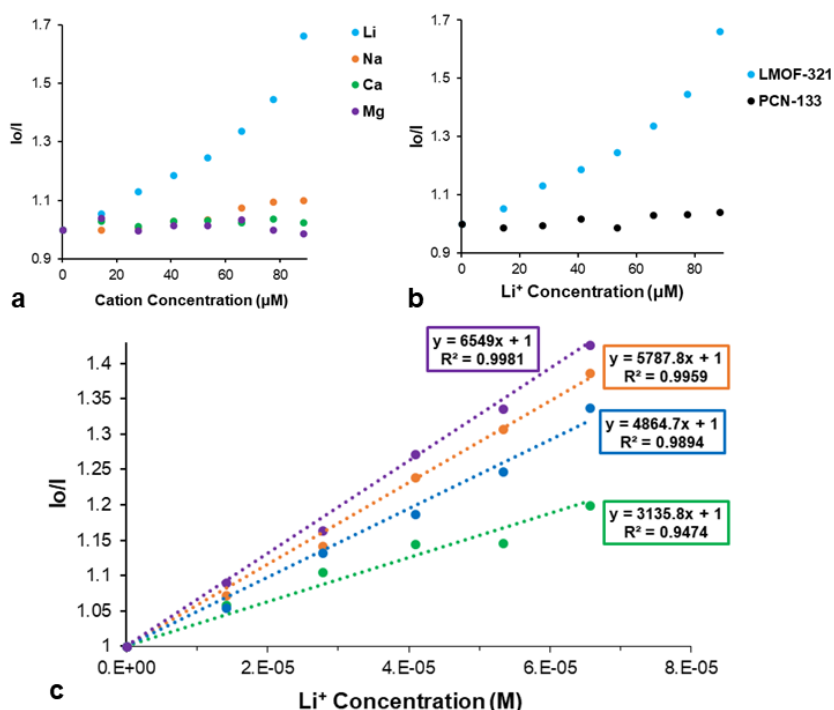


Figure 4.8. (a) Stern-Volmer (S-V) curves ($\lambda_{ex} = 365$ nm) of LMOF-321 for alkali and alkaline earth metals. High selectivity for Li⁺ is clearly visible. (b) S-V curves comparing the PL signal change from LMOF-321 and PCN-133 during Li⁺ exposure. (c) Low-concentration Li⁺ titrations immersed in pH 7 (green), seawater (pH 7.6, blue), pH 8 (orange) and pH 10 (purple). Equations represent the S-V relationship, with K_{SV} values provided under each condition. Average standard deviation values for pH = 7, 7.6, 8, and 10 titrations were 0.897, 0.849, 0.775, and 0.665 a.u., respectively.

At low concentrations, I_0/I increased linearly with metal ion concentration (Figure 4.8c). The maximum K_{SV} for Li⁺ was 6,549 M⁻¹, and the detection limit was determined to be 3.9 ppb in pH 10, which is below the average concentration of Li⁺ in seawater and brine-lakes.¹⁴²⁻¹⁴³ LMOF-321 demonstrated a selective interaction with Li⁺ over other interferent ions, with detection ratios of 7.7, 14.3, and 44.9 over Na⁺, Ca²⁺, and Mg²⁺, respectively. To date, MOFs have not been utilized

for lithium detection, so LMOF-321 sets the standard among this class of materials. LMOF-321 is well-matched with other types of fluorescent sensor materials that target lithium, including fluoroionophores,¹⁵³ nanoparticles,¹⁵⁰ and metallacrown-complexes,^{151-152, 165-167} among other compounds,^{148-149, 168-169} presenting comparable quantitative detection values.

Select metallacrown-complexes have exhibited impressive detection limits in deionized, tap, lake, and saline water,^{150, 167} however, the recyclability of these materials were never discussed. Pre-production costs for lithium-ion batteries need to be diminished so focus can be applied towards research and development. Reusable lithium sensors would be a valuable commodity for industrial endeavors.

The proposed interaction site on H₂dsab is the bis(sulfonyl)imide functional group, which is protonated under acidic conditions. The LMOF-321 detection capability is improved under basic conditions due to the deprotonation of the central imide, leaving a vacant site for Li⁺ interaction. To remove Li⁺ from the framework, Li⁺@LMOF-321 was stirred into 0.01 M HCl for 2 h. Protonation of the imide causes Li⁺ to dissociate from the imide and evacuate the pores. After Li⁺ exposure, the PL from LMOF-321 is quenched proportional to the Li⁺ concentration. However, the intensity reverts to the as-made signal in an acidic environment. Five full cycles of Li⁺- and HCl-exposure were conducted while observing the structural and PL stability of the system (Figure 4.9).

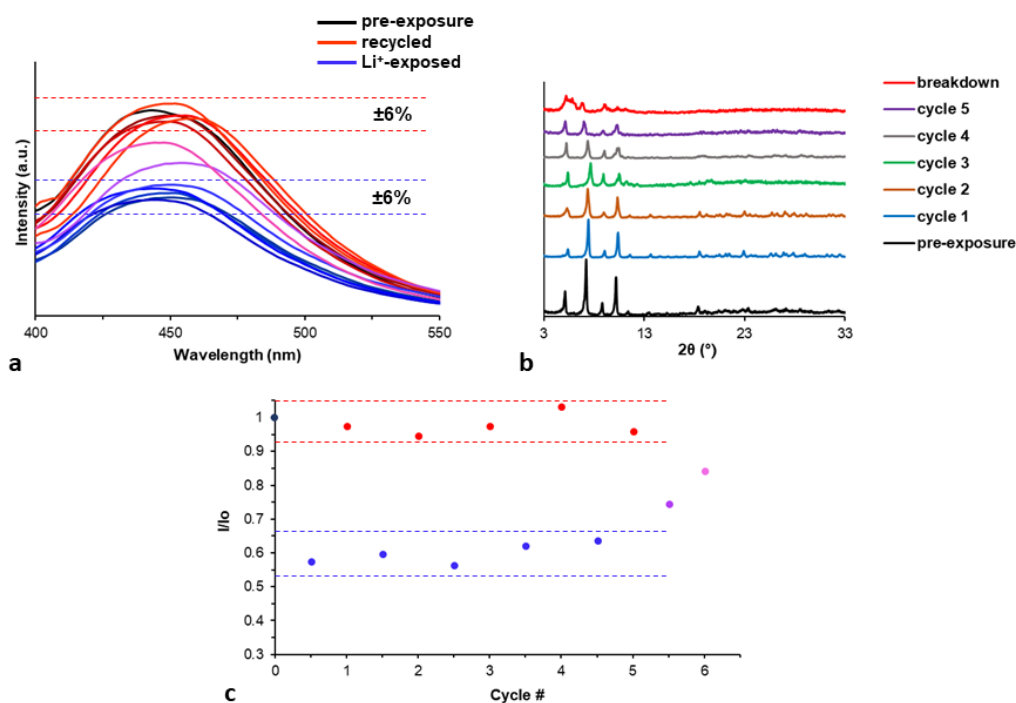


Figure 4.9. (a) Optical emission spectra of LMOF-321 as-made (black) and after successive Li⁺- (blue) and HCl-exposures (red). A maximum emission within $\pm 6\%$ of the as-made and initially Li⁺-quenched spectra were considered recycled. Pink and purple spectra correspond to PL emissions from degraded products. (b) PXRD overlay of LMOF-321 samples after each successive regeneration cycle. The red diffraction pattern represents a breakdown of the framework after five full cycles. (c) PL intensity ratios of LMOF-321 at each Li⁺-adsorption and -desorption stage of the regeneration cycle.

The structure of LMOF-321 was maintained through five full cycles, depicted in Figure 4.9b. After the sixth cycle, the framework degrades according to the diffraction pattern and is also evident from the PL spectrum—upon Li⁺ exposure the emission intensity was not quenched to the same extent as the five previous cycles, and similarly the PL intensity was not reverted to the pristine condition when reintroduced to an acidic environment (purple and pink spectra, Figure 4.9a,c).

In addition to recycling properties, LMOF-321 was utilized for the extraction of lithium from aqueous solution, an application not demonstrated among other sensor materials.

4.3.5 Lithium Extraction

Previous lithium detection materials have not exhibited simultaneous extraction abilities. Dual-performance compounds would be crucial to increasing the lithium harvesting efficiency that should become necessary as demand for the resource intensifies.

Evident from detection analyses, selectivity is vital for lithium separation materials, especially in environments such as brine-lakes or seawater when interferent concentrations are orders of magnitude higher than lithium. To analyze the lithium extraction ability of LMOF-321, activated samples (5.6, 11.2, and 16.8 mg; 0.059 mM, 0.119 mM, and 0.178 mM, respectively) were placed in aqueous solutions of either LiCl, NaCl, CaCl₂, or MgCl₂ (35 mL, M^{+/2+} concentration of 10 ppm, or ~350 µg of M^{+/2+}). The suspensions were agitated at room temperature for 15 h, after which the supernatant was separated from the adsorbent. The residual metal ion concentrations were measured via ICP-OES using a Spectro Arcos analyzer. As depicted in Figure 4.10a, LMOF-321 removes 38.3% of Li⁺ from solution, effectively lowering the concentration from 10 ppm (35 mL) to 6.16 ppm (16.8 mg LMOF-321, 0.178 mM). Under the same conditions, the adsorbent reduces the concentration of Na⁺, Ca²⁺, and Mg²⁺ from 10 ppm to 7.71, 9.67, and 8.32 ppm, respectively. Molar selectivity for Li⁺/Na⁺, Li⁺/Ca²⁺, and Li⁺/Mg²⁺ were 5.6, 67.2, and 8.0, respectively, emphasizing the preference of LMOF-321 towards lithium.

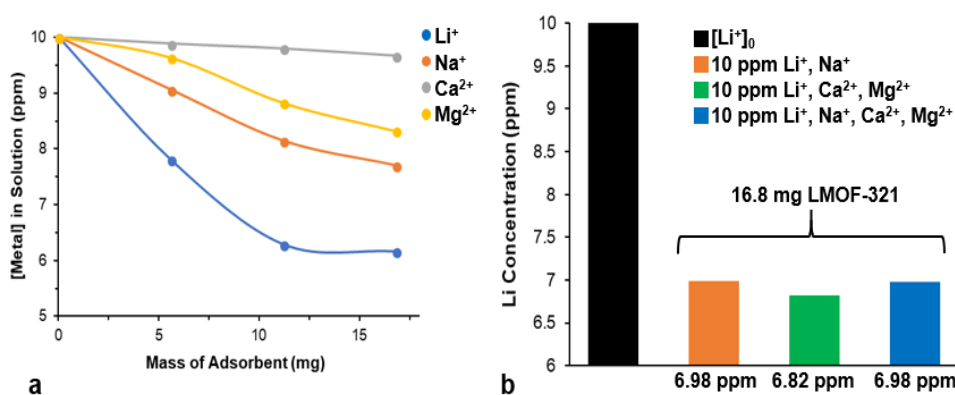


Figure 4.10. (a) The remaining metal concentrations after exposure to various amounts of LMOF-321. (b) Residual Li⁺ concentrations from mixed-metal solution exposures.

To function in practical environments, LMOF-321 must demonstrate similar Li^+ extraction performances when immersed with interferences. Solutions with 10 ppm Li^+ and Na^+ were exposed to LMOF-321 to further evaluate lithium selectivity (Figure 4.10b). Additionally, the adsorbent was mixed with a solution containing 10 ppm of Li^+ , Ca^{2+} , and Mg^{2+} as well as a system including all four metal ions (10 ppm). Under competitive conditions, the Li^+ concentration was reduced to 6.98, 6.82, and 6.98 ppm when LMOF-321 was exposed to ions Li^+/Na^+ , $\text{Li}^+/\text{Ca}^{2+}/\text{Mg}^{2+}$, and $\text{Li}^+/\text{Na}^+/\text{Ca}^{2+}/\text{Mg}^{2+}$, respectively. Interferent ions have minimal effects on the Li^+ -extraction performance of LMOF-321, which still removes 82.8% of the amount of Li^+ that was removed under non-competitive conditions. The order of selectivity in LMOF-321 follows $\text{Li}^+ > \text{Na}^+ > \text{Mg}^{2+} \geq \text{Ca}^{2+}$, which was consistent with observations from the detection analysis.

The rate kinetics of LMOF-321 for lithium were examined. LMOF-321 (16 mg, 0.170 mM) was exposed to an aqueous solution of 10 ppm Li^+ for specific time intervals. Portrayed in Figure 4.11, LMOF-321 exhibited pseudo-second-order adsorption kinetics with a relatively rapid uptake ($5.61 \text{ mg mg}^{-1} \text{ min}^{-1}$). The experimental data were fitted with the pseudo-second-order kinetic model using Equation 2.3. Approximately 85% of the total Li^+ removed from solution was extracted by LMOF-321 within 2 h. The composite adsorbent PSS@HKUST-1 exhibited a higher selectivity towards lithium compared to other metals, but extraction kinetics were not analyzed and the material was not reported to have sensing capabilities.¹⁷⁰

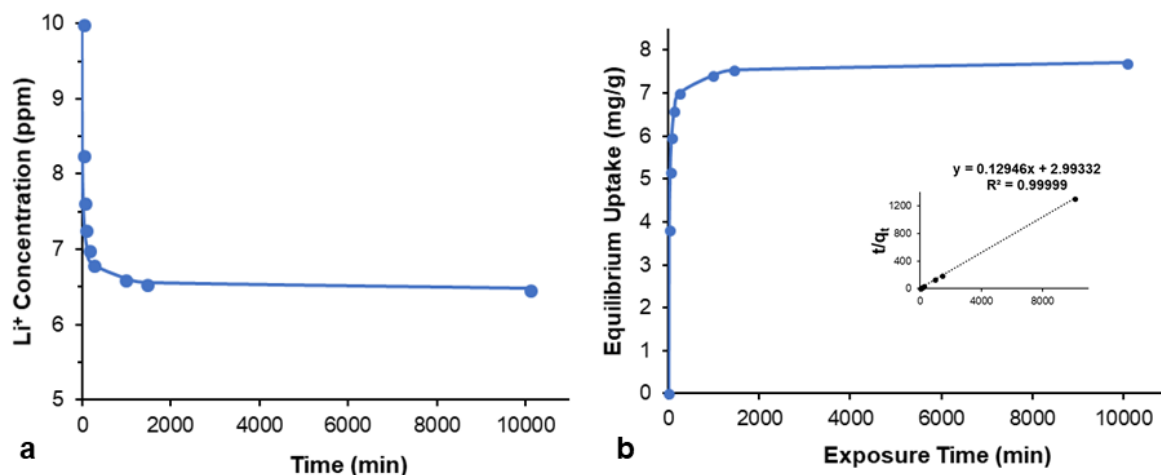


Figure 4.11. (a) Li⁺ concentrations after exposure to LMOF-321 for various time intervals. (b) The amount of adsorbed Li⁺ as a function of exposure time. The inset shows the pseudo-second-order kinetic plot for Li⁺ adsorption (initial Li⁺ concentration: 10 ppm), which was used to determine the kinetic rate constant (0.0056 g mg⁻¹ min⁻¹).

Adsorption of lithium within LMOF-321 was best evaluated using the Langmuir model, following the relationship displayed in Equation 4.1.

$$Q_m = \frac{Q_m K_L C_e}{1 + K_L C_e}$$

Equation 4.1. Langmuir adsorption model.

where C_e is the concentration of Li⁺ under equilibrium, Q_m is the maximum quantity of Li⁺ adsorbed onto LMOF-321 (monolayer capacity), K_L is the Langmuir constant and Q_e is the quantity of Li⁺ adsorbed under equilibrium. The better fit from the Langmuir model suggests monolayer adsorption onto homogeneous interaction sites, consistent with the crystalline structure of LMOF-321, with bis(sulfonyl)imide groups in regular locations throughout the framework. Figure 4.12 displays the Langmuir isotherm, from which we determined the maximum adsorption capacity of Li⁺ onto LMOF-321 to be 12.18 mg/g (K_L : 0.23 L/mg). Although other types of materials have reported higher lithium maximum adsorption capacities,¹⁷¹⁻¹⁷³ LMOF-321

exhibited comparable performances with Mn_xO_y species¹⁷⁴ and is the only adsorbent that was also used as an effective and simple lithium detector. This represents the first time a MOF has been used for the selective detection and simultaneous extraction of lithium from water.

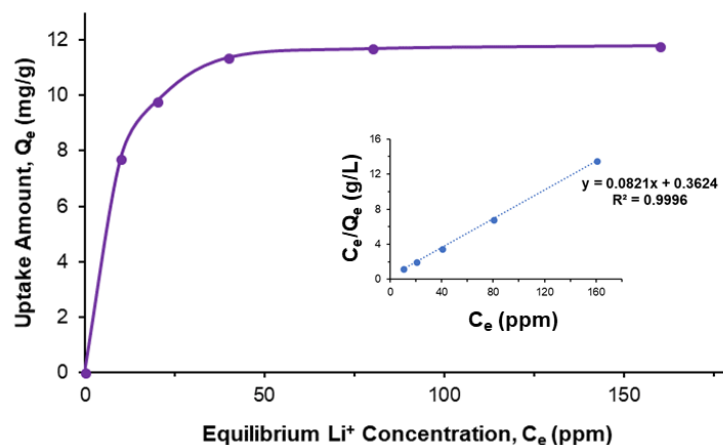


Figure 4.12. Adsorption isotherm of Li^+ on LMOF-321. The inset shows experimental values fit with the Langmuir model.

4.3.6 Interaction Mechanism

Details regarding the specific interaction of Li^+ with LMOF-321 have been obtained from IR and XPS spectroscopic investigation. FTIR spectroscopy was used to monitor vibrational modes from the sulfonyl groups to highlight the contact between Li^+ and bis(sulfonyl)imide moiety within the functional co-ligand H_2dsab . Figure 4.13 portrays the FTIR spectrum of pristine H_2dsab before LMOF-321 incorporation. The peaks at 1090, 1288, and 3350 cm^{-1} correspond to symmetric and asymmetric vibrational modes of the sulfonyl groups, as well as the stretching mode of the central imide, respectively. This imide stretching peak was not present in the bulk LMOF samples due to its overlapping with broad $\nu(\text{OH})$ band from adsorbed water inside MOFs. Difference spectrum in Figure 4.13 shows that the $\nu_{\text{as,s}}(\text{SO}_2)$ bands at 1090 and 1288 cm^{-1} exhibited significant perturbations after exposure to Li^+ , indicating contact and/or interaction between the metal and the sulfone groups within H_2dsab . X-ray photoelectron spectroscopy (XPS), focusing on the N 1s

binding energy, can help to elucidate the interaction between Li^+ and the central imide within the bis(sulfonyl)imide group.

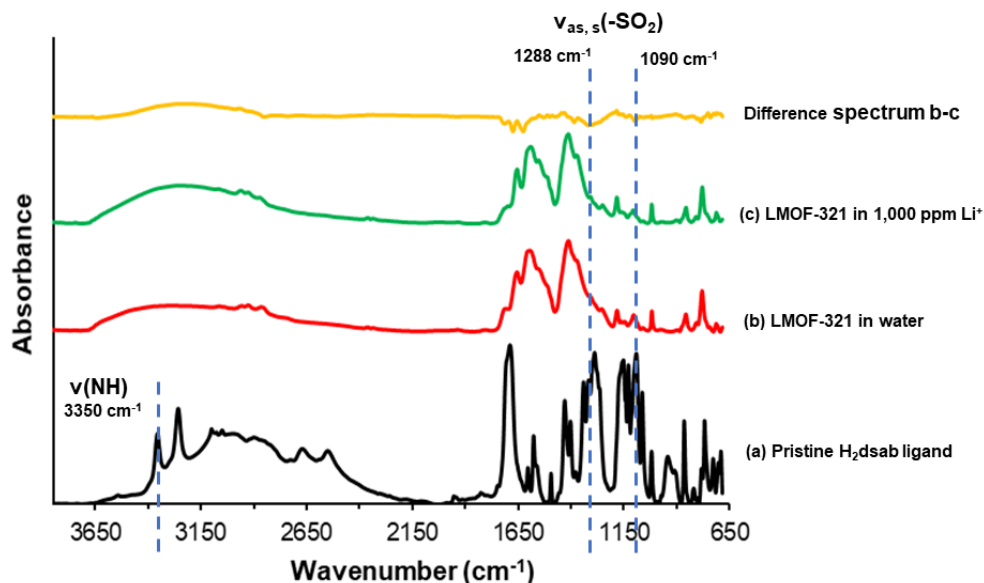


Figure 4.13. FTIR spectra for pristine H_2dsab and LMOF-321 samples [reference to KBr pellet in vacuum (<20 mTorr)]. Black labels are used to identify peaks related to the sulfone and imide moieties. (a) The spectrum for the pristine H_2dsab ligand, highlighting peaks representing the imide and sulfone groups. (b) The spectrum of LMOF-321 exposed to water is compared with (c) LMOF-321 after exposure to $\text{Li}^+_{(\text{aq})}$ solution. The top difference spectrum, obtained by subtracting spectrum b from c, shows the perturbations of the asymmetric and symmetric sulfone vibrational modes after Li^+ -exposure.

To further confirm the interaction between Li^+ and the bis(sulfonyl)imide moiety, XPS was used to monitor the nitrogen (N 1s) binding energy in water-immersed, Ca^{2+} -, and Li^+ -exposed LMOF-321 samples. The imide stretching modes were absent in the bulk LMOF FTIR spectra, so this is mandatory to understand the adsorption between metal ions and the bis(sulfonyl)imide group. Information regarding changes in the electronic structure of nitrogen, the central atom of the bis(sulfonyl)imide functionality that represents the primary interaction site, before and after Li^+ exposure can be inferred by monitoring the N 1s binding energy in LMOF-321. Figure 4.14 displays the shifting of N 1s binding energies. After Ca^{2+} -exposure, the N 1s binding energy shifted by 0.4 eV from the water-exposed sample. Similarly, after immersion in a Li^+ solution, this N 1s

binding energy shifted by 0.1 eV. The higher valence state associated with Ca^{2+} attracts more electrons from the central imide group, shifting the core level binding energy more compared to Li^+ . This binding energy shift, paired with FTIR results, supports the observations from detection and extraction analyses. LMOF-321 selectively interacts with metals through direct contact with the bis(sulfonyl)imide moiety in the H_2dsab co-linker, exhibiting selectivity for lithium over other alkali and alkaline earth elements.

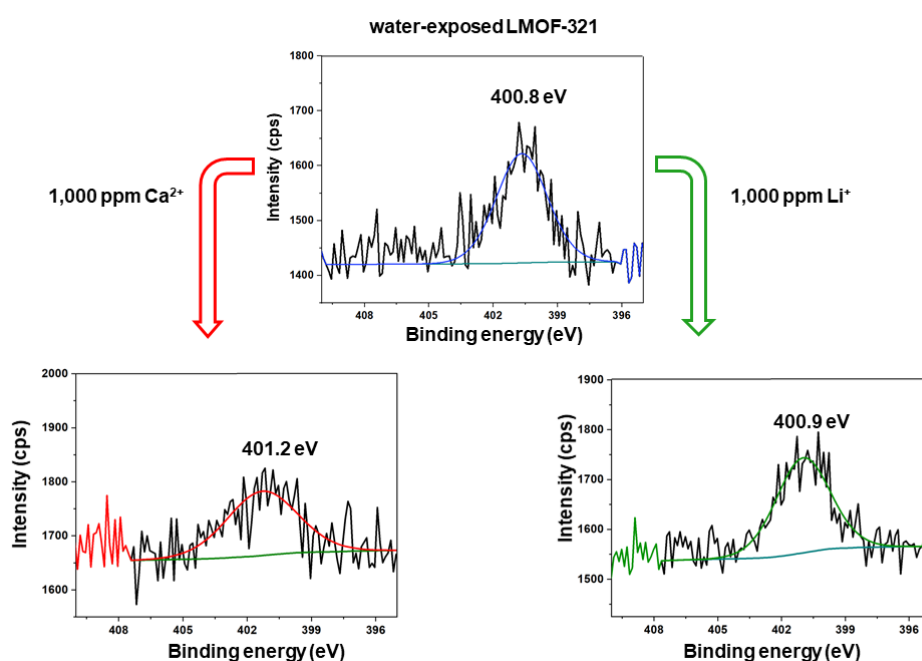


Figure 4.14. XPS spectra of LMOF-321 exposed to water (no $\text{M}^{+/2+}$) as reference, and 1,000 ppm solutions of Ca^{2+} and Li^+ . The shift in N 1s binding energy observed in both exposures indicates direct interaction with the imide in the bis(sulfonyl)imide functional group.

4.4 Conclusions

We have designed, synthesized and structurally characterized a new and robust Zr_6 -based, dual-linker LMOF that contained a fluorophore paired with a pillaring dicarboxylate co-ligand. This linker included a central functionality that accentuated selective interactions with lithium over common interferent ions (Na^+ , Ca^{2+} , Mg^{2+}). Detection analyses were carried out on aqueous

suspensions of LMOF-321 under several alkaline conditions, monitoring the performance of the sensor as the central imide group was deprotonated and made available for enhanced interactions with Li^+ . The limit of detection for this system was determined to be 3.9 ppb with an impressive and selective uptake for lithium (12.18 mg Li^+ /g). The selectivity towards lithium was consistent between photoluminescence sensing experiments and extraction analyses. XPS and FTIR confirmed the interaction between Li^+ and the bis(sulfonyl)imide moiety on the central position in H_2dsab .

There are no lithium adsorbent materials that have demonstrated a simple and effective sensing response. The sensitivity of this response, coupled with extraction capabilities, propels LMOF-321 as a standard for industrial lithium harvesting materials, especially in the resource estimation phase (before harvesting). Using a single material to identify areas of the ocean and/or salt-lake brines that are ideal candidates for lithium removal while simultaneously executing the extraction process would lower industrial costs early in the economic timeline. The resulting decline of prices for lithium-ion batteries and associated devices would not only benefit current consumers, but the increased supply of this resource could also generate innovation and development of technologies to a previously unimagined level.

CHAPTER 5: Conclusions and Outlook

My dissertation has focused on the use of LMOFs for environmental sensing, waste removal, and industrial harvesting applications. The crystallinity of LMOFs offers the opportunity to observe precise locations of framework-analyte interaction, enabling systematic optimization during the design and synthetic stages of this research. Materials have been chemically modified

and tailored to adsorb specific species in aqueous and organic media, while exhibiting optical activity that prompts changes in photoemission properties after exposure to the targeted analyte.

LMOFs towards the chemosensing of vital environmental contaminants compared favorably with current detection materials available today. However, it has been extremely rare for sensing methods to effectively remove pollutants simultaneously. The porosity, notable surface area, and precise functionality within LMOFs facilitate their efficacy as dual-performance materials, boasting low limits of detection and high adsorption capacities for specific analytes. Beyond their vital use for environmental remediation, materials presented in this work provide important roles in industrial operations. These LMOFs have been used to target and extract vital elements for the energy sector in an efficient manner. These applications could increase supplies, lower costs, and empower further scientific advancement to new frontiers.

The facile chemical modifications for LMOFs highlight their capability for enhanced performances. The projects presented in this dissertation represent valuable steps for environmental and industrial processes, but they are among only the first stages. Pore sizes can be tailored for physical constraint, and functional groups can be optimized for specific chemical environments within the channels and voids of the frameworks under observation. The possibilities for LMOF design and synthesis are infinite and can be beneficial towards adverse issues.

Overall, my graduate research has allowed me to investigate advanced organic syntheses to create new ligands with distinct functionalities, while also incorporating these organic compounds into interesting hybrid inorganic-organic materials. The opportunity to develop and advance the fields of solid-state chemistry and metal-organic frameworks towards environmental applications that provide global benefits has been incredibly rewarding, and I hope this work brings motivation to subsequent researchers.

List of Abbreviations

DMA	N,N'-dimethylacetamide
DMF	N,N'-dimethylformamide
DMSO	dimethylsulfoxide
FTIR	fourier-transform infrared spectroscopy
H ₂ adc	9,10-anthracene dicarboxylic acid
H ₃ btb	benzene tribenzoic acid
HCl	hydrochloric acid
H ₂ dbtdcO ₂	dibenzo[<i>b,d</i>]thiophene-3,7-dicarboxylic acid-5,5-dioxide
H ₂ dsab	4,4'-((hydrosulfonylamino)sulfonyl)dibenzoic acid
H ₂ hfdc	9H-fluorene-2,7-dicarboxylate
H ₂ ofdc	9-oxo-9H-fluorene-2,7-dicarboxylic acid
HOMO	highest occupied molecular orbital
ICP-OES	inductively-coupled plasma optical emission spectroscopy
iPrOH	isopropanol
IQY	internal quantum yield
LMOF	luminescent metal-organic framework
LUMO	lowest unoccupied molecular orbital
MOF	metal-organic framework
NaOH	sodium hydroxide
PBU	primary building unit
PL	photoluminescence
PXRD	powder X-ray diffraction
SBU	secondary building unit
TGA	thermogravimetric analysis
tpe	1,1,2,2-tetraphenylethene
tppe	1,1,2,2-tetrakis(4-(pyridine-4-yl)phenyl)ethane
UV-Vis	ultraviolet-visible spectroscopy
XPS	X-ray photoelectron spectroscopy
XRF	X-ray fluorescence spectroscopy

References

1. Batten, S. R.; Champness, N. R.; Chen, X.-M.; Garcia-Martinez, J.; Kitagawa, S.; Öhrström, L.; O'Keeffe, M.; Suh, M. P.; Reedijk, J., Coordination Polymers, Metal–Organic Frameworks and the Need for Terminology Guidelines. *Cryst. Eng. Comm.* **2012**, *14*, 3001-3004.
2. Tranchemontagne, D. J.; Mendoza-Cortes, J. L.; O'Keeffe, M.; Yaghi, O. M., Secondary Building Units, Nets and Bonding in the Chemistry of Metal–Organic Frameworks. *Chem. Soc. Rev.* **2009**, *38*, 1257-1283.
3. Bao, Z.; Chang, G.; Xing, H.; Krishna, R.; Ren, Q.; Chen, B., Potential of Microporous Metal–Organic Frameworks for Separation of Hydrocarbon Mixtures. *Energy Environ. Sci.* **2016**, *9*, 3612-3641.
4. He, Y.; Zhou, W.; Krishna, R.; Chen, B., Microporous Metal–Organic Frameworks for Storage and Separation of Small Hydrocarbons. *Chem. Commun.* **2012**, *48*, 11813-11831.
5. Liu, J.; Chen, L.; Cui, H.; Zhang, J.; Zhang, L.; Su, C. Y., Applications of Metal–Organic Frameworks in Heterogeneous Supramolecular Catalysis. *Chem. Soc. Rev.* **2014**, *43*, 6011-6061.
6. Morozan, A.; Jaouen, F., Metal–Organic Frameworks for Electrochemical Applications. *Energy Environ. Sci.* **2012**, *5*.
7. Lustig, W. P.; Mukherjee, S.; Rudd, N. D.; Desai, A. V.; Li, J.; Ghosh, S. K., Metal–Organic Frameworks: Functional Luminescent and Photonic Materials for Sensing Applications. *Chem. Soc. Rev.* **2017**, *46*, 3242-3285.
8. Ke, F.; Yuan, Y.-P.; Qiu, L.-G.; Shen, Y.-H.; Xie, A.-J.; Zhu, J.-F.; Tian, X.-Y.; Zhang, L.-D., Facile Fabrication of Magnetic Metal–Organic Framework Nanocomposites for Potential Targeted Drug Delivery. *J. Mater. Chem.* **2011**, *21*, 3843-3848.
9. Ray Chowdhuri, A.; Bhattacharya, D.; Sahu, S. K., Magnetic Nanoscale Metal–Organic Frameworks for Potential Targeted Anticancer Drug Delivery, Imaging and as an MRI Contrast Agent. *Dalton Trans.* **2016**, *45*, 2963-2973.
10. Song, B.-Q.; Wang, X.-L.; Yang, G.-S.; Wang, H.-N.; Liang, J.; Shao, K.-Z.; Su, Z.-M., A Polyrotaxane-like Metal–Organic Framework Exhibiting Luminescent Sensing of Eu³⁺ Cations and Proton Conductivity. *CrystEngComm* **2014**, *16*, 6882-6888.
11. Heine, J.; Muller-Buschbaum, K., Engineering Metal-based Luminescence in Coordination Polymers and Metal–Organic Frameworks. *Chem. Soc. Rev.* **2013**, *42*, 9232-9242.
12. Yang, Y.; Zhao, Q.; Feng, W.; Li, F., Luminescent Chemodosimeters for Bioimaging. *Chemical reviews* **2013**, *113*, 192-270.
13. Diamantis, S. A.; Margariti, A.; Pournara, A. D.; Papaefstathiou, G. S.; Manos, M. J.; Lazarides, T., Luminescent Metal–Organic Frameworks as Chemical Sensors: Common Pitfalls and Proposed Best Practices. *Inorg. Chem. Frontiers* **2018**, *5*, 1493-1511.
14. Zhou, Q.; Swager, T. M., Fluorescent Chemosensors Based on Energy Migration in Conjugated Polymers: The Molecular Wire Approach to Increased Sensitivity. *J. Am. Chem. Soc.* **1995**, *117*, 12593-12602.
15. Swager, T. M., Iptycenes in the Design of High Performance Polymers. *Acc. Chem. Res.* **2008**, *41*, 1181-1189.
16. Wei, Z.; Gu, Z. Y.; Arvapally, R. K.; Chen, Y. P.; McDougald, R. N., Jr.; Ivy, J. F.; Yakovenko, A. A.; Feng, D.; Omary, M. A.; Zhou, H. C., Rigidifying Fluorescent Linkers by Metal–Organic Framework Formation for Fluorescence Blue-Shift and Quantum Yield Enhancement. *J. Am. Chem. Soc.* **2014**, *136*, 8269-8276.

17. Gong, Q.; Hu, Z.; Deibert, B. J.; Emge, T. J.; Teat, S. J.; Banerjee, D.; Mussman, B.; Rudd, N. D.; Li, J., Solution Processable MOF Yellow Phosphor with Exceptionally High Quantum Efficiency. *J. Am. Chem. Soc.* **2014**, *136*, 16724-16727.
18. Hu, Z.; Deibert, B. J.; Li, J., Luminescent Metal-Organic Frameworks for Chemical Sensing and Explosive Detection. *Chem. Soc. Rev.* **2014**, *43*, 5815-5840.
19. Dai, J.-C.; Wu, X.-T.; Fu, Z.-Y.; Hu, S.-M.; Du, W.-X.; Cui, C.-P.; Wu, L.-M.; Zhang, H.-H.; Sun, R.-Q., A Novel Ribbon-Candy-like Supramolecular Architecture of Cadmium(ii)-Terephthalate Polymer with Giant Rhombic Channels: Twofold Interpenetration of the 3D 8210-a Net. *Chem. Commun.* **2002**, *1*, 12-13.
20. Wang, B.; Lv, X. L.; Feng, D.; Xie, L. H.; Zhang, J.; Li, M.; Xie, Y.; Li, J. R.; Zhou, H. C., Highly Stable Zr(IV)-Based Metal-Organic Frameworks for the Detection and Removal of Antibiotics and Organic Explosives in Water. *J. Am. Chem. Soc.* **2016**, *138*, 6204-6216.
21. Howarth, A. J.; Liu, Y.; Li, P.; Li, Z.; Wang, T. C.; Hupp, J. T.; Farha, O. K., Chemical, Thermal and Mechanical Stabilities of Metal-Organic Frameworks. *Nat. Rev. Mater.* **2016**, *1*, 1-15.
22. Bai, Y.; Dou, Y.; Xie, L. H.; Rutledge, W.; Li, J. R.; Zhou, H. C., Zr-based Metal-Organic Frameworks: Design, Synthesis, Structure, and Applications. *Chem. Soc. Rev.* **2016**, *45*, 2327-2367.
23. Chen, W.; Wang, J.-Y.; Chen, C.; Yue, Q.; Yuan, H.-M.; Chen, J.-S.; Wang, S.-N., Photoluminescent Metal-Organic Polymer Constructed from Trimetallic Clusters and Mixed Carboxylates. *Inorg. Chem.* **2003**, *42*, 944-946.
24. Yuan, S.; Qin, J. S.; Zou, L.; Chen, Y. P.; Wang, X.; Zhang, Q.; Zhou, H. C., Thermodynamically Guided Synthesis of Mixed-Linker Zr-MOFs with Enhanced Tunability. *J. Am. Chem. Soc.* **2016**, *138*, 6636-6642.
25. Yuan, S.; Lu, W.; Chen, Y. P.; Zhang, Q.; Liu, T. F.; Feng, D.; Wang, X.; Qin, J.; Zhou, H. C., Sequential Linker Installation: Precise Placement of Functional Groups in Multivariate Metal-Organic Frameworks. *J. Am. Chem. Soc.* **2015**, *137*, 3177-3180.
26. Cohen, S. M., Postsynthetic Methods for the Functionalization of Metal-Organic Frameworks. *Chem. Rev.* **2012**, *112*, 970-1000.
27. Rudd, N. D.; Wang, H.; Fuentes-Fernandez, E. M.; Teat, S. J.; Chen, F.; Hall, G.; Chabal, Y. J.; Li, J., Highly Efficient Luminescent Metal-Organic Framework for the Simultaneous Detection and Removal of Heavy Metals from Water. *ACS Appl. Mater. Inter.* **2016**, *8*, 30294-30303.
28. Hanna-Attisha, M.; LaChance, J.; Sadler, R. C.; Champney Schnepf, A., Elevated Blood Lead Levels in Children Associated With the Flint Drinking Water Crisis: A Spatial Analysis of Risk and Public Health Response. *Am. J. Public Health* **2016**, *106*, 283-290.
29. Bai, L.; Wang, Y.; Guo, Y.; Zhou, Y.; Xie, Z., Health Risk Assessment Research on Heavy Metals Ingestion Through Groundwater Drinking Pathway for the Residents in Baotou, China. *J. Environ. Health* **2016**, *78*.
30. Xuan, F.; Luo, X.; Hsing, I. M., Conformation-Dependent Exonuclease III Activity Mediated by Metal Ions Reshuffling on Thymine-rich DNA Duplexes for an Ultrasensitive Electrochemical Method for Hg²⁺ Detection. *Anal. Chem.* **2013**, *85*, 4586-4593.
31. Jena, B. K.; Raj, C. R., Gold Nanoelectrode Ensembles for the Simultaneous Electrochemical Detection of Ultratrace Arsenic, Mercury and Copper. *Anal. Chem.* **2008**, *80*, 4836-4844.

32. Xiao, Y.; Rowe, A. A.; Plaxco, K. W., Electrochemical Detection of Parts-Per-Billion Lead via an Electrode-Bound DNAzyme Assembly. *J. Am. Chem. Soc.* **2007**, *129*, 262-264.
33. Zhang, Y.; Zeng, G. M.; Tang, L.; Chen, J.; Zhu, Y.; He, X. X.; He, Y., Electrochemical Sensor based on Electrodeposited Graphene-Au Modified Electrode and NanoAu Carrier Amplified Signal Strategy for Attomolar Mercury Detection. *Anal. Chem.* **2015**, *87*, 989-996.
34. Zhou, Y.; Dong, H.; Liu, L.; Li, M.; Xiao, K.; Xu, M., Selective and Sensitive Colorimetric Sensor of Mercury(II) based on Gold Nanoparticles and 4-Mercaptophenylboronic acid. *Sensors and Actuators B* **2014**, *196*, 106-111.
35. Thomas, K. G.; Thomas, K. J.; Das, S.; George, M. V., A Squaraine-Based Near-IR Absorbing Sensor for the Selective Detection of Transition and Other Metal Ions. *Chem. Commun.* **1997**, 597-599.
36. Maghasi, A. T.; Conklin, S. D.; Shtoyko, T.; Piruska, A.; Richardson, J. N.; Seliskar, C. J.; Heineman, W. R., Spectroelectrochemical Sensing Based on Attenuated Total Internal Reflectance Stripping Voltammetry: Determination of Mercury and Lead. *Anal. Chem.* **2004**, *76*, 1458-1465.
37. Aragay, G.; Pons, J.; Merkoci, A., Recent Trends in Macro-, Micro-, and Nanomaterial-based Tools and Strategies for Heavy-Metal Detection. *Chem. Rev.* **2011**, *111*, 3433-3458.
38. Nolan, E. M.; Lippard, S. J., Tools and Tactics for the Optical Detection of Mercuric Ion. *Chem. Rev.* **2008**, *108*, 3443-3480.
39. Xie, J.; Zheng, Y.; Ying, J. Y., Highly Selective and Ultrasensitive Detection of Hg(2+) based on Fluorescence Quenching of Au Nanoclusters by Hg(2+)-Au(+) Interactions. *Chem. Commun.* **2010**, *46*, 961-963.
40. Cai, S.; Lao, K.; Lau, C.; Lu, J., "Turn-on" Chemiluminescence Sensor for the Highly Selective and Ultrasensitive Detection of Hg²⁺ Ions based on Interstrand Cooperative Coordination and Catalytic Formation of Gold Nanoparticles. *Anal. Chem.* **2011**, *83*, 9702-9708.
41. Chen, B.; Wang, L.; Xiao, Y.; Fronczek, F. R.; Xue, M.; Cui, Y.; Qian, G., A Luminescent Metal-Organic Framework with Lewis Basic Pyridyl Sites for the Sensing of Metal Ions. *Angew. Chem. Int. Ed.* **2009**, *48*, 500-503.
42. Cui, Y.; Song, R.; Yu, J.; Liu, M.; Wang, Z.; Wu, C.; Yang, Y.; Wang, Z.; Chen, B.; Qian, G., Dual-Emitting MOF Supersetdye Composite for Ratiometric Temperature Sensing. *Adv. Mater.* **2015**, *27*, 1420-1425.
43. Cui, Y.; Xu, H.; Yue, Y.; Guo, Z.; Yu, J.; Chen, Z.; Gao, J.; Yang, Y.; Qian, G.; Chen, B., A Luminescent Mixed-Lanthanide Metal-Organic Framework Thermometer. *J. Am. Chem. Soc.* **2012**, *134*, 3979-3982.
44. Cui, Y.; Yue, Y.; Qian, G.; Chen, B., Luminescent Functional Metal-Organic Frameworks. *Chemical reviews* **2012**, *112*, 1126-1162.
45. Allendorf, M. D.; Bauer, C. A.; Bhakta, R. K.; Houk, R. J., Luminescent Metal-Organic Frameworks. *Chem. Soc. Rev.* **2009**, *38*, 1330-1352.
46. Perry Iv, J. J.; Feng, P. L.; Meek, S. T.; Leong, K.; Doty, F. P.; Allendorf, M. D., Connecting Structure with Function in Metal-Organic Frameworks to Design Novel Photo- and Radioluminescent Materials. *J. Mater. Chem.* **2012**, *22*, 10235-10248.
47. Bhunia, A.; Esquivel, D.; Dey, S.; Fernández-Terán, R.; Goto, Y.; Inagaki, S.; Van Der Voort, P.; Janiak, C., A Photoluminescent Covalent Triazine Framework: CO₂ Adsorption, Light-Driven Hydrogen Evolution and Sensing of Nitroaromatics. *J. Mater. Chem. A* **2016**, *4*, 13450-13457.
48. Shahat, A.; Hassan, H. M.; Azzazy, H. M., Optical Metal-Organic Framework Sensor for Selective Discrimination of Some Toxic Metal Ions in Water. *Anal. Chim. Acta* **2013**, *793*, 90-98.

49. Wu, L. L.; Wang, Z.; Zhao, S. N.; Meng, X.; Song, X. Z.; Feng, J.; Song, S. Y.; Zhang, H. J., A Metal-Organic Framework/DNA Hybrid System as a Novel Fluorescent Biosensor for Mercury(II) Ion Detection. *Chem. Eur. J.* **2016**, *22*, 477-480.
50. Liu, B.; Huang, Y.; Zhu, X.; Hao, Y.; Ding, Y.; Wei, W.; Wang, Q.; Qu, P.; Xu, M., Smart Lanthanide Coordination Polymer Fluorescence Probe for Mercury(II) Determination. *Anal. Chim. Acta* **2016**, *912*, 139-45.
51. Li, L.; Chen, Q.; Niu, Z.; Zhou, X.; Yang, T.; Huang, W., Lanthanide MOFs Assembled from Fluorene-based Ligand: Selective Sensing of Pb²⁺ and Fe³⁺ Ions. *J. Mater. Chem. A* **2016**, *4*, 1900-1905.
52. Lu, W.; Qin, X.; Liu, S.; Chang, G.; Zhang, Y.; Luo, Y.; Asiri, A. M.; Al-Youbi, A. O.; Sun, X., Economical, Green Synthesis of Fluorescent Carbon Nanoparticles and their Use as Probes for Sensitive and Selective Detection of Mercury(II) Ions. *Anal. Chem.* **2012**, *84*, 5351-5357.
53. Wang, H. M.; Yang, Y. Y.; Zeng, C. H.; Chu, T. S.; Zhu, Y. M.; Ng, S. W., A Highly Luminescent Terbium-Organic Framework for Reversible Detection of Mercury Ions in Aqueous Solution. *Photochem. Photobiol. Sci.* **2013**, *12*, 1700-1706.
54. Zhu, Y.-M.; Zeng, C.-H.; Chu, T.-S.; Wang, H.-M.; Yang, Y.-Y.; Tong, Y.-X.; Su, C.-Y.; Wong, W.-T., A Novel Highly Luminescent LnMOF film: A Convenient Sensor for Hg²⁺ Detecting *J. Mater. Chem. A* **2013**, *1*, 11312-11319.
55. Ke, F.; Qiu, L. G.; Yuan, Y. P.; Peng, F. M.; Jiang, X.; Xie, A. J.; Shen, Y. H.; Zhu, J. F., Thiol-Functionalization of Metal-Organic Framework by a Facile Coordination-based Postsynthetic Strategy and Enhanced Removal of Hg²⁺ from Water. *J. Haz. Mater.* **2011**, *196*, 36-43.
56. Saleem, H.; Rafique, U.; Davies, R. P., Investigations on Post-Synthetically Modified UiO-66-NH₂ for the Adsorptive Removal of Heavy Metal Ions from Aqueous Solution. *Micro. and Meso. Mater.* **2016**, *221*, 238-244.
57. Yee, K. K.; Reimer, N.; Liu, J.; Cheng, S. Y.; Yiu, S. M.; Weber, J.; Stock, N.; Xu, Z., Effective Mercury Sorption by Thiol-Laced Metal-Organic Frameworks: in Strong Acid and the Vapor Phase. *J. Am. Chem. Soc.* **2013**, *135*, 7795-7798.
58. Xu, X.-Y.; Yan, B., Fabrication and Application of a Ratiometric and Colorimetric Fluorescent Probe for Hg²⁺ based on Dual-Emissive Metal-Organic Framework Hybrids with Carbon Dots and Eu³⁺. *J. Mater. Chem. C* **2016**, *4*, 1543-1547.
59. Li, B.; Zhang, Y.; Ma, D.; Shi, Z.; Ma, S., Mercury Nano-Trap for Effective and Efficient Removal of Mercury(II) from Aqueous Solution. *Nat. Commun.* **2014**, *5*, 5537-5543.
60. Nagarkar, S. S.; Joarder, B.; Chaudhari, A. K.; Mukherjee, S.; Ghosh, S. K., Highly Selective Detection of Nitro Explosives by a Luminescent Metal-Organic Framework. *Angew. Chem. Int. Ed.* **2013**, *52*, 2881-2885.
61. Hu, Z.; Tan, K.; Lustig, W. P.; Wang, H.; Zhao, Y.; Zheng, C.; Banerjee, D.; Emge, T. J.; Chabal, Y. J.; Li, J., Effective Sensing of RDX via Instant and Selective Detection of Ketone Vapors. *Chem. Sci.* **2014**, *5*, 4873-4877.
62. Sanda, S.; Parshamoni, S.; Biswas, S.; Konar, S., Highly Selective Detection of Palladium and Picric Acid by a Luminescent MOF: a Dual Functional Fluorescent Sensor. *Chem. Commun.* **2015**, *51*, 6576-6579.
63. Hu, Z.; Lustig, W. P.; Zhang, J.; Zheng, C.; Wang, H.; Teat, S. J.; Gong, Q.; Rudd, N. D.; Li, J., Effective Detection of Mycotoxins by a Highly Luminescent Metal-Organic Framework. *J. Am. Chem. Soc.* **2015**, *137*, 16209-16215.

64. Hu, Z.; Huang, G.; Lustig, W. P.; Wang, F.; Wang, H.; Teat, S. J.; Banerjee, D.; Zhang, D.; Li, J., Achieving Exceptionally High Luminescence Quantum Efficiency by Immobilizing an AIE Molecular Chromophore into a Metal-Organic Framework. *Chem. Commun.* **2015**, *51*, 3045-3048.
65. Li, B.; Chrzanowski, M.; Zhang, Y.; Ma, S., Applications of Metal-Organic Frameworks Featuring Multi-Functional Sites. *Coordin. Chem. Rev.* **2016**, *307*, 106-129.
66. Eddaoudi, M.; Kim, J.; Rosi, N.; Vodak, D.; Wachter, J.; O'Keeffe, M.; Yaghi, O. M., Systematic Design of Pore Size and Functionality in Isorecticular MOFs and Their Application in Methane Storage. *Science* **2002**, *295*, 469-472.
67. Olkovich, V.; Vasilevskii, D.; Pap, A.; Kalechys, G.; Matveienko, Y.; Baran, A.; Halinouski, N.; Petushok, V., Synthesis of New Polyconjugated Molecules with Biphenyl, Dibenzothiophene, Carbazole and Phenanthrene Units. *Arkivoc* **2008**, *9*, 69-93.
68. Takashima, I.; Kinoshita, M.; Kawagoe, R.; Nakagawa, S.; Sugimoto, M.; Hamachi, I.; Ojida, A., Design of Ratiometric Fluorescent Probes based on Arene-Metal-Ion Interactions and their Application to Cd(II) and Hydrogen Sulfide Imaging in Living Cells. *Chem. Eur. J.* **2014**, *20*, 2184-2192.
69. Wang, J.; Roman-Perez, G.; Soler, J. M.; Artacho, E.; Fernandez-Serra, M. V., Density, Structure and Dynamics of Water: the Effect of van der Waals Interactions. *J. Chem. Phys.* **2011**, *134*.
70. Ding, S. Y.; Dong, M.; Wang, Y. W.; Chen, Y. T.; Wang, H. Z.; Su, C. Y.; Wang, W., Thioether-Based Fluorescent Covalent Organic Framework for Selective Detection and Facile Removal of Mercury(II). *J. Am. Chem. Soc.* **2016**, *138*, 3031-3037.
71. Wen, L.; Zheng, X.; Lv, K.; Wang, C.; Xu, X., Two Amino-Decorated Metal-Organic Frameworks for Highly Selective and Quantitatively Sensing of Hg(II) and Cr(VI) in Aqueous Solution. *Inorg. Chem.* **2015**, *54*, 7133-7135.
72. Shan, F.-S.; Lai, J.-P.; Sun, H.; Zhang, P.; Luo, C.; He, Y.-H.; Feng, H.-R., A Facile, Fast Responsive and Highly Selective Mercury(II) Probe: Characterized by the Fluorescence Quenching of 2,9-dimethyl-1,10-phenanthroline and Two New Metal-Organic Frameworks. *RSC Adv.* **2016**, 66215-66223.
73. Xu, F.; Kou, L.; Jia, J.; Hou, X.; Long, Z.; Wang, S., Metal-Organic Frameworks of Zeolitic Imidazolate Framework-7 and Zeolitic Imidazolate Framework-60 for Fast Mercury and Methylmercury Speciation Analysis. *Anal. Chim. Acta* **2013**, *804*, 240-245.
74. Liu, M.; Li, G.; Cheng, Z., A Novel Dual-Functional Fluorescent Chemosensor for the Selective Detection of 2,4,6-Trinitrotoluene and Hg²⁺. *New J. Chem.* **2015**, *39*, 8484-8491.
75. Yang, J.; Wang, Z.; Li, Y.; Zhuang, Q.; Zhao, W.; Gu, J., Porphyrinic MOFs for Reversible Fluorescent and Colorimetric Sensing of Mercury(II) Ions in Aqueous-Phase. *RSC Adv.* **2016**, *6*, 69807-69814.
76. Li, T.; Zhou, Y.; Sun, J.; Tang, D.; Guo, S.; Ding, X., Ultrasensitive Detection of Mercury(II) Ion Using CdTe Quantum Dots in Sol-Gel-Derived Silica Spheres Coated with Calix[6]arene as Fluorescent Probes. *Microchim. Acta* **2011**, *175*, 113-119.
77. Jurado-Sánchez, B.; Escarpa, A.; Wang, J., Lighting Up Micromotors with Quantum Dots for Smart Chemical Sensing. *Chem. Commun.* **2015**, *51*, 14088-14091.
78. Zhou, Y.; Chen, H.-H.; Yan, B., An Eu³⁺-Post-Functionalized Nanosized Metal-Organic Framework for Cation Exchange-based Fe³⁺-Sensing in an Aqueous Environment. *J. Mater. Chem. A* **2014**, *2*, 13691-13697.

79. Yang, C. X.; Ren, H. B.; Yan, X. P., Fluorescent Metal-Organic Framework MIL-53(Al) for Highly Selective and Sensitive Detection of Fe³⁺ in Aqueous Solution. *Anal. Chem.* **2013**, 85, 7441-7446.
80. Ho, Y. S., Review of Second-Order Models for Adsorption Systems. *J. Haz. Mater.* **2006**, 136, 681-689.
81. Yantasee, W.; Rutledge, R. D.; Chouyyok, W.; Sukwarotwat, V.; Orr, G.; Warner, C. L.; Warner, M. G.; Fryxell, G. E.; Wiacek, R. J.; Timchalk, C.; Addleman, R. S., Functionalized Nanoporous Silica for the Removal of Heavy Metals from Biological Systems: Adsorption and Application. *ACS Appl. Mater. Inter.* **2010**, 2, 2749-58.
82. Shin, Y.; Fryxell, G. E.; Um, W.; Parker, K.; Mattigod, S. V.; Skaggs, R., Sulfur-Functionalized Mesoporous Carbon. *Adv. Func. Mater.* **2007**, 17, 2897-2901.
83. Manos, M. J.; Petkov, V. G.; Kanatzidis, M. G., H₂xMnxSn₃-xS₆(x = 0.11-0.25): A Novel Reusable Sorbent for Highly Specific Mercury Capture Under Extreme pH Conditions. *Adv. Func. Mater.* **2009**, 19, 1087-1092.
84. Hafizovic, J.; Bjorgen, M.; Olsbye, U.; Dietzel, P. D. C.; Bordiga, S.; Prestipino, C.; Lamberti, C.; Lillerud, K. P., The Inconsistency in Adsorption Properties and PXRD Data of MOF-5 is Rationalized by Framework Interpenetration and the Presence of Organic and Inorganic Species in the Nanocavities. *J. Am. Chem. Soc.* **2007**, 129, 3612-3620.
85. Mon, M.; Ferrando-Soria, J.; Grancha, T.; Fortea-Perez, F. R.; Gascon, J.; Leyva-Perez, A.; Armentano, D.; Pardo, E., Selective Gold Recovery and Catalysis in a Highly Flexible Methionine-Decorated Metal-Organic Framework. *J. Am. Chem. Soc.* **2016**, 138, 7864-7867.
86. Luo, F.; Chen, J. L.; Dang, L. L.; Zhou, W. N.; Lin, H. L.; Li, J. Q.; Liu, S. J.; Luo, M. B.; Luo, M. B., High Performance Hg^{II} Removal from Low Concentration Aqueous Solutions Using Acylamide and Hydroxyl MOFs. *J. Mater Chem. A* **2015**, 3, 9616-9620.
87. He, J.; Yee, K.-K.; Xu, Z.; Zeller, M.; Hunter, A. D.; Chui, S. S.-Y.; Che, C.-M., Thioether Side Chains Improve the Stability, Fluorescence, and Metal Uptake of a Metal-Organic Framework. *Chem. Mater.* **2011**, 23, 2940-2947.
88. Huang, L.; He, M.; Chen, B.; Hu, B., A Mercapto- Functionalized Magnetic Zr-MOF by Solvent-Assisted Ligand Exchange for Hg²⁺-Removal from Water. *J. Mater. Chem. A* **2016**, 4, 5159-5166.
89. Luo, X.; Shen, T.; Ding, L.; Zhong, W.; Luo, J.; Luo, S., Novel Thymine-Functionalized MIL-101 Prepared by Post-Synthesis and Enhanced Removal of Hg(2+) from Water. *J. Haz. Mater.* **2016**, 306, 313-322.
90. Wu, Y.; Xu, G.; Liu, W.; Yang, J.; Wei, F.; Li, L.; Zhang, W.; Hu, Q., Postsynthetic Modification of Copper Terephthalate Metal-Organic Frameworks and their New Application in Preparation of Samples Containing Heavy Metal Ions. *Micro. and Meso. Mater.* **2015**, 210, 110-115.
91. Wang, K.; Huang, H.; Xue, W.; Liu, D.; Zhao, X.; Xiao, Y.; Li, Z.; Yang, Q.; Wang, L.; Zhong, C., An Ultrastable Zr Metal-Organic Framework with a Thiophene-type Ligand Containing Methyl Groups. *CrystEngComm* **2015**, 17, 3586-3590.
92. Chakraborty, A.; Bhattacharyya, S.; Hazra, A.; Ghosh, A. C.; Maji, T. K., Post-Synthetic Metalation in an Anionic MOF for Efficient Catalytic Activity and Removal of Heavy Metal Ions from Aqueous Solution. *Chem. Commun.* **2016**, 52, 2831-2834.
93. Huang, L.; He, M.; Chen, B.; Hu, B., A Designable Magnetic MOF Composite and Facile Coordination-based Post-Synthetic Strategy for the Enhanced Removal of Hg²⁺ from Water. *J. Mater. Chem. A* **2015**, 3, 11587-11595.

94. Fang, Q. R.; Yuan, D. Q.; Sculley, J.; Li, J. R.; Han, Z. B.; Zhou, H. C., Functional Mesoporous Metal-Organic Frameworks for the Capture of Heavy Metal Ions and Size-Selective Catalysis. *Inorg. Chem.* **2010**, *49*, 11637-11642.
95. Bellú, S.; Hure, E.; Trapé, M.; Rizzotto, M.; Sutich, E.; Sigrist, M.; Moreno, V., The Interaction Between Mercury(II) and Sulfathiazole. *Química Nova* **2003**, *26*, 188-192.
96. Obasi, L.; Ukoha, P.; Chah, K.; Anaga, A., Synthesis, Spectroscopic Characterization and Antibacterial Screening of Novel n-(benzothiazol-2-yl)ethanamides. *Eclética Quím.* **2011**, *36*, 7-17.
97. Lu, Y.-C.; Chen, J.; Wang, A.-J.; Bao, N.; Feng, J.-J.; Wang, W.; Shao, L., Facile Synthesis of Oxygen and Sulfur Co-Doped Graphitic Carbon Nitride Fluorescent Quantum Dots and their Application for Mercury(ii) Detection and Bioimaging. *J. Mater. Chem. C* **2015**, *3*, 73-78.
98. Wang, Y.-S.; Cheng, C.-C.; Chen, J.-K.; Ko, F.-H.; Chang, F.-C., Bioinspired Supramolecular Fibers for Mercury Ion Adsorption. *J. Mater. Chem. A* **2013**, *1*, 7745-7750.
99. Yang, J.; Hu, Y.; Tan, J.; Jia, L.; Zhu, Y.-H.; Yu, J.-S., Ultra-Bright Near-Infrared-Emitting HgS/ZnS Core/Shell Nanocrystals for in Vitro and in Vivo Imaging. *J. Mater. Chem. B* **2015**, *3*, 6928-6938.
100. Block, E., *Reactions of Organosulfur Compounds: Organic Chemistry: A Series of Monographs*. Academic Press: 2013; Vol. 37.
101. Niu, Y.; Feng, S.; Qu, R.; Ding, Y.; Wang, D.; Wang, Y., Theoretical Study on the Interaction of Sulfur- and Aminopyridine-Containing Chelating Resins with Hg(II) and Pb(II). *Inter. J. Quantum Chem.* **2011**, *111*, 991-1001.
102. Perry, J. J. t.; Perman, J. A.; Zaworotko, M. J., Design and Synthesis of Metal-Organic Frameworks using Metal-Organic Polyhedra as Supermolecular Building Blocks. *Chem. Soc. Rev.* **2009**, *38*, 1400-1417.
103. Li, J. R.; Sculley, J.; Zhou, H. C., Metal-Organic Frameworks for Separations. *Chem. Rev.* **2012**, *112*, 869-932.
104. Yoon, M.; Srirambalaji, R.; Kim, K., Homochiral Metal-Organic Frameworks for Asymmetric Heterogeneous Catalysis. *Chem. Rev.* **2012**, *112*, 1196-1231.
105. Deng, H.; Doonan, C. J.; Furukawa, H.; Ferreira, R. B.; Towne, J.; Knobler, C. B.; Wang, B.; Yaghi, O. M., Multiple Functional Groups of Varying Ratios in Metal-Organic Frameworks. *Science* **2010**, *327*, 846-50.
106. Lan, A.; Li, K.; Wu, H.; Olson, D. H.; Emge, T. J.; Ki, W.; Hong, M.; Li, J., A Luminescent Microporous Metal-Organic Framework for the Fast and Reversible Detection of High Explosives. *Angew. Chem. Int. Ed.* **2009**, *48*, 2334-2338.
107. Pramanik, S.; Hu, Z.; Zhang, X.; Zheng, C.; Kelly, S.; Li, J., A Systematic Study of Fluorescence-based Detection of Nitroexplosives and other Aromatics in the Vapor Phase by Microporous Metal-Organic Frameworks. *Chem. Eur. J.* **2013**, *19*, 15964-15971.
108. Hu, Z.; Pramanik, S.; Tan, K.; Zheng, C.; Liu, W.; Zhang, X.; Chabal, Y. J.; Li, J., Selective, Sensitive, and Reversible Detection of Vapor-Phase High Explosives via Two-Dimensional Mapping: A New Strategy for MOF-Based Sensors. *Cryst. Growth Des.* **2013**, *13*, 4204-4207.
109. Banerjee, D.; Hu, Z.; Pramanik, S.; Zhang, X.; Wang, H.; Li, J., Vapor Phase Detection of Nitroaromatic and Nitroaliphatic Explosives by Fluorescence Active Metal-Organic Frameworks. *CrystEngComm* **2013**, *15*, 9745.

110. Pramanik, S.; Zheng, C.; Zhang, X.; Emge, T. J.; Li, J., New Microporous Metal-Organic Framework Demonstrating Unique Selectivity for Detection of High Explosives and Aromatic Compounds. *J. Am. Chem. Soc.* **2011**, *133*, 4153-4155.
111. Guo, H.-D.; Guo, X.-M.; Batten, S. R.; Song, J.-F.; Song, S.-Y.; Dang, S.; Zheng, G.-L.; Tang, J.-K.; Zhang, H.-J., Hydrothermal Synthesis, Structures and Luminescent Properties of Seven d¹⁰ Metal-Organic Frameworks Based on 9,9-Dipropylfluorene-2,7-Dicarboxylic acid (H₂DFDA). *Cryst. Growth Des.* **2008**, *9*, 1394-1401.
112. Hong, C. S.; Lim, K. S.; Jeong, S. Y.; Kang, D. W.; Song, J. H.; Jo, H.; Lee, W. R.; Phang, W. J.; Moon, D., Luminescent Metal-Organic Framework Sensor: Exceptional Cd²⁺ Turn-on Detection and First In Situ Visualization of Cd²⁺ Ion Diffusion to a Crystal. *Chem. Eur. J.* **2017**, *23*, 4803-4809.
113. Health, D. o. P., Toxicological Profile for Carbon Tetrachloride. **2014**.
114. Santharam, S.; Davis, L. C.; Erickson, L. E., Biodegradation of Carbon Tetrachloride in Simulated Groundwater Flow Channels. *Environ. Prog. Sus. Energy* **2014**, *33*, 444-453.
115. Organization, W. H., Carbon Tetrachloride in Drinking Water. **2004**.
116. Ruch, R. J.; Klaunig, J. E.; Schultz, N. E.; Askari, A. B.; Lacher, D. A.; Pereira, M. A.; Goldblatt, P. J., Mechanisms of Chloroform and Carbon Tetrachloride Toxicity in Primary Cultured Mouse Hepatocytes. *Environ. Health Perspectives* **1986**, *69*, 301-305.
117. Luo, L.; Chen, H.; Zhang, L.; Xu, K.; Lv, Y., A Cataluminescence Gas Sensor for Carbon Tetrachloride based on Nanosized ZnS. *Anal. Chim. Acta* **2009**, *635*, 183-187.
118. Xu, S.; Zhang, L.; Zhang, X.; He, C.; Lv, Y., Synthesis of Ag₂Se Nanomaterial by Electrodeposition and its Application as Cataluminescence Gas Sensor Material for Carbon Tetrachloride. *Sensors and Actuators B* **2011**, *155*, 311-316.
119. Regmi, B. P.; Monk, J.; El-Zahab, B.; Das, S.; Hung, F. R.; Hayes, D. J.; Warner, I. M., A Novel Composite Film for Detection and Molecular Weight Determination of Organic Vapors. *J. Mater. Chem.* **2012**, *22*, 13732-13741.
120. Ferguson, A.; Liu, L.; Tapperwijn, S. J.; Perl, D.; Coudert, F. X.; Van Cleuvenbergen, S.; Verbiest, T.; van der Veen, M. A.; Telfer, S. G., Controlled Partial Interpenetration in Metal-Organic Frameworks. *Nat. Chem.* **2016**, *8*, 250-257.
121. Honma, T.; Suda, M., Changes in Plasma Lipoproteins as Toxicity Markers for Carbon Tetrachloride, Chloroform and Dichloromethane. *Indus. Health* **1997**, *35*, 519-531.
122. Patil, N. R.; Melavanki, R. M.; Kapatkar, S. B.; Chandrasekhar, K.; Ayachit, N. H.; Umapathy, S., Solvent Effect on the Fluorescence Quenching of Biologically Active Carboxamide by Aniline and Carbon Tetrachloride in Different Solvents Using S–V Plots. *J. Lumin.* **2012**, *132*, 558-565.
123. Kadadevarmath, J. S.; Malimath, G. H.; Melavanki, R. M.; Patil, N. R., Static and Dynamic Model Fluorescence Quenching of Laser Dye by Carbon Tetrachloride in Binary Mixtures. *Spectrochim. Acta A Mol Biomol. Spectrosc.* **2014**, *117*, 630-634.
124. He, C.-T.; Tian, J.-Y.; Liu, S.-Y.; Ouyang, G.; Zhang, J.-P.; Chen, X.-M., A Porous Coordination Framework for Highly Sensitive and Selective Solid-Phase Microextraction of Non-Polar Volatile Organic Compounds. *Chem. Sci.* **2013**, *4*, 351-356.
125. Karmakar, A.; Desai, A. V.; Manna, B.; Joarder, B.; Ghosh, S. K., An Amide-Functionalized Dynamic Metal-Organic Framework Exhibiting Visual Colorimetric Anion Exchange and Selective Uptake of Benzene over Cyclohexane. *Chem. Eur. J.* **2015**, *21*, 7071-7076.

126. Pentyala, V.; Davydovskaya, P.; Ade, M.; Pohle, R.; Urban, G., Metal–Organic Frameworks for Alcohol Gas Sensor. *Sensors and Actuators B* **2016**, *222*, 904-909.
127. Stylianou, K. C.; Heck, R.; Chong, S. Y.; Bacsa, J.; Jones, J. T. A.; Khimyak, Y. Z.; Bradshaw, D.; Rosseinsky, M. J., A Guest-Responsive Fluorescent 3D Microporous Metal-Organic Framework Derived from a Long-Lifetime Pyrene Core. *J. Am. Chem. Soc.* **2010**, *132*, 4119-4130.
128. Wang, Y.; Yuan, B.; Xu, Y. Y.; Wang, X. G.; Ding, B.; Zhao, X. J., Turn-On Fluorescence and Unprecedented Encapsulation of Large Aromatic Molecules within a Manganese(II)-Triazole Metal-Organic Confined Space. *Chem. Eur. J.* **2015**, *21*, 2107-2116.
129. Jones, R. N., The Ultraviolet Absorption Spectra of Anthracene Derivatives. *Chemical reviews* **1947**, *41*, 353-371.
130. Lewis, C.; Ware, W. R., Wavelength Effects in Fluorescence Quenching: The Anthracene-Carbon Tetrachloride System. *Chem. Phys. Lett.* **1971**, *15*, 290-292.
131. Carroll, F. A.; Whitten, D. G., Multiplicity of the Reacting State in the Photoaddition of Carbon Tetrachloride to Anthracene. *J. Phys. Chem.* **1976**, *80*, 2046-2047.
132. Chen, X.; Huang, Z.; Chen, S.-Y.; Li, K.; Yu, X.-Q.; Pu, L., Enantioselective Gel Collapsing: A New Means of Visual Chiral Sensing. *J. Am. Chem. Soc.* **2010**, *132*, 7297-7299.
133. Shustova, N. B.; McCarthy, B. D.; Dinca, M., Turn-On Fluorescence in Tetraphenylethylene-based Metal-Organic Frameworks: An Alternative to Aggregation-Induced Emission. *J. Am. Chem. Soc.* **2011**, *133*, 20126-20129.
134. Grosjean, C.; Miranda, P. H.; Perrin, M.; Poggi, P., Assessment of World Lithium Resources and Consequences of their Geographic Distribution on the Expected Development of the Electric Vehicle Industry. *Renew. Sus. Energy Rev.* **2012**, *16*, 1735-1744.
135. Gruber, P. W.; Medina, P. A.; Keoleian, G. A.; Kesler, S. E.; Everson, M. P.; Wallington, T. J., Global Lithium Availability. *J. Indus. Eco.* **2011**, *15*, 760-775.
136. Hamzaoui, A. H.; Jamoussi, B.; M'Nif, A., Lithium Recovery from Highly Concentrated Solutions: Response Surface Methodology (RSM) Process Parameters Optimization. *Hydrometallurgy* **2008**, *90*, 1-7.
137. Kesler, S. E.; Gruber, P. W.; Medina, P. A.; Keoleian, G. A.; Everson, M. P.; Wallington, T. J., Global Lithium Resources: Relative Importance of Pegmatite, Brine and other Deposits. *Ore Geol. Rev.* **2012**, *48*, 55-69.
138. Li, X.; Zhang, C.; Zhang, S.; Li, J.; He, B.; Cui, Z., Preparation and Characterization of Positively Charged Polyamide Composite Nanofiltration Hollow Fiber Membrane for Lithium and Magnesium Separation. *Desalination* **2015**, *369*, 26-36.
139. Nie, X.-Y.; Sun, S.-Y.; Sun, Z.; Song, X.; Yu, J.-G., Ion-Fractionation of Lithium Ions from Magnesium Ions by Electrodialysis Using Monovalent Selective Ion-Exchange Membranes. *Desalination* **2017**, *403*, 128-135.
140. Shi, C.; Jing, Y.; Jia, Y., Solvent Extraction of Lithium Ions by Tri-n-butyl Phosphate Using a Room Temperature Ionic Liquid. *J. of Mol. Liq.* **2016**, *215*, 640-646.
141. Zhao, Y.; Shi, W.; Van der Bruggen, B.; Gao, C.; Shen, J., Tunable Nanoscale Interlayer of Graphene with Symmetrical Polyelectrolyte Multilayer Architecture for Lithium Extraction. *Adv. Mater. Inter.* **2018**, *5*, 1701449-1701454.
142. Diallo, M. S.; Kotte, M. R.; Cho, M., Mining Critical Metals and Elements from Seawater: Opportunities and Challenges. *Environ. Sci. Technol.* **2015**, *49*, 9390-9399.

143. Song, J. F.; Nghiem, L. D.; Li, X.-M.; He, T., Lithium Extraction from Chinese Salt-Lake Brines: Opportunities, Challenges, and Future Outlook. *Environ. Sci. Water Res. Tech.* **2017**, *3*, 593-597.
144. Risacher, F.; Fritz, B., Quarternary Geochemical Evolution of the Salars of Uyuni and Coipasa, Central Altiplano, Bolivia. *Chem. Geo.* **1990**, *90*, 211-231.
145. Furukawa, H.; Ko, N.; Go, Y. B.; Aratani, N.; Choi, S. B.; Choi, E.; Yazaydin, A. O.; Snurr, R. Q.; O'Keeffe, M.; Kim, J.; Yaghi, O. M., Ultrahigh Porosity in Metal-Organic Frameworks. *Science* **2010**, *329*, 424-428.
146. Chen, L.; Ye, J. W.; Wang, H. P.; Pan, M.; Yin, S. Y.; Wei, Z. W.; Zhang, L. Y.; Wu, K.; Fan, Y. N.; Su, C. Y., Ultrafast Water Sensing and Thermal Imaging by a Metal-Organic Framework with Switchable Luminescence. *Nat. Commun.* **2017**, *8*, 15985.
147. You, L.; Zha, D.; Anslyn, E. V., Recent Advances in Supramolecular Analytical Chemistry Using Optical Sensing. *Chem. Rev.* **2015**, *115*, 7840-7892.
148. Obare, S. O.; Hollowell, R. E.; Murphy, C. J., Sensing Strategy for Lithium Ion Based on Gold Nanoparticles. *Langmuir* **2002**, *18*, 10407-10410.
149. He, Q.; Zhang, Z.; Brewster, J. T.; Lynch, V. M.; Kim, S. K.; Sessler, J. L., Hemispherand-Strapped Calix[4]pyrrole: An Ion-pair Receptor for the Recognition and Extraction of Lithium Nitrite. *J. Am. Chem. Soc.* **2016**, *138*, 9779-9782.
150. Kaur, G.; Singh, A.; Venugopalan, P.; Kaur, N.; Singh, N., Selective Recognition of Lithium(I) Ions Using Biginelli-Based Fluorescent Organic Nanoparticles in an Aqueous Medium. *RSC Adv.* **2016**, *6*, 1792-1799.
151. Gao, J.; Rochat, S.; Qian, X.; Severin, K., A Simple Assay for the Fluorometric Detection of Lithium Ions in Aqueous Solution. *Chem. Eur. J.* **2010**, *16*, 5013-7.
152. Rochat, S.; Grote, Z.; Severin, K., Ruthenium-Based Metallacrown Complexes for the Selective Detection of Lithium Ions in Water and in Serum by Fluorescence Spectroscopy. *Org. Biomol. Chem.* **2009**, *7*, 1147-1153.
153. Citterio, D.; Takeda, J.; Kosugi, M.; Hisamoto, H.; Sasaki, S.; Komatsu, H.; Suzuki, K., pH-Independent Fluorescent Chemosensor for Highly Selective Lithium Ion Sensing. *Anal. Chem.* **2007**, *79*, 1237-1242.
154. Deria, P.; Gomez-Gualdron, D. A.; Bury, W.; Schaefer, H. T.; Wang, T. C.; Thallapally, P. K.; Sarjeant, A. A.; Snurr, R. Q.; Hupp, J. T.; Farha, O. K., Ultraporos, Water Stable, and Breathing Zirconium-Based Metal-Organic Frameworks with ftw Topology. *J. Am. Chem. Soc.* **2015**, *137*, 13183-13190.
155. Liu, T. F.; Feng, D.; Chen, Y. P.; Zou, L.; Bosch, M.; Yuan, S.; Wei, Z.; Fordham, S.; Wang, K.; Zhou, H. C., Topology-Guided Design and Syntheses of Highly Stable Mesoporous Porphyrinic Zirconium Metal-Organic Frameworks with High Surface Area. *J. Am. Chem. Soc.* **2015**, *137*, 413-419.
156. Burrows, A. D., Mixed-Component Metal-Organic Frameworks (MC-MOFs): Enhancing Functionality Through Solid Solution Formation and Surface Modifications. *CrystEngComm* **2011**, *13*, 3623-3642.
157. Liu, C.; Luo, T. Y.; Feura, E. S.; Zhang, C.; Rosi, N. L., Orthogonal Ternary Functionalization of a Mesoporous Metal-Organic Framework via Sequential Postsynthetic Ligand Exchange. *J. Am. Chem. Soc.* **2015**, *137*, 10508-10511.
158. Zhang, X.; Frey, B. L.; Chen, Y. S.; Zhang, J., Topology-Guided Stepwise Insertion of Three Secondary Linkers in Zirconium Metal-Organic Frameworks. *J. Am. Chem. Soc.* **2018**, *140*, 7710-7715.

159. Li, J.; Cai, W.; Zhang, Y.; Chen, Z.; Xu, G.; Cheng, H., Novel Polyamide Proton Exchange Membranes with Bi-Functional Sulfonimide Bridges for Fuel Cell Applications. *Electrochim. Acta* **2015**, *151*, 168-176.
160. Bednaříková, T.; Tošner, Z.; Horský, J.; Jindřich, J., Synthesis of C₃-Symmetric Tri(alkylamino) Guests and their Interaction with Cyclodextrins. *J. Incl. Phenom. Macro.* **2015**, *81*, 141-152.
161. Mahler, J.; Persson, I., A Study of the Hydration of the Alkali Metal Ions in Aqueous Solution. *Inorg. Chem.* **2012**, *51*, 425-438.
162. Bunck, D. N.; Dichtel, W. R., Mixed Linker Strategies for Organic Framework Functionalization. *Chem. Eur. J.* **2013**, *19*, 818-827.
163. Morizur, V.; Olivero, S.; Desmurs, J. R.; Knauth, P.; Duñach, E., Novel Lithium and Sodium Salts of Sulfonamides and Bis(sulfonyl)imides: Synthesis and Electrical Conductivity. *New J. Chem.* **2014**, *38*, 6193-6197.
164. Yoshizawa, M.; Xu, W.; Angell, C. A., Ionic Liquids by Proton Transfer: Vapor Pressure, Conductivity, and the Relevance of pK_a from Aqueous Solutions. *J. Am. Chem. Soc.* **2003**, *125*, 15411-15219.
165. Gunnlaugsson, T.; Bichell, B.; Nelson, C., A Novel Fluorescent Photoinduced Electron Transfer (PET) Sensor for Lithium. *Tet. Lett.* **2002**, *43*, 4989-4992.
166. Sanniccolo, F.; Brenna, E.; Benincori, T.; Zotti, G.; Zecchin, S.; Schiavon, G.; Pilati, T., Highly Ordered Poly(cyclopentabithiophenes) Functionalized with Crown-Ether Moieties for Lithium- and Sodium-Sensing Electrodes. *Chem. Mater.* **1998**, *10*, 2167-2176.
167. Katsuta, S.; Saito, Y.; Takahashi, S., Application of a Lithium-Ion Selective Metallacrown to Extraction-Spectrophotometric Determination of Lithium in Saline Water. *Anal. Sci.* **2018**, *34*, 189-193.
168. Hirayama, E.; Sugiyama, T.; Hisamoto, H.; Suzuki, K., Visual and Colorimetric Lithium Ion Sensing Based on Digital Color Analysis. *Anal. Chem.* **2000**, *72*, 465-474.
169. Obare, S. O.; Murphy, C. J., A Two-Color Fluorescent Lithium Ion Sensor. *Inorg. Chem.* **2001**, *40*, 6080-6082.
170. Guo, Y.; Ying, Y.; Mao, Y.; Peng, X.; Chen, B., Polystyrene Sulfonate Threaded through a Metal-Organic Framework Membrane for Fast and Selective Lithium-Ion Separation. *Angew. Chem. Int. Ed.* **2016**, *55*, 15120-15124.
171. Lu, J.; Qin, Y.; Zhang, Q.; Wu, Y.; Cui, J.; Li, C.; Wang, L.; Yan, Y., Multilayered Ion-Imprinted Membranes with High Selectivity Towards Li⁺ based on the Synergistic Effect of 12-crown-4 and Polyether sulfone. *Appl. Sur. Sci.* **2018**, *427*, 931-941.
172. Moazeni, M.; Hajipour, H.; Askari, M.; Nusheh, M., Hydrothermal Synthesis and Characterization of Titanium Dioxide Nanotubes as Novel Lithium Adsorbents. *Mater. Res. Bull.* **2015**, *61*, 70-75.
173. Chitrakar, R.; Makita, Y.; Ooi, K.; Sonoda, A., Lithium Recovery from Salt-Lake Brine by H₂TiO₃. *Dalton. Trans.* **2014**, *43*, 8933-8939.
174. Park, H.; Singhal, N.; Jho, E. H., Lithium Sorption Properties of HMnO in Seawater and Wastewater. *Water Res.* **2015**, *87*, 320-327.